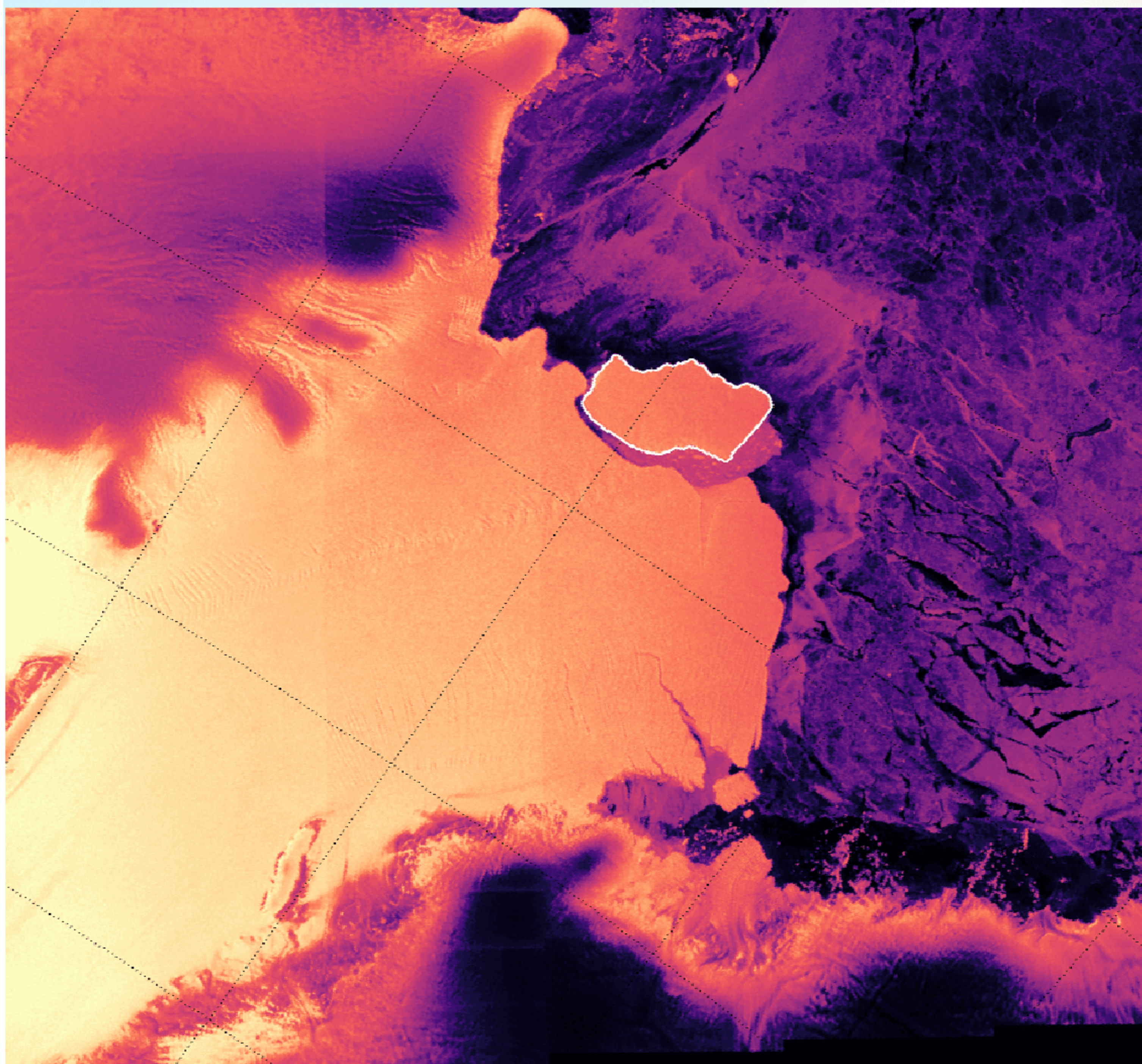




RUSSIAN
JOURNAL *of*
EARTH SCIENCES

Vol. 24
Issue 6



LATE MIDDLE TO LATE ORDOVICIAN PHOSPHATE ACCUMULATION OF THE MOYERO RIVER SECTION (SIBERIA): A RECORD OF UPWELLING AND GLOBAL COOLING

N. Lykov ^{*,1,3} , Yu. Rostovtseva ² , and A. Dronov ¹ 

¹Geological Institute of the Russian Academy of Sciences, Moscow, Russia

²Geophysical Center of the Russian Academy of Sciences, Moscow, Russia

³Gubkin Russian State University of Oil and Gas, Moscow, Russia

* **Correspondence to:** Nikita Lykov, lykownikita@gmail.com

Abstract: The phosphate-bearing rocks (phosphate rocks and phosphorites) were studied over a 45-meter interval of the Moyero river section, covering the upper part of the Darriwilian and the lower part of the Sandbian stages of the Ordovician. These rocks were investigated by field observations and laboratory methods, including optic and scanning electron microscopy, X-ray diffraction analyses. The accumulation of phosphatic matter is manifested in carbonates, sandstones, and aleurolites in the form of grains (ooids and peloids), intraclasts, phosphatic and phosphatized shells. In argillites, it is represented by cryptocrystalline matter. Phosphate matter consists of fluorapatite. The peaks of phosphate accumulation are associated with the formation of layers of physically reworked granular phosphorites (condensation horizons) directly above the depositional sequence boundaries. The formation of the studied phosphate-bearing rocks during the Darriwilian-Sandbian transition was influenced by a combination of global (Great Ordovician Biodiversification Event (GOBE), reduction in sea surface temperature, atmospheric CO₂, high sea level, flooding of craton margins) and regional (equatorial position of Siberia, arid climate, facies) factors. Global conditions led to the enrichment of seawater with phosphorus and the effect of upwelling. Regional conditions determined the characteristics of phosphate formation. Studied phosphate-bearing rocks can be considered as a record of upwelling on the Siberian craton during the Middle-Late Ordovician transition and one of the manifestations of long-term global cooling started early in the Middle Ordovician.

Keywords: Middle Ordovician, Late Ordovician, upwelling, phosphates, Siberian platform, Paleoclimate.

Citation: Lykov, N., Yu. Rostovtseva, and A. Dronov (2024), Late Middle to Late Ordovician Phosphate Accumulation of the Moyero River Section (Siberia): A Record of Upwelling and Global Cooling, *Russian Journal of Earth Sciences*, 24, ES6001, EDN: KFGDNB, <https://doi.org/10.2205/2024es000946>

RESEARCH ARTICLE

Received: 4 September 2024

Accepted: 22 October 2024

Published: 26 December 2024



Copyright: © 2024. The Authors. This article is an open access article distributed under the terms and conditions of the Creative Commons Attribution (CC BY) license (<https://creativecommons.org/licenses/by/4.0/>).

Introduction

Along with carbon, phosphorus is the most important bioelement, without which life on our planet is impossible. Therefore, the biospheric aspect of phosphorus is so important that without it, full-fledged presentation of the geochemistry of this small element is impossible [Yudovich et al., 2020]. Phosphorites are extremely important as an indicator of the biosphere evolution and paleoenvironmental conditions (upwelling, low sedimentation rates, transgression, etc.). Their accumulation also clearly correlates with climate changes the evolution of the biosphere. Their practical significance is also important: they are the source of phosphoric acid and rare earth elements. They are also widely used as natural fertilizers. [Frolov, 1993].

The widespread distribution of the Ordovician phosphate-bearing rocks on the Siberian platform has been known for a long time [Krasilnikova and Smirnov, 1955, 1962; Markov and Zanin, 1979; Zanin and Matukhina, 1983]. Their presence is noted mainly in the

deposits of the late Middle to early Upper Ordovician. They are represented by separate layers of granular phosphorites as well as carbonate and/or terrigenous rocks enriched with a phosphate component, represented by phosphatic ooids and phosphatized litho- and bioclasts. The Gurevsky phosphorite field, confined to the Chertovskian regional stage of the upper Ordovician, is one of the richest and best studied on the Siberian platform. It is located in the valley of the Podkamennaya Tunguska River [Dronov, 2013; Markov and Zanin, 1979]. Phosphorites in the Moyero river section have been noted by previous researches [Krasilnikova and Smirnov, 1962; Markov, 1969; Myagkova et al., 1963, 1977]. Some of them noted only single manifestations of phosphate accumulation in the form of a layer of phosphate conglomerate and enrichment of rocks with phosphate lingulid brachiopods [Myagkova et al., 1977]. At the same time, back in the 1950s, a special prospecting for phosphorus was carried out in the Moyero river valley. The high content of P_2O_5 (from 5 to 50 kg/m²) in the rocks was recorded [Krasilnikova and Smirnov, 1962]. However, details of the phosphorites distribution in the Moyero river section still require clarification.

The purpose of this work is to study and interpret the origin of phosphate accumulation in the Middle to Upper Ordovician interval of the Moyero river section. The authors refer the rocks containing more than 3–5% of phosphate matter to phosphate-bearing rocks. We distinguish phosphate rocks and phosphorites according to J. Trappe' nomenclature system [Trappe, 2001].

Geological Setting

The Siberian paleocontinent in the Ordovician embraced several basins. The largest ones are the Irkutsk Amphitheater (or the Irkutsk basin) and the Tungus Syncline (or the Tungus basin) [Dronov, 2013; Kanygin et al., 2007]. The Moyero river section is located in the northern part of Tungus basin adjacent to the Anabar land (Figure 1A).

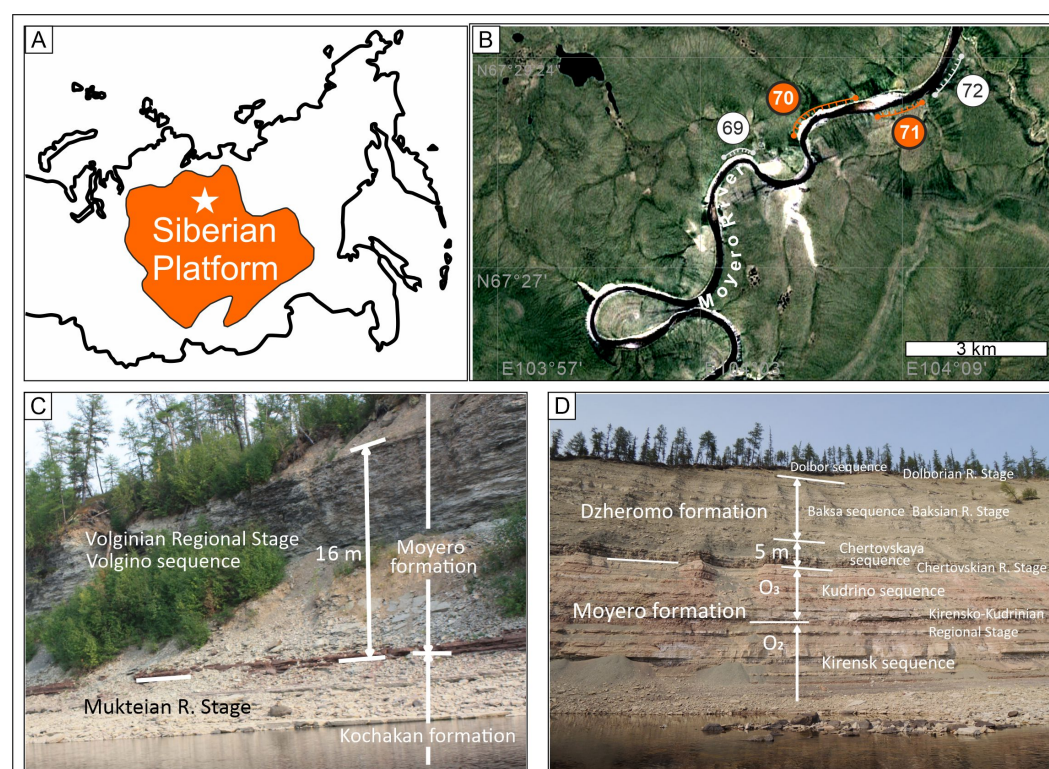


Figure 1. Geographical position and outcrops of the studied deposits. A) Position of the Moyero section on the Siberian platform indicated with a star. B) Satellite map, showing locations of the 69th to 72nd outcrops along the Moyero river. The studied outcrops, marked with orange colour. C) Field photo of 71th outcrop. D) Field photo of 70th outcrop.

In the Ordovician of the Tungus basin two carbonate series of contrast lithology could be distinguished: 1) warm water tropical carbonate series (Tremadocian-Floian) and 2) cool-water carbonate series (Sandbian-Katian) [Dronov, 2009, 2013]. These two series are separated in the Moyero river section by a relatively thick and well-developed transitional interval (Dapingian-Darriwilian) with alteration of cool water and warm water carbonates. The latter becomes less and less abundant upward the section.

The Moyero river reference section is one of the most complete and continuous Ordovician sections on the entire Siberian platform [Myagkova et al., 1963]. However, due to its remoteness, it remains rarely visited by scientists, as a result of which many aspects of sedimentology are insufficiently studied. Outcrops along the Moyero River are traditionally marked with specific numbers such as 69, 70, 71, 72 (Figure 1B) and so on given to them by O. I. Nikiforova in 1951 [Myagkova et al., 1977]. The Ordovician strata are almost horizontal or slightly tilted (2° to 3°) to the south. The Ordovician succession of the Moyero river is subdivided into four formations (from the base upward): Irbukli, Kochakan, Moyero, and Dzheromo formations [Kanygin et al., 2007]. Identified intervals of phosphate accumulation are from the Moyero and Lower part of the Dzheromo formations. Those formations crop out on the left and right banks of the river (outcrops 70 and 71, Figure 1B) about 1.5 km upstream the Bugarikta River mouth. The Moyero formation corresponds to the Volginian and Kirensko-Kudrinian Regional Stages of the upper Darriwilian and lower Sandbian stages [Tolmacheva and Dronov, 2008]. The Dzheromo formation corresponds to the Chertovskian, Baksian and Dolborian regional stages of the Sandbian and Katian Global stages [Kanygin et al., 2016].

Material and Method

Fieldworks for this study was conducted in July 2021, and July 2022. A total of more than a hundred samples were collected by A. Dronov and N. Lykov. These samples were studied by various methods. We used longitudinal and tangential 2.5 × 2.5 cm thin sections for lithological identification. Results of the microscopic study were confirmed by X-ray diffraction analyses. We used X-ray diffractometer Rigaku Miniflex 600 in the Geological department of Moscow State University. For the study, the sample weight (3.0 g) was grind to a fine powder (about 0.01 mm). The resulting powder was put into a cuvette 20 mm in diameter and 2 mm thick. The electric current is 15 mA, the operating voltage is 40 kV, the survey was carried out with an X-ray tube with a Si-anti-cathode. The resulting diffractogram was processed according to the PDXL-2 program. The mineral phases and their amount in the sample were determined.

Chemical composition of granular phosphorites and iron oolites was studied by X-ray spectral microanalysis in the Department of Petrology and Volcanology, Faculty of Geology of Moscow State University (analyst-researcher – V. O. Yapaskurt), using an analytical complex with a combined system of microanalysis, based on an electron scanning microscope Jeol IT-500 with energy dispersive spectrometer.

Results

Our research indicates that phosphate accumulation covers approximately 45 meters in the studied interval of the Moyero river section (outcrops 70 and 71, Figure 1B). However, the first appearance of phosphate minerals is noted even lower in the section in some nucleus of iron ooids (Figure 3), which compose a prominent layer at the base of the Volgino depositional sequence (Moyero formation, Volginian regional stage). This layer is interpreted as a transgressive lag at the base of the Transgressive Systems Tract of the sequence (Figure 1C and Figure 2). The Volginian deposits above this layer are represented by intercalation green-colored aleurolites and bioclastic limestones. Among these rocks, phosphate material is found only in bioclastic limestones as fragments of phosphatic brachiopods (Figure 3). Content of phosphatic components in these limestones is less than 1%.

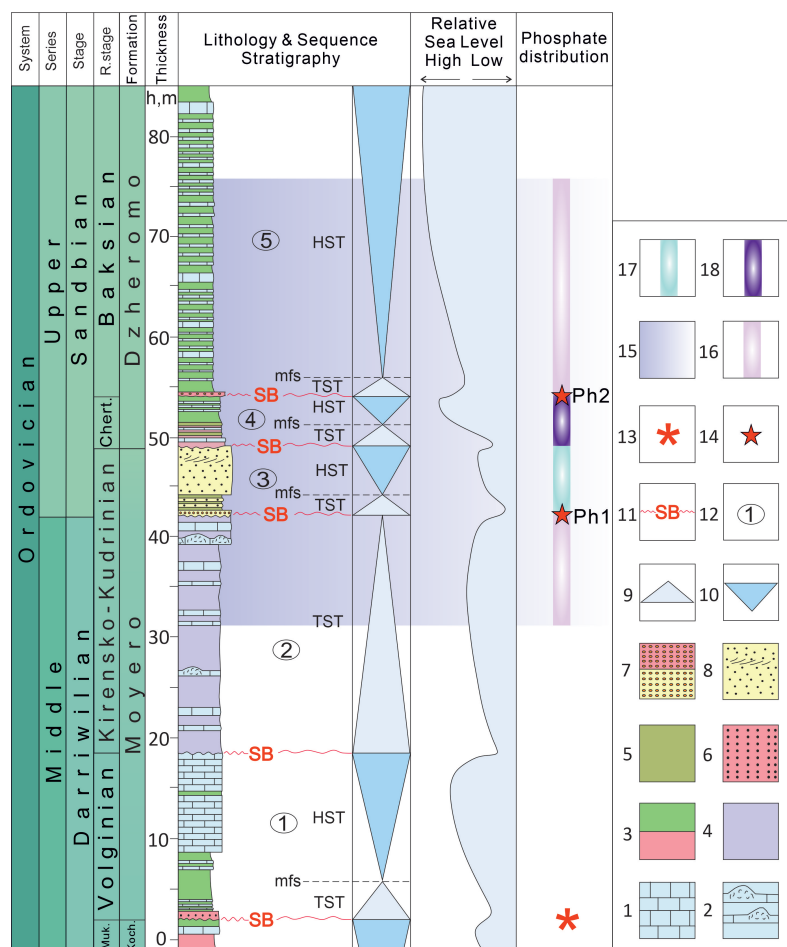


Figure 2. Simplified lithology and stratigraphy column of the studied section (Chert. = Chertovskian; Muk. = Mukteian; Koch = Kochakan). 1. Limestones. 2. Carbonate bioherms and banks. 3. Greenish and reddish aleurolites and argillites. 4. Violet and multi-coloured dolomitized aleurolites. 5. Greenish aleurolites with phosphate grains. 6. Iron oolites. 7. Granular phosphorites (reddish is hematized). 8. Sandstones with and without crossbedding. 9. Deepening upward succession. 10. Shallowing upward succession. 11. Sequence boundaries. 12. Sequences: 1) Volgino sequence; 2) Kirensk sequence; 3) Kudrino sequence; 4) Chertovskaya sequence; 5) Baksa sequence; 13. First appearance of sedimentary phosphate in the section; 14. Peaks of phosphate accumulation (2nd type accumulation); 15–18 – Phosphate distribution in the section: 15. Interval of continuous phosphate (Ph.) accumulation; 16. 1st type Ph. accumulation in limestones; 17. 3rd type Ph. accumulation in sandstones; 18. 4th type Ph. accumulation in limestones, aleurolites and argillites. TST – Transgressive Systems Tract; mfs – maximum flooding surface; HST – Highstand Systems Tract.

The Kirensko-Kudrinian regional stage is clearly divided into two parts separated by a regional erosional unconformity which corresponds to the Middle/Upper Ordovician boundary (Figure 2). It consists of the two depositional sequences: Kirensk and Kudrino [Dronov, 2013]. The lower Kirensk sequence is represented by the intercalation of violet and red lagoonal quartz aleurolites with a carbonate matrix and light-gray limestones. The types of limestones vary throughout the section. At the lower part of the section limestones are represented by bioclastic grainstones with calcite peloids. Upwards the section they pass into oolitic grainstones, above which lie calcimicrobe–stromatoporoid bioherms (the 3rd limestone layer of the Kirensk depositional sequence on Figure 2). At the top of these deposits, corresponding to the end of the Darriwilian, phosphatic grains appear in bioclastic limestones (the 4th limestone layer of the Kirensk depositional sequence on Figure 2 and Figure 4A). Those grains are represented by peloids and ooids of phosphatic

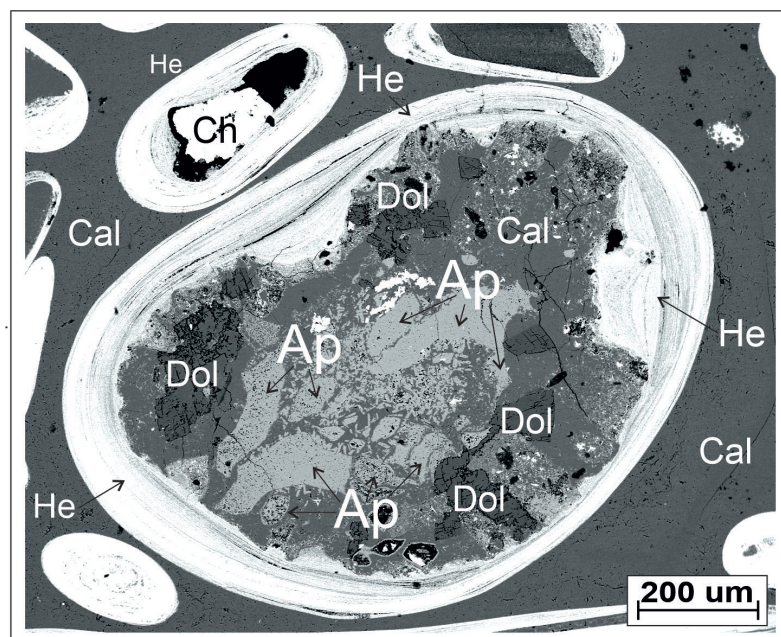


Figure 3. SEM image of the iron ooid from the transgressive lag at the base of the Volgino sequence. Ap – fluorapatite, He – hematite, Cal – calcite, Dol – dolomite, Ch – chalcopyrite.

composition. The content of phosphate matter in carbonates increases to 5–10%, in contrast to the sediments of the Volgino sequence. The Kirensk sequence is represented only by a Transgressive Systems Tract bounded by unconformities at the base and at the top.

At the base of the next Kudrino depositional sequence, there is a thin (20 cm) layer of phosphate conglomerate and/or granular phosphorite, which is interpreted as a transgressive lag deposit at the base of a Transgressive Systems Tract of this sequence (Figure 4B). That is the first maximum of the phosphate accumulation in the Moyero river section. An optical study showed that the phosphorite is gray-colored and non-layered. Grain sizes vary from silty to small-pebble size. The most common grain size is 0.15–0.35 mm. The rock is composed of 85% of phosphate material sometimes with bioclastic components (phosphatic brachiopods). The remaining 15% consists of subrounded quartz and feldspar grains of silt and sand size. The intraclasts are fragments of reworked sediments, composed of phosphatic material with or without clastic admixture, as well as phosphatic ooids and quartz pebbles. This phosphorite is cemented by clearly crystalline calcite (sparite).

The Kudrino depositional sequence is represented by quartz sandstones. In the lower two meters of the sequence, interpreted as a Transgressive Systems Tract, sandstone beds (from 2 to 7 cm thick) are intercalated with thin layers of aleurolites. The top surfaces of sandstones layers demonstrate ripple marks, while the base of the layers reveals trace fossils *Cruziana* and *Rusophycus*. In thin sections of these sandstones there are numerous phosphate ooids, peloids and fragments of phosphatic brachiopods. (Figure 4C). The upper seven meters of the sequence is represented by relatively thick (20–30 cm) layers of quartz sandstone with horizontal and/or cross-stratification and vertical *Skolithos* burrows. It is interpreted as a Highstand Systems Tract of the Kudrino depositional sequence. The change in the ichnofossil association indicates a shallowing upwards the section. The sandstones in this part of the section contain phosphate grains and phosphatized ostracod shells (Figure 4D).

In the next Chertovskaya depositional sequence despite a prominent shift in sedimentary environment from a shallow-water near-shore to relatively deep-water off-shore [Dronov, 2013] phosphate accumulation persists. The base of the Chertovskaya depositional sequence is represented by an unconformity which marks the sequence boundary coinciding with the transgressive surface. Lithologically, it is marked by an abrupt change from fine-grained shallow-water quartz sandstones (the underlying Kirensko-Kudrinian

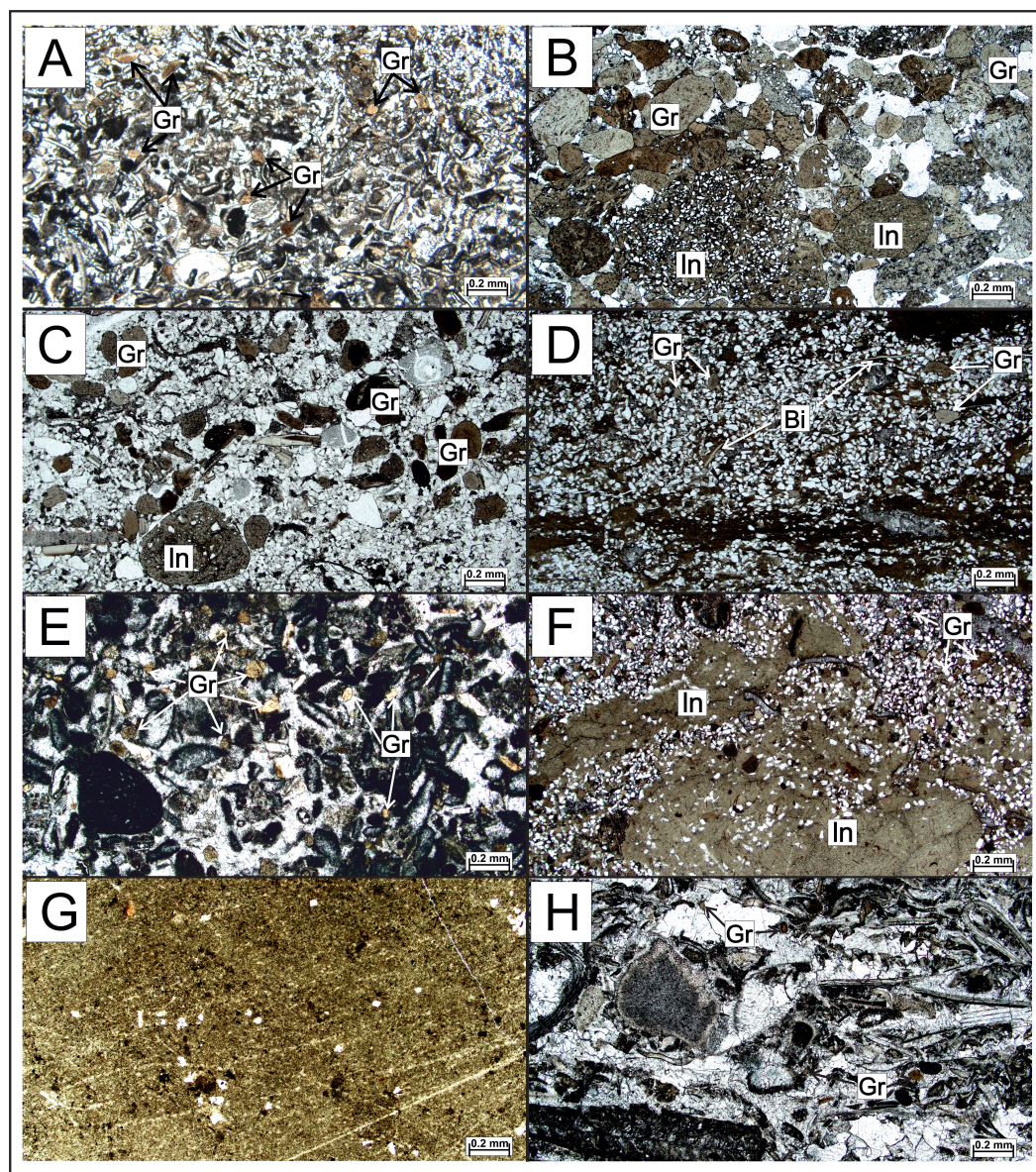


Figure 4. Phosphate materials in the studied deposits. Photos of the thin sections without an analyzer: In – intraclasts; Gr – grains; Bi – bioclasts. A – phosphatic grains in bioclastic limestone; B – granular phosphorite (Ph1); C – sandstones with phosphatic grains; D – sandstones with phosphatic grains and phosphatised ostracod shells; E – limestone with phosphatic grains; F – aleurolites with phosphatic grains and intraclasts; G – argillites with cryptocrystalline phosphate material and phosphatic grains; H – limestone with phosphate grains.

regional stage) to cherry-brown relatively deep-water argillites. This part of the sequence is interpreted as a Transgressive Systems Tract. The upper part of the sequence, interpreted as a Highstand Systems Tract is composed of green argillite and aleurolite with carbonate cement intercalated with interlayers of bioclastic wackestone or packstone (Figure 4E). Bioclastic limestone contains phosphatic grains (Figure 4F). In the argillites was found an admixture (according to an X-ray phase analysis) of phosphatic matter, the content of which could reach up to 15%. Phosphatic matter is represented by cryptocrystalline material (Figure 4G) dispersed in the clay matrix. The number of carbonate layers increase upwards the section.

A layer (15 cm) with lenses of hematitized granular phosphorites (thickness ranging from 2 to 8 cm) is observed at the base of the next Baksa depositional sequence and

interpreted as transgressive lag deposits. It represents the second peak of phosphate accumulation (Figure 2). Optical microscopy studies (Figure 5A) show that the phosphorite bed consists of phosphate grains represented by ooids, fragments of inarticulate brachiopods and intraclasts within a clear-crystalline (sparite) calcite cement. In addition, the rock contains sand-sized grains of quartz and calcareous biogenic components. The phosphorite also contains secondary dolomite, barite, and chalcopryrite. Phosphate grains (mainly ooids) are partially or completely covered with hematite films (Figure 5B).

Overlying deposits of the Baksa depositional sequence are similar to the underlying Highstand Systems Tract deposits of the Chertovskaya sequence (Figure 4H). Phosphate matter from bioclastic limestones layers disappears in the middle part of the Baksonian regional stage. According to the X-ray diffraction analyses and the X-ray spectral microanalyses the studied phosphate material is represented by fluorapatite.

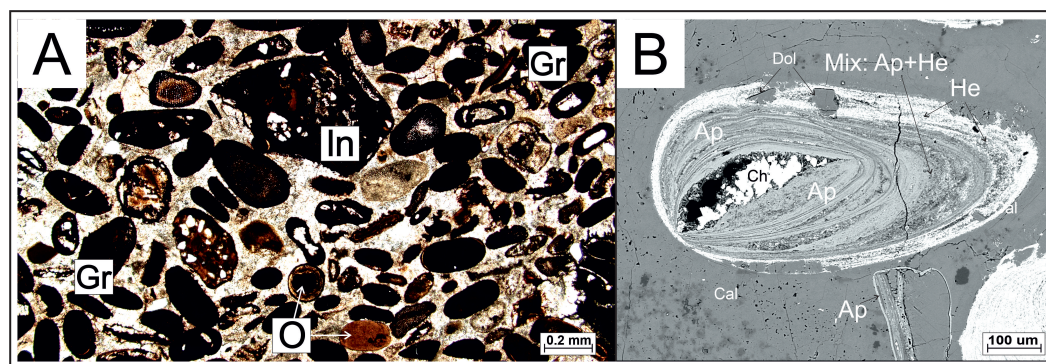


Figure 5. Hematitized granular phosphorite (Ph2) from the base of the Baksa depositional sequence. A) Thin section: Gr – phosphate grains, O – hematitized phosphate ooids, In – phosphate intraclasts. B) SEM image: Ap – fluorapatite, He – hematite, Cal – calcite, Dol – dolomite, Ch – chalcopryrite, Mix – mixture of fluorapatite and hematite.

The layer with hematitized phosphate ooids at the base of the Baksa depositional sequence is similar to the layer of iron ooids (transgressive lag deposits) at the base of the Volgino depositional sequence where the first appearance of phosphate matter was recorded (Figure 2), [Markov, 1969]. However, A continuous interval (45 m) with an increased amount of phosphate matter (“Phosphate Accumulation zone”) started only in the middle of the Kirensk depositional sequence and terminated in the middle of the Baksa depositional sequence during the Middle-Upper Ordovician transition (Figure 2). This zone can be divided into several types of phosphate accumulations in rocks (relative to facies variability)

The 1st type representing the onset of the “Phosphate Accumulation Zone”, is characterized by the initial appearance of phosphatic grains as an admixture within the limestone layers. The 2nd type represents the peaks of phosphate accumulation: Ph1 and Ph2. A phosphorite layer (Ph1) composed of reworked phosphate material. It represents a transgressive lag deposit of the Kudrino depositional sequence and rests directly on its erosional lower boundary. The next 3rd type of phosphate accumulation is associated with the Highstand Systems Tract deposit of the Kudrino depositional sequence and is represented by quartz sandstone containing phosphate grains and phosphatized ostracod shells. During the next Chertovskaya sequence of phosphate accumulation due to the sea-level rise and change in the sedimentation regime, clays enriched with cryptocrystalline phosphate material and individual layers of limestones and aleurolites with phosphate grains, were deposited – 4th type. The second peak of phosphate accumulation (2nd type), like the first, represented by a phosphorite layer (Ph2) with an erosional lower boundary, composed of repeatedly reworked phosphate material. It represents a transgressive lag deposit at the base of the Baksa depositional sequence. Upwards the section the accumulation of phosphates (1st type) gradually decreases and terminates in the first half of the Baksa sequence. Phosphate material here is in the form of phosphate grains and bioclasts in limestone layers.

It should be noted that the peaks of phosphate accumulation are associated with the formation of layers of granular phosphorites at the sequence boundaries coinciding with transgressive surfaces [Kanygin *et al.*, 2010]. Thus, the highest enrichment of sediments with phosphate material coincides with a relative rise in sea level.

Discussion

Marine upwelling is one of the major physical processes responsible for the marine primary productivity rise. That is why its distribution in the Ordovician is so important for understanding the “Great Ordovician Biodiversification Event”. There were several attempts to reconstruct possible oceanic circulation patterns, surface water currents and upwelling zones in the Ordovician [Christiansen and Stouge, 1999; Servais *et al.*, 2014; Wild, 1991]. The most reliable reconstruction was first introduced by Christiansen and Stouge [Christiansen and Stouge, 1999] and later modified by Rasmussen *et al.*, [Rasmussen *et al.*, 2016] (Figure 6). This reconstruction based on modern analogues demonstrates an upwelling zone on the Siberian margin. Our regional data supports this reconstruction.

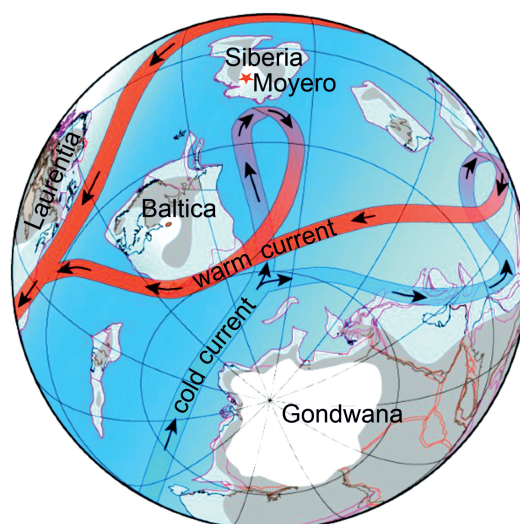


Figure 6. Simplified ocean current circulation model for the Middle Ordovician Southern Hemisphere based on Rasmussen *et al.* [2016]. Blue belt in the Iapetus Ocean (left) shows proposed Middle Ordovician cool, deep-water countercurrent the inflow toward north along Siberia, with an upwelling along the shelf and around the intra-Iapetus Ocean Island arcs. Red bands – warm surface water circulation; blue bands – cold deep ocean water circulation; red borders – continental shelf-ocean boundaries; black border – outline of the present-day Scandinavian and Baltic land-sea boundaries; light blue – the Middle Ordovician shallow sea; dark blue – Middle Ordovician deep ocean; gray – the Middle Ordovician exposed land areas; white – the Gondwana continent ice-covered south pole region.

The Siberian platform was situated in low latitudes, gradually migrating from the Southern Hemisphere during the Early Ordovician to the Northern Hemisphere by the Late Ordovician [Cocks and Torsvik, 2007]. However, despite its closer proximity to the equator, the platform exhibits evidence of cooling which starts already in the Middle Ordovician and reaches its maximum in the Upper Ordovician, which is represented by a series of cool-water carbonates [Dronov, 2013]. The most reliable explanation for this cooling is the invasion of cold deep oceanic waters into the tropical epicontinental basin of Siberia as a result of upwelling [Dronov, 2009, 2013]. Appearance of phosphorites in the upper Darriwilian – lower Sandbian interval of the Tungus basin in Siberia is one of the possible indicators of such an upwelling event. Like in East Siberia, the phosphate accumulation during the Middle-Late Ordovician transition is also observed in the Baltic region [Küpli *et al.*, 2010] in the same stratigraphic interval.

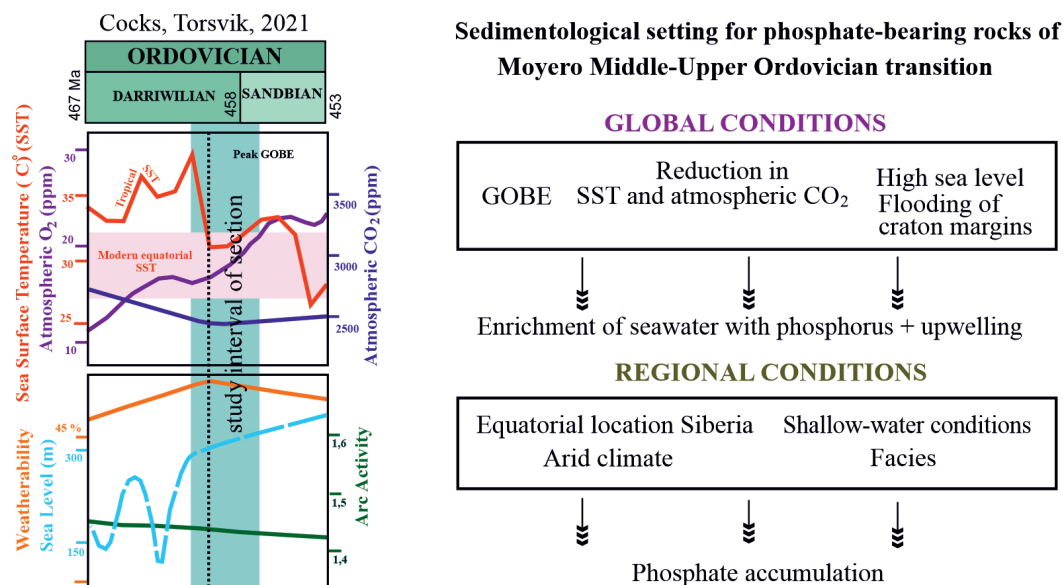


Figure 7. Sedimentological setting for phosphate-bearing rocks of the Moyero Middle-Upper Ordovician transition. GOBE – Great Ordovician Biodiversification Event, SST – sea surface temperature at the equator. The global conditions for the Middle-Late Ordovician transition are presented according to [Cocks and Torsvik \[2021\]](#).

The structural features of the studied phosphate-bearing rocks indicate the multi-stage and long-term nature of their formation. Granular phosphorites were deposited under conditions of redeposition and condensation of phosphate matter in the transgressive lag deposit above the sequence boundaries at the base of Kudrino and Baksa depositional sequences. Accumulation of granular phosphorites is obviously linked to abrupt sea level changes [[Kanygin et al., 2010](#)]. The first appearance of phosphate in the section is also localized in the transgressive lag deposit of the Volgino depositional sequence when the relative sea level was rapidly rising. The whole “Phosphate Accumulation Zone” coincides with a long-term eustatic rise of the global sea level ([Figure 7](#)) [[Haq and Schutter, 2008](#)]. The coastal upwelling on the Siberian margins seems to start earlier already in the Dapingian and ends later, probably in Hirnantian or the Early Silurian. However, “Phosphate Accumulation Zone” possibly reflects maximum invasion of the cold and phosphate-rich deep oceanic waters into the Tungus epicontinental basin. This invasion seems to coincide with the maximum of relative sea level rise in the basin.

The large-scale coastal upwelling during the Late Ordovician affected the shallow margins of a number of cratons [[Challands et al., 2009](#); [Pope and Steffen, 2003](#); [Saltzman and Young, 2005](#); [Young et al., 2008](#)]. Comparative analysis of the Ordovician successions of Siberia and Laurentia demonstrates a striking similarity in the long-term lithologic changes. On both palaeocontinents the Ordovician succession starts with tropical stromatolite-bearing carbonates which abruptly changes to siliciclastic deposits and terminates with cool-water carbonates [[Dronov, 2013](#); [Ettensohn, 2010](#)].

Similar to Laurentia the Siberian palaeocontinent was located in the tropical zone during the Cambrian, Ordovician and Silurian [[Cocks and Torsvik, 2007, 2021](#)]. Therefore, similar to Laurentia [[Dronov et al., 2015](#); [Holland and Patzkowsky, 1996](#); [Pope and Steffen, 2003](#); [Saltzman and Young, 2005](#)] the shift from tropical-type to temperate-type carbonates in the Middle and Late Ordovician of Siberia can be explained by an upwelling of cold oceanic waters into the intracratonic basin. The onset of cooling marked by the distribution of cool-water carbonates and phosphate-rich deposits starts earlier in Siberia (later Darriwilian – early Sandbian) than in Laurentia (early Katian). This observation demonstrates the importance of regional factors in the long-term global climate changes ([Figure 7](#)).

Phosphate accumulation relates to the upwelling, but its causes are a combination of both global and regional conditions. According to [Cocks and Torsvik \[2021\]](#) several global events occurred at the turn of the late Darriwilian and early Sandbian: the pick of GOBE, the reduction in sea surface temperature (SST) and atmospheric CO₂ ([Figure 7](#)). A combination of these global factors resulted in the enrichment of seawater with phosphorus. The reduction of SST caused the rise of CO₂ dissolving in the ocean, which also favored the rise in P₂O₅ enrichment in the ocean deep water. At the same time, due to regional conditions (equatorial location of Siberia, arid climate and facies), the cold, phosphate-rich waters of the World Ocean could have warmed as they ascended to the shallow settings of craton margins ([Figure 6](#)), contributing to the intensive accumulation of phosphates.

Conclusion

A 45 m interval of phosphorite accumulation has been found and studied in the Moyero river section. Based on forms of phosphatic matter manifestation and associated sediments we distinguish 4 types of phosphatic accumulations in the studied stratigraphic interval. This interval of intensive phosphate accumulation reflects the general patterns of climatic and oceanographic changes during the Ordovician period. The widespread phosphate-bearing rocks (phosphate rocks and phosphorites) in the Middle-Upper Ordovician transition suggest that the upwelling had a significant impact on this part of the Siberian platform during this time, against the background of favorable regional conditions of phosphorite accumulation.



Acknowledgments. The present study was supported by Russian Science Foundation (grant 20-17-00198) and Ministry of Science and Higher Education funding of Geological Institute RAS (project FMMG-2021-0003) and Geophysical Centre RAS (project 075-00443-24-01). This is a contribution to the IGCP 735 project “Rocks and the Rise of Ordovician Life”.

References

- Challands, T. J., H. A. Armstrong, D. P. Maloney, et al. (2009), Organic-carbon deposition and coastal upwelling at mid-latitude during the Upper Ordovician (Late Katian): A case study from the Welsh Basin, UK, *Palaeogeography, Palaeoclimatology, Palaeoecology*, 273(3–4), 395–410, <https://doi.org/10.1016/j.palaeo.2008.10.004>.
- Christiansen, J. L., and S. Stouge (1999), Oceanic circulation as an element in palaeogeographical reconstructions: the Arenig (early Ordovician) as an example, *Terra Nova*, 11(2–3), 73–78, <https://doi.org/10.1046/j.1365-3121.1999.00229.x>.
- Cocks, L. R. M., and T. H. Torsvik (2007), Siberia, the wandering northern terrane, and its changing geography through the Palaeozoic, *Earth-Science Reviews*, 82(1–2), 29–74, <https://doi.org/10.1016/j.earscirev.2007.02.001>.
- Cocks, L. R. M., and T. H. Torsvik (2021), Ordovician palaeogeography and climate change, *Gondwana Research*, 100, 53–72, <https://doi.org/10.1016/j.gr.2020.09.008>.
- Dronov, A. V. (2009), Upwelling in the Middle and Late Ordovician of the Siberian Platform and its connection to the evolution of Biota and Sediments, in *PALEOSTRAT-2009, Annual meeting of the paleontology section of MOIP and the Moscow branch of the paleontological society, Moscow, January 26-27, 2009, Program and abstracts of reports*, pp. 15–16, Palaeontological Institute of RAS, Moscow (in Russian).
- Dronov, A. V. (2013), Late Ordovician cooling event: Evidence from the Siberian Craton, *Palaeogeography, Palaeoclimatology, Palaeoecology*, 389, 87–95, <https://doi.org/10.1016/j.palaeo.2013.05.032>.
- Dronov, A. V., A. V. Kanygin, A. V. Timokhin, and T. V. Gonta (2015), Ordovician sequence stratigraphy of the Siberian Platform revised, in *The Ordovician Exposed: Short Papers, Abstracts, and Field Guides for the 12th International Symposium on the Ordovician System*, vol. 13(2), Society for Sedimentary Geology, <https://doi.org/10.2110/sepmord.015>.
- Ettensohn, F. R. (2010), Origin of Late Ordovician (mid-Mohawkian) temperate-water conditions on southeastern Laurentia: Glacial or tectonic?, in *The Ordovician Earth System*, Geological Society of America, [https://doi.org/10.1130/2010.2466\(11\)](https://doi.org/10.1130/2010.2466(11)).

- Frolov, V. T. (1993), *Lithology. Volume 2*, Moscow State University Press (in Russian).
- Haq, B. U., and S. R. Schutter (2008), A Chronology of Paleozoic Sea-Level Changes, *Science*, 322(5898), 64–68, <https://doi.org/10.1126/science.1161648>.
- Holland, S. M., and M. E. Patzkowsky (1996), Sequence stratigraphy and long-term paleoceanographic change in the Middle and Upper Ordovician of the eastern United States, in *Paleozoic sequence stratigraphy; views from the North American Craton*, Geological Society of America, <https://doi.org/10.1130/0-8137-2306-X.117>.
- Kanygin, A. V., A. G. Yadrenkina, A. V. Timokhin, T. A. Moskalenko, and O. V. Sychev (2007), *Stratigraphy of the oil and gas basins of Siberia. Ordovician of the Siberian platform*, 267 pp., Geo, Novosibirsk (in Russian).
- Kanygin, A. V., A. Dronov, A. Timokhin, and T. Gonta (2010), Depositional sequences and palaeoceanographic change in the Ordovician of the Siberian craton, *Palaeogeography, Palaeoclimatology, Palaeoecology*, 296(3–4), 285–296, <https://doi.org/10.1016/j.palaeo.2010.02.014>.
- Kanygin, A. V., A. G. Yadrenkina, A. V. Timokhin, et al. (2016), The regional stratigraphic chart of the Ordovician of the Siberian Platform, *Geology and mineral resources of Siberia*, (5s), 4–57, <https://doi.org/10.20403/2078-0575-2016-5s-4-57> (in Russian).
- Kiipli, E., T. Kiipli, T. Kallaste, and L. Ainsaar (2010), Distribution of phosphorus in the Middle and Upper Ordovician Baltoscandian carbonate palaeobasin, *Estonian Journal of Earth Sciences*, 59(4), 247, <https://doi.org/10.3176/earth.2010.4.01>.
- Krasilnikova, N. A., and A. I. Smirnov (1955), On the Ordovician phosphorites of the Siberian platform, in *Geology of Mining and Chemical Raw Materials. Proceedings of the Research Institute of Mining and Chemical Raw Materials. Issue 2*, Goskhimizdat, Moscow (in Russian).
- Krasilnikova, N. A., and A. I. Smirnov (1962), Prospectivity of phosphorite prospecting in the Old Paleozoic sediments of the Siberian platform, *Geology of phosphorite deposits. Transactions of State Research Institute of Mining and Chemical Raw Materials*, 7, 215–265 (in Russian).
- Markov, E. P. (1969), On lithological criteria for indication of the Central Tungus uplands in the Early Paleozoic, *Trudy SNIIGiMS*, 89, 141–145 (in Russian).
- Markov, E. P., and Y. N. Zanin (1979), Search for the ordovician grained phosphorites in the middle reaches of the Podkamennaya Tunguska river, *Soviet geology and geophysics*, (3), 100–104 (in Russian).
- Myagkova, E. I., O. I. Nikiforova, A. A. Vysotski, and A. B. Ivanovskii (1963), *Stratigraphy of the Ordovician and Silurian sediments of the Moyero River Valley, Siberian Platform*, Akademia nauk SSSR (in Russian).
- Myagkova, E. I., H. E. Nestor, and R. E. Einasto (1977), Ordovician and Silurian sequence of the Moiero River (Siberian platform), in *Transactions of the Institute of geology and geophysics*, p. 176, Nauka (in Russian).
- Pope, M. C., and J. B. Steffen (2003), Widespread, prolonged late Middle to Late Ordovician upwelling in North America: A proxy record of glaciation?, *Geology*, 31(1), 63, [https://doi.org/10.1130/0091-7613\(2003\)031<0063:WPLMTL>2.0.CO;2](https://doi.org/10.1130/0091-7613(2003)031<0063:WPLMTL>2.0.CO;2).
- Rasmussen, C. M. Ø., C. V. Ullmann, K. G. Jakobsen, et al. (2016), Onset of main Phanerozoic marine radiation sparked by emerging Mid Ordovician icehouse, *Scientific Reports*, 6(1), <https://doi.org/10.1038/srep18884>.
- Saltzman, M. R., and S. A. Young (2005), Long-lived glaciation in the Late Ordovician? Isotopic and sequence-stratigraphic evidence from western Laurentia, *Geology*, 33(2), 109, <https://doi.org/10.1130/G21219.1>.
- Servais, T., T. Danelian, D. A. T. Harper, and A. Munnecke (2014), Possible oceanic circulation patterns, surface water currents and upwelling zones in the Early Palaeozoic, *GFF*, 136(1), 229–233, <https://doi.org/10.1080/11035897.2013.876659>.
- Tolmacheva, T. Y., and A. V. Dronov (2008), The lower boundary of the Upper Ordovician on the East European and Siberian platforms, in *Geobiosphere events and history of the organic world. Abstracts of reports of the LIV session of the Paleontological Society of the Russian Academy of Sciences (April 7–11, 2008)* (in Russian).

- Trappe, J. (2001), A nomenclature system for granular phosphate rocks according to depositional texture, *Sedimentary Geology*, 145(1–2), 135–150, [https://doi.org/10.1016/s0037-0738\(01\)00103-8](https://doi.org/10.1016/s0037-0738(01)00103-8).
- Wild, P. (1991), Oceanography in the Ordovician, in *Advances in Ordovician Geology. Special paper of Geological Survey of Canada. Paper 90-9*, pp. 293–298, Geological Survey of Canada.
- Young, S. A., M. R. Saltzman, S. M. Bergström, S. A. Leslie, and C. Xu (2008), Paired $\delta^{13}\text{C}_{\text{carb}}$ and $\delta^{13}\text{C}_{\text{org}}$ records of Upper Ordovician (Sandbian-Katian) carbonates in North America and China: Implications for paleoceanographic change, *Palaeogeography, Palaeoclimatology, Palaeoecology*, 270(1–2), 166–178, <https://doi.org/10.1016/j.palaeo.2008.09.006>.
- Yudovich, Y. E., M. P. Ketris, and N. V. Rybina (2020), *Geochemistry of Phosphorus*, IG Komi SC UB RAS, Syktyvkar (in Russian).
- Zanin, Y. N., and V. G. Matukhina (Eds.) (1983), *Phosphorite and apatite deposits of Siberia and the Soviet Far East*, IGI SB AS USSR, Novosibirsk (in Russian).

АЛГОРИТМЫ АВТОМАТИЧЕСКОГО ДЕТЕКТИРОВАНИЯ И ЛОКАЦИИ
ИНФРАЗВУКОВЫХ СОБЫТИЙ В СИСТЕМЕ PSDLВ. Э. Асминг¹  и А. В. Федоров^{*},¹ ¹Кольский филиал ФИЦ ЕГС РАН, Апатиты, Россия^{*} **Контакт:** Андрей Викторович Федоров, Afedorov@krsc.ru

В работе представлено описание автоматизированной системы и реализованных в ней алгоритмов для обнаружения, ассоциации и локации низкочастотных акустических событий по данным инфразвуковых групп. Описан алгоритм обнаружения инфразвуковых сигналов методом расчета функции взаимной корреляции между записями отдельных датчиков группы. Реализованный алгоритм оптимизирован для работы с группами, состоящими из большого количества сенсоров, что позволяет минимизировать вычислительную нагрузку на систему мониторинга в режиме, близком к реальному времени. Описана процедура распознавания длительных сигналов с возможно меняющимся во времени положением источника, таких как движущийся транспорт или снежные лавины. Также в работе приводится описание алгоритмов ассоциации инфразвуковых сигналов, зарегистрированных разными группами, а также локации источника сигнала по данным нескольких инфразвуковых групп. Система способна анализировать одновременно данные сейсмического и инфразвукового мониторинга и обнаруживать пары сигналов двух видов, ассоциируемых с общим источником. Алгоритм такой ассоциации также приведен в работе. Описанная система автоматического обнаружения и локации инфразвуковых сигналов может быть применена для мониторинга опасных природных и техногенных процессов и явлений в режиме, близком к реальному времени.

Ключевые слова: инфразвуковой сигнал, инфразвуковая группа, детектирование, локация, кросс-корреляция.

Цитирование: Асминг, В. Э., А. В. Федоров Алгоритмы автоматического детектирования и локации инфразвуковых событий в системе PSDL // Russian Journal of Earth Sciences. — 2024. — Т. 24. — ES6002. — DOI: 10.2205/2024es000944 — EDN: ZVUUJP

Введение

Многие опасные природные и техногенные явления сопровождаются как сейсмическими, так и акустическими сигналами. Наиболее распространенный класс таких событий – это взрывы различной природы – от промышленных [Arrowsmith et al., 2008] до ядерных [Koch and Pilger, 2018]. Также инфразвуковые волны, наряду с сейсмическими, порождаются сильными землетрясениями [Mutschlecner and Whitaker, 2005], извержениями вулканов [Le Pichon et al., 2005], льдотрясениями и процессами откола айсбергов [Асминг и др., 2016; Виноградов и др., 2021]. Пролеты сверхзвуковых летательных аппаратов [Liszka and Waldemark, 1995] и болидов [Ens et al., 2012] также порождают сильные инфразвуковые волны.

Для мониторинга низкочастотных акустических сигналов используются инфразвуковые группы (наборы разнесенных в пространстве низкочастотных микрофонов или микробарографов) [Gibbons et al., 2015]. Апертуры инфразвуковых групп варьируют от первых сотен метров до первых километров. Примеры конфигураций инфразвуковых групп, установленных в Северной Европе, показаны на рис. 1 (буквенно-числовой код обозначает международный код станции).

<https://elibrary.ru/zvuujp>

Получено: 4 октября 2024 г.

Принято: 23 октября 2024 г.

Опубликовано: 30 декабря 2024 г.



© 2024. Коллектив авторов.

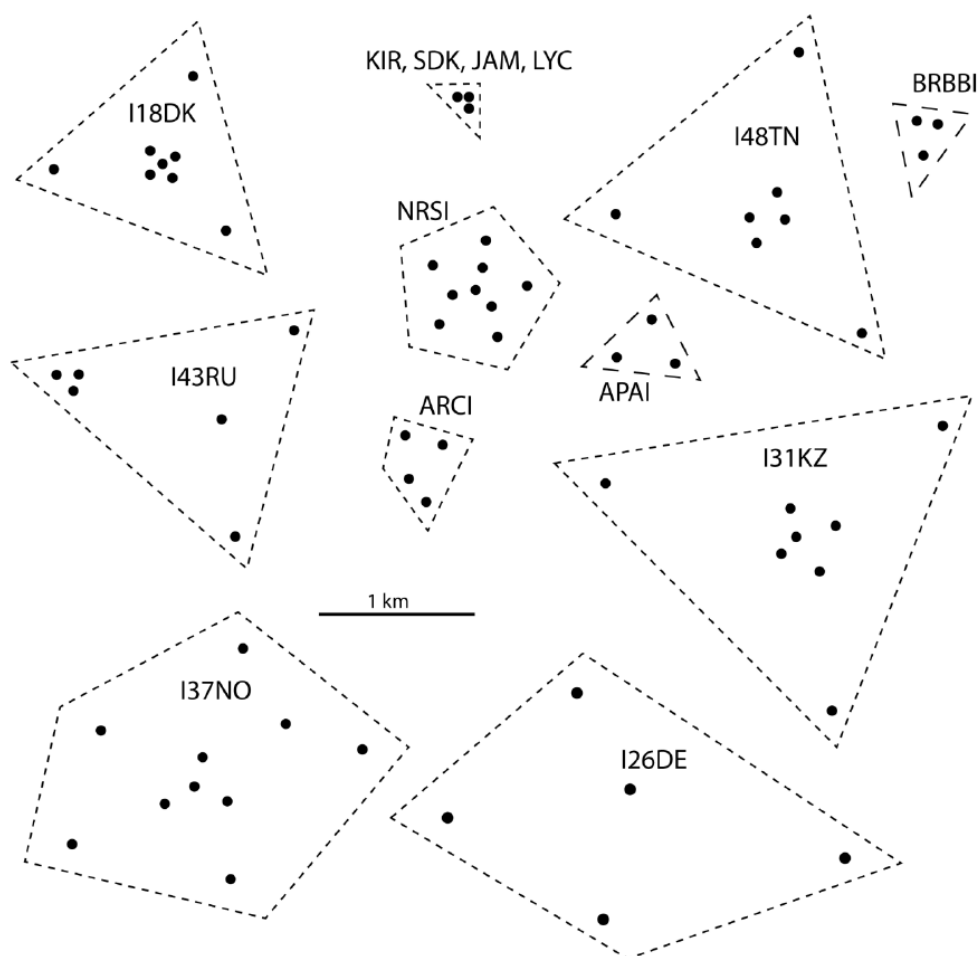


Рис. 1. Конфигурации различных инфразвуковых групп, установленных в Северной Европе [Gibbons et al., 2015].

Перечень задач, которые решаются сетями инфразвукового наблюдения, включает в себя не только вопросы мониторинга природных и техногенных процессов и явлений. По данным регистрации инфразвука зондируется строение атмосферы на трассах распространения инфразвукового сигнала, изучаются глобальные планетарные атмосферные циркуляции и их аномалии, такие, например, как внезапное стратосферное потепление [Infrasound Monitoring for Atmospheric Studies: Challenges in Middle Atmosphere Dynamics and Societal Benefits, 2019].

Для решения такого широкого круга задач, связанных с инфразвуковыми наблюдениями, крайне важно максимально автоматизировать процессы обнаружения и первичного анализа целевых сигналов. Создание автоматизированных систем инфразвукового и сейсмоинфразвукового мониторинга, характеризующихся высокой достоверностью результатов, позволит в режиме близком к реальному времени решать прикладные задачи связанные с наблюдением за опасными природными явлениями и оперативным реагированием на них.

В 2022–2024 годах в Кольском филиале ФИЦ ЕГС РАН была разработана потоковая система автоматического детектирования и локации (ПСДЛ/PSDL), предназначенная для организации сейсмического и инфразвукового мониторинга произвольных регионов [Асминг и Асминг, 2022].

Система включает в себя две подсистемы – детектирования и локации сейсмических и инфразвуковых событий. Эти подсистемы взаимосвязаны – в случае, когда за сейсмическим сигналом следует соответствующий ему инфразвуковой, происходит их ассоциация.

В настоящее время система рутинно используется в ФИЦ ЕГС РАН для решения следующих задач:

- обработка данных сети сейсмических и инфразвуковых станций, включающей станции Кольского полуострова, северной Норвегии и Финляндии;
- обработка сейсмических и инфразвуковых данных сети архипелага Шпицберген. Обнаруживаются и лоцируются землетрясения, льдотрясения, отколы айсбергов, микробаромы и т.д.;
- обработка данных сейсмоинфразвуковой группы, расположенной на архипелаге Земля Франца-Иосифа для изучения процессов деструкции местных ледников;
- обработка инфразвуковых данных трех инфразвуковых групп, расположенных в Хибинском горном массиве и его окрестностях. Система позволяет обнаруживать промышленные взрывы и сходы снежных лавин.

Решение задачи автоматизации дистанционного мониторинга снежных лавин и дискриминации событий этого класса от событий иной природы также во многом может быть найдено в комплексировании анализа инфразвуковых и сейсмических сигналов. Отчасти эта работа посвящена решению именно таких задач, когда совместный анализ сейсмических и инфразвуковых записей позволяет получать дополнительную информацию для автоматизации процессов классификации событий по природе их генерации.

Упомянутый выше программный комплекс PSDL включает в себя четыре модуля. Первый – NSS (New Single Station), обрабатывает данные отдельных сейсмических станций или групп. Для каждой станции запускается отдельный экземпляр модуля, все они работают параллельно. Второй программный модуль – NAS (New ASsociation), ассоциирует результаты работы модулей NSS, лоцирует сейсмические события по сети станций, производит вероятностную оценку типов сейсмических событий. Третий – модуль быстрого инфразвукового детектирования QACD (Quick ACoustic Detector). Один экземпляр модуля обрабатывает данные одной инфразвуковой группы, все экземпляры работают параллельно. Четвертый модуль – ASIS (ASsociation of Infrasound Signals), обобщает данные, полученные от экземпляров QACD и лоцирует инфразвуковые события по сети.

Информация о сейсмических событиях, обнаруженных модулями NSS и NAS, передается в инфразвуковые модули. Если инфразвуковому событию соответствует сейсмическое, между ними производится ассоциация.

В настоящей статье рассматриваются алгоритмы детектирования инфразвуковых событий отдельными группами, ассоциации событий по нескольким группам, локации событий и оценок ошибок локации, которые реализованы в модулях QACD и ASIS программы PSDL.

Детектирование инфразвуковых событий

Когда инфразвуковой сигнал приходит на группу с расстояния, намного большего, чем апертура группы, его можно рассматривать в приближении плоской волны. В этом случае записи на разных датчиках группы похожи, но сдвинуты друг относительно друга по времени (рис. 2). Если известны временные сдвиги между приходами сигналов на разные датчики группы, по ним можно рассчитать азимут подхода сигнала и кажущуюся скорость подхода (кажущаяся скорость – отношение $V_{\text{звука}}/\cos(\beta)$, где β – угол падения волны к дневной поверхности).

Важным параметром в детектировании и локации инфразвуковых сигналов является кросс-корреляция записей разных датчиков группы. Определим кросс-корреляцию каналов в зависимости от предполагаемого азимута прихода волны α и кажущейся скорости v :

$$C(\alpha, v) = \sum_{i,j} \text{Corr}(S_i(t - \Delta t_i(\alpha, v)), S_j(t - \Delta t_j(\alpha, v))),$$

где i, j – индексы датчиков, $S_i(t)$ – запись на i -м датчике, $\Delta t(\alpha, v)$ – сдвиг относительно центра группы в зависимости от азимута и кажущейся скорости. Корреляция (Corr) считается для временного интервала $[t_1, t_2]$.

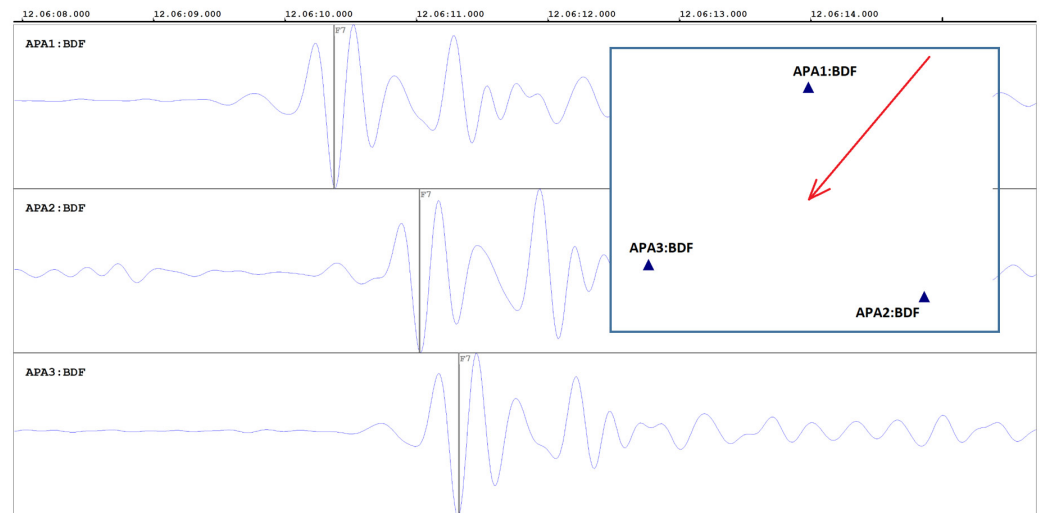


Рис. 2. Запись инфразвукового сигнала на датчиках Апатитской группы (АРА). Записи имеют высокое подобие, но сдвинуты по времени. По сдвигам сигнала на разных каналах определен азимут подхода волны. Красной стрелкой показано направление прихода волны.

Детектирование с помощью кросс-корреляции будет заключаться в поиске $\max_{\alpha, v} C(\alpha, v)$ для каждого небольшого временного окна. Если этот максимум превысит определенный порог, инфразвуковое событие может считаться обнаруженным, а значения α и v , на которых максимум достигнут, и будут оценками азимута на источник и кажущейся скорости для данного временного окна.

На практике сигналы, записанные датчиками, расположенными близко друг к другу, имеют более высокую корреляцию, чем записанные удаленными датчиками одной и той же группы. Это хорошо заметно при работе с данными инфразвуковых групп больших апертур (от 0,5 км и выше).

Для учета этого эффекта при работе с такими инфразвуковыми группами авторами было предложено учитывать попарные корреляции с весами, уменьшающимися с расстоянием между датчиками:

$$C(\alpha, v) = \frac{\sum_{i,j} w(R_{i,j}) \text{Corr}(S_i(t - \Delta t_i(\alpha, v)), S_j(t - \Delta t_j(\alpha, v)))}{\sum_{i,j} w(R_{i,j})}.$$

Здесь $w(R_{i,j})$ – эмпирическая весовая функция, зависящая от расстояния между парой датчиков $R_{i,j}$.

Аналогичным образом введем функцию G (gain), имеющую смысл выигрыша в амплитуде при суммировании каналов инфразвуковой группы со сдвигами на интервале $[t_1, t_2]$:

$$G_{ij}(\alpha, v) = \frac{\max_{t \in [t_1, t_2]} (S_i(t - \Delta t_i(\alpha, v)) + S_j(t - \Delta t_j(\alpha, v)))}{2 \max(\max_{t \in [t_1, t_2]} S_i, \max_{t \in [t_1, t_2]} S_j)}, \quad (1)$$

$$G(\alpha, v) = \frac{\sum_{i,j} w(R_{i,j}) G_{ij}(\alpha, v)}{\sum_{i,j} w(R_{i,j})}.$$

Введем аналогично функцию амплитуды $A(\alpha, v)$ на интервале $[t_1, t_2]$:

$$A_{ij}(\alpha, v) = \frac{1}{2} \max_{t \in [t_1, t_2]} |S_i(t + \Delta t_i(\alpha, v)) + S_j(t + \Delta t_j(\alpha, v))|, \quad (2)$$

$$A(\alpha, v) = \frac{\sum_{i,j} w(R_{i,j}) A_{ij}(\alpha, v)}{\sum_{i,j} w(R_{i,j})}.$$

Рассмотрим теперь процедуру детектирования в том виде, как она реализована в программе PSDL. Исследуемый фрагмент данных разбивается на короткие (длительностью 2–3 сек) временные окна и для каждого положения окна рассчитываются параметры $C(\alpha, v)$ (корреляция), $G(\alpha, v)$ (gain) и $A(\alpha, v)$ (амплитуда) для большого количества наборов углов и кажущихся скоростей (α, v) (о выборе этих наборов будет сказано ниже).

Будем считать, что во временном окне обнаружен сигнал, если для какой-либо пары азимута и скорости (α, v) выполняется одно из следующих условий:

$$(C(\alpha, v) > C_0) \& (G(\alpha, v) > G_0) \& (A(\alpha, v)/A_{\text{шум}} > A_0) \quad (3)$$

или

$$(C(\alpha, v)G(\alpha, v) > C_0G_0) \& (A(\alpha, v)/A_{\text{шум}} > A_0), \quad (4)$$

где C_0 – порог по корреляции, G_0 – порог по амплитудному выигрышу, A_0 – порог по отношению сигнал/шум (об оценке уровня шума $A_{\text{шум}}$ будет сказано ниже).

В качестве параметров сигнала в этом случае берутся те (α, v) , на которых достигается максимум $C(\alpha, v)G(\alpha, v)$.

Расчет по формулам, (1) и (2) для всех пар датчиков может быть вычислительно затратен. Например, для группы, состоящей из четырёх датчиков, необходимо учесть шесть пар. На практике достаточно из всех пар выбрать две – наиболее близких датчиков. В случае высокой корреляции на этих двух парах можно посчитать и общую корреляцию по всем. Если корреляция по двум парам будет низкой, то и по всем парам она окажется низкой, и вычислять ее не будет необходимости.

Таким образом, детектирование инфразвуковых сигналов в программе PSDL производится в два этапа. На первом рассчитываются корреляции, амплитудные выигрыши и амплитуды для минимальных наборов пар датчиков. Если проверка пройдена, т.е. выполнены условия (3) или (4), производится расчет уже по полному набору пар датчиков для уточнения параметров сигнала.

Такой алгоритм детектирования является эффективной альтернативой известного метода РМСС (Progressive Multi-Channel Correlation) [Cansi and Le Pichon, 2008].

Оценка уровня шума

Как сказано выше, для каждого положения короткого окна считается амплитуда A_i , здесь i – индекс (номер) скользящего окна. В конфигурационном файле программы задается число окон N , по которым рассчитывается шум.

Для первых N окон за шум принимается средняя амплитуда в этих окнах:

$$A_{\text{шум}}(N) = \frac{1}{N} \sum_{i=1}^N A_i.$$

С появлением новой амплитуды шум пересчитывается:

$$A_{\text{шум}}(K+1) = \frac{(N-1)A_{\text{шум}}(K) + A_{K+1}}{N}. \quad (5)$$

После того, как в окне обнаружен сигнал (выполнены условия (3) или (4)) обновление шума по формуле (5) отключается до тех пор, пока не закончится сигнал.

Объединение фрагментов в сигнал

Запись инфразвукового сигнала может содержаться в нескольких коротких окнах, сигнал может прерываться или временно затухать. В длительных сигналах, генерируемых движущимся источником, может со временем меняться азимут на источник. Для анализа таких сложных случаев и корректного объединения окон, содержащих продолжительный сигнал, используется следующий подход. Вначале в списке обработанных окон выбирается «активное» окно, это окно не должно являться последним в списке.

Далее начинается анализ окон слева и справа от него в поисках окон, полностью совместимых с данным. Под «полностью совместимым» окном понимается окно, в котором также превышены пороги по корреляции и выигрышу, а азимуты и время отличаются от исходных не больше, чем на предварительно заданные в конфигурационном файле величины. Интервал между первым и последним полностью совместимыми окнами считается интервалом события.

По всем участкам, объединенным в единый сигнал, вычисляется диапазон азимутов и рассчитывается изменение азимута за время прохождения сигнала. Оно может оказаться больше максимального расхождения по азимуту, заданного пользователем.

Иногда возникают ситуации, при которых внутри выделенного таким образом интервала (события) есть фрагменты с другими параметрами, также претендующие на роль событий (т.е. имеющие высокие значения корреляции и выигрыша). Возможен режим работы программы, в котором такие фрагменты рассматриваются как отдельные события.

Ассоциация с сейсмическими событиями

В PSDL локация сейсмических событий происходит как при одностанционной обработке в модуле NSS, так и после ассоциации при многостанционной обработке в модуле NAS. В различных конфигурациях программы ассоциация инфразвуковых сигналов может выполняться как с результатами одностанционной, так и сетевой обработки сейсмических данных.

Параметры ассоциации задаются в конфигурационном файле программы. Это максимальное расхождение азимутов $\Delta\alpha$, а также минимальные и максимальные скорости пробега звуковой волны (celerities) – c_0 и c_1 .

Пусть инфразвуковой группой с координатами (φ_g, λ_g) было зарегистрировано событие, записанное в отрезок времени $[t_{g0}, t_{g1}]$, азимуты на источник, рассчитанные для этого события по этой группе, находятся в интервале $[\alpha_{g0}, \alpha_{g1}]$. Опишем процедуру ассоциации этого инфразвукового события с сейсмическим, произошедшим в точке с координатами (φ, λ) в момент времени t_0 .

Обозначим $d = \text{Dist}(\varphi_g, \lambda_g, \varphi, \lambda)$ – расстояние между сейсмическим событием и инфразвуковой группой, α – азимут из инфразвуковой группы на сейсмическое событие.

Инфразвуковое событие будем считать ассоциированным с данным сейсмическим, если:

$$\left[t_0 - \frac{d}{c_1}, t_0 - \frac{d}{c_0} \right] \cap [t_{g0}, t_{g1}] \neq \emptyset$$

и

$$[\alpha - \Delta\alpha, \alpha + \Delta\alpha] \cap [\alpha_{g0}, \alpha_{g1}] \neq \emptyset.$$

В этом случае инфразвуковому событию приписываются координаты сейсмического, а в бюллетень и в базу данных добавляется информация об ассоциации.

Предварительный расчет, оценка неустраняемых ошибок определения азимутов

В начале работы программа производит подготовительный расчет. При этом программа перебирает азимуты с маленьким шагом $\Delta\alpha$ и скорости от V_0 до V_1 с маленьким шагом ΔV . Для каждого варианта (α, V) рассчитываются целочисленные сдвиги по времени сигналов, приходящих на датчики, относительно центра группы. Сдвиги вычисляются в отсчетах, поэтому возможны ситуации, когда одни и те же значения сдвигов получаются для нескольких разных (α_i, V_i) . В этом случае для этого набора сдвигов запоминаются средние значения азимутов и скоростей, а также диапазон ошибок по азимуту и скорости. К ошибкам по азимуту прибавляется $\Delta\alpha/2$ – ошибка за счет дискретности перебора азимутов.

Таким образом, после предварительного расчета для первого и второго проходов детектора хранятся следующие наборы данных – $(\Delta t_1, \dots, \Delta t_N, \alpha_{\text{центр}}, \delta\alpha, V_{\text{центр}}, \delta V)$, где Δt – целочисленные сдвиги каналов по времени относительно центра группы

в отсчетах, $(\alpha, V_{\text{центр}})$ – средний азимут и кажущаяся скорость, соответствующая этим сдвигам, $(\delta\alpha, \delta V)$ – неустранимые ошибки определения азимута и кажущейся скорости.

Отметим, что число этих наборов (вариантов сдвигов каналов) оказывается меньше, чем число перебираемых при начальном расчете пар (α, V) , потому что один и тот же вариант может соответствовать нескольким разным значениям (α, V) .

Ассоциация сигналов по нескольким инфразвуковым группам

Выбор наборов фаз

В результате работы модулей инфразвукового детектирования QACD формируется информация о приходах сигналов на станции (далее – о фазах). Для каждого прихода (i – индекс прихода) обозначим $[t_{i0}, t_{i1}]$ – интервал времени прихода сигнала на станцию, N_i – номер станции, на которой обнаружен приход, $[\alpha_{i0}, \alpha_{i1}]$ – диапазон азимутов прихода сигнала.

Процедура ассоциации выполняется каждый раз после того, как обнаруживается новая фаза. Вначале из списка ранее обнаруженных фаз выбираются все, которые совместимы с новой, т.е. могут в принципе быть порождены одним и тем же инфразвуковым событием. Это делается только по временам фаз. Для совместимости фаз 1 и 2 необходимо, чтобы для каких либо времен $t_1 \in [t_{10}, t_{11}]$ и $t_2 \in [t_{20}, t_{21}]$ выполнялось условие

$$|t_1 - t_2| < \frac{d_{12}}{c_{\min}}, \quad (6)$$

где d_{12} – расстояние между станциями 1 и 2, c_{\min} – минимальное значение скорости пробега (в смысле celerity) звука на расстоянии предполагаемой локации.

Обратим внимание, что (6) задает широкие рамки совместимости. Не все отобранные таким образом фазы в конечном итоге окажутся ассоциированными с одним и тем же событием.

Ассоциация инфразвуковых фаз

Будем рассматривать наборы фаз, отобранные из всего потока, как описано в предыдущем пункте.

Модуль ASIS ассоциирует сигналы в круге, центр и радиус которого задаются в конфигурационном файле параметрами φ_0 (широта центра), λ_0 (долгота центра) и R_1 (радиус области поиска). При этом область разбивается на перекрывающиеся круговые ячейки радиуса R_0 , для каждой из которых проверяется гипотеза, не произошло ли в данной ячейке инфразвуковое событие. Дополнительными параметрами ассоциации являются допустимое отклонение азимута $\Delta\alpha$ и порог T_0 .

Дальше будем обозначать (k -индекс ячейки, i -индекс станции, j -индекс события): (φ_0, λ_0) – координаты центра области поиска; (φ_k, λ_k) – координаты центра k -й ячейки; R_0 – радиус ячейки сетки; R_1 – радиус области поиска; c_0 – минимальная скорость пробега инфразвуковой волны; c_1 – максимальная скорость пробега инфразвуковой волны; $\Delta\alpha$ – допустимое отклонение азимута; $[t_{0ij}, t_{1ij}]$ – интервал времени, в котором на i -й станции обнаружено j -е событие; α_{ij} – азимут из i -й станции на j -е событие; β_{ik} – азимут из i -й станции на центр k -й ячейки; $\Delta\beta_{ik}$ – максимальное расхождение между β_{ik} и азимутом из i -й станции на край k -й ячейки; d_{ik} – расстояние от i -й станции до k -й ячейки.

В первых версиях алгоритма c_0 и c_1 были постоянными. В последних версиях это медленно меняющиеся функции, зависящие от расстояния от станции до события.

Ассоциация инфразвуковых сигналов, зарегистрированных на разных станциях, производится методом, идейно близким к Generalized Beamforming [Ringdal and Kværna, 1989]. Вычисляется рейтинг для ячейки k , то есть оценка предположения, что источник инфразвукового события находился в этой ячейке.

Просматриваются все сигналы (j) всех станций (i). Для каждого сигнала ij вычисляем вес того, что он произведен событием, случившимся в ячейке k :

$$w_{ij} = \begin{cases} 1, & |\alpha_{ij} - \beta_{ik}| \leq \Delta\beta_{ik} \\ 1 - \frac{|\alpha_{ij} - \beta_{ik}| - \Delta\beta_{ik}}{\Delta\alpha}, & \Delta\beta_{ik} < |\alpha_{ij} - \beta_{ik}| < \Delta\beta_{ik} + \Delta\alpha. \\ 0, & \text{в противном случае} \end{cases}$$

Другими словами, этот вес равен 1, если азимут на источник сигнала пересекает ячейку, меньше 1, если проходит рядом с ячейкой, и равен 0, если далек от ячейки.

Для сигналов с $w_{ij} > 0$ вычислим интервал времен, в который могло бы произойти событие, если оно случилось в ячейке k :

$$\left[t_{0ij} - \frac{d_{ik} + R_1}{c_0}, t_{1ij} - \frac{d_{ik} - R_1}{c_1} \right].$$

Характеристическую функцию сигнала w_{ij} определим, как:

$$f_{ij}(t) = \begin{cases} w_{ij}, & t \in \left[t_{0ij} - \frac{d_{ik} + R_1}{c_0}, t_{1ij} - \frac{d_{ik} - R_1}{c_1} \right] \\ 0, & \text{в противном случае} \end{cases}$$

Характеристическую функцию станции i определим, как максимум по всем сигналам, зарегистрированным этой станцией:

$$F_i(t) = \max_j f_{ij}(t).$$

Окончательно, рейтинг рассматриваемой ячейки R определяем, как:

$$R = \max_t \sum_i F_i(t).$$

Другими словами, рейтинг ячейки меньше или равен максимальному числу сигналов, зарегистрированных разными станциями (по одному на станцию), которые одновременно могут быть проассоциированы с данной ячейкой. Если рейтинг больше порога T_0 , сигналы, внесшие ненулевой вклад в рейтинг, считаются ассоциированными. За предварительную оценку координат берется центр ячейки. Ассоциированные сигналы изымаются из списка, и процедура ассоциации повторяется снова.

Уточнение локации ассоциированных фаз, оценка эллипса ошибок

На вход процедуры уточнения локации поступает информация о станциях, на которых обнаружен приход волны, для каждой станции – набор подходящих азимутов, ошибки их определения и веса (здесь веса – единицы или числа, немного их меньше, если азимут фазы попал не точно в ячейку, а отклонился от нее на угол, не превышающий $\Delta\alpha$).

Введем обозначения: N – число станций, для которых есть приходы. Индекс станции – i . Для каждой i -й станции: (φ_i, λ_i) – координаты станции, $N_{\text{азим}, i}$ – число азимутов у i -й станции (индекс j). Для каждого j -го азимута i -й станции: α_{ij} – j -й азимут i -й станции, ε_{ij} – неустранимая ошибка определения j -го азимута, w_{ij} – вес j -го азимута.

Введем функцию невязки по расстоянию в зависимости от предполагаемых координат события $\text{Err}(\varphi, \lambda)$:

$$\text{Err}(\varphi, \lambda) = \frac{\sum_{i=1}^{N_{\text{станций}}} \text{Dist}(\varphi_i, \lambda_i, \varphi, \lambda) w_{i, \min} \min_j (\| \text{Az}(\varphi_i, \lambda_i, \varphi, \lambda), \alpha_{ij} \| + \varepsilon_{ij})}{\sum_{i=1}^{N_{\text{станций}}} w_{i, \min}}.$$

Здесь $\text{Dist}(\varphi_1, \lambda_1, \varphi_2, \lambda_2)$ – расстояние между двумя точками по поверхности Земли; $\text{Az}(\varphi_1, \lambda_1, \varphi_2, \lambda_2)$ – азимут из точки 1 в точку 2; $\|\alpha_1, \alpha_2\|$ – угловая разность между азимутами α_1 и α_2 (0° – 180°).

Под $w_{i,\min}$ понимается вес $w_{i,j}$ для того j , на котором достигается указанный в формуле минимум.

Функция $\text{Err}(\varphi, \lambda)$ минимизируется по координатам, за исходную точку минимизации берется центр круговой ячейки, для которой была произведена ассоциация.

По окончании локации рассчитывается эллипс ошибок. Он строится следующим образом. В точке, куда пришел алгоритм локации, считаются производные функции Err по всем направлениям. Направление, в котором эта производная достигает максимума, принимается за азимут большой полуоси. Длина малой полуоси принимается равной

$$\text{Err}(\varphi, \lambda), \text{ а большой – } \text{Err}(\varphi, \lambda) \frac{\max_{\alpha} \frac{\partial \text{Err}}{\partial \alpha}}{\min_{\alpha} \frac{\partial \text{Err}}{\partial \alpha}}.$$

Представление результатов

По результатам детектирования и локации инфразвуковых событий программа PSDL создает бюллетени обнаруженных событий в формате HTML. Отдельные бюллетени могут быть сгенерированы для событий, обнаруженных отдельными группами (модули QACD), а также ассоциированные по нескольким группам (модуль ASIS). Бюллетени содержат информацию о событии (азимуты, координаты, ошибки локации и т.д.), а также карты, на которые нанесены события, азимуты приходов волн, эллипсы ошибок локации и т.д.

Кроме бюллетеней, система создает файлы с фрагментами волновых форм событий в формате CSS 3.0, к которым прикрепляется база данных с метаданными о событиях. Эта база позволяет выполнять поиск, генерировать таблицы и отчеты, рассчитывать статистические характеристики наборов событий с помощью программы интерактивной обработки сейсмических и инфразвуковых данных LOS [Асминг и др., 2021].

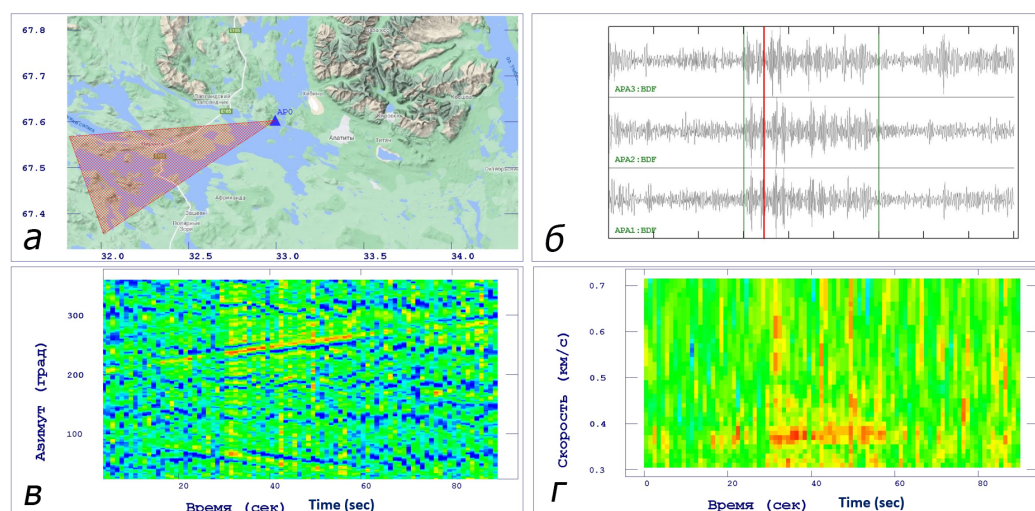


Рис. 3. Пример изображений, генерируемых при создании бюллетеня событий, зарегистрированных по одиночной группе AP0: а – карта, отображающая положение группы и сектор, покрывающий диапазон азимутов, с которых был принят сигнал; б – запись сигнала тремя каналами группы AP0, выделен фрагмент, соответствующий событию; в – кросскорреляционный график, отображающий изменение азимута сигнала со временем; г – кросскорреляционный график, отображающий изменение кажущейся скорости подхода волны со временем.

На рис. 3 показан пример бюллетеня, созданного для события, порожденного движущимся объектом (с большой вероятностью пролетом самолета). Азимут источника сигнала плавно менялся со временем.

Заключение

В работе подробно описаны алгоритмы обнаружения, ассоциации инфразвуковых сигналов, а также локации их источников по данным нескольких инфразвуковых групп. Описанные алгоритмы реализованы в программном комплексе PSDL. Опыт применения данного программного комплекса в задачах мониторинга инфразвуковых сигналов в Арктической зоне Российской Федерации (АЗРФ) показал высокую эффективность. В частности, программа PSDL применялась для обнаружения инфразвуковых сигналов, генерируемых движением снежной массы при сходе лавин в Хибинском горном массиве в Мурманской области. Специфическими особенностями таких сигналов являются длительность сигнала более 10 сек (до 40 сек в условиях Хибин) и изменчивость азимута на источник, в результате движения, генерирующего сигнал, фронта лавины по склону. Реализованный в программе алгоритм анализа протяженных сигналов, объединяющий соседние по времени фрагменты в общий сигнал, учитывает логику изменения азимута на источник и позволяет уверенно обнаруживать и классифицировать такого рода сигналы. Реализованный в программном комплексе алгоритм ассоциации инфразвуковых сигналов с результатами сейсмических наблюдений в случае совместной сейсмоинфразвуковой регистрации позволяет уточнять локализацию источников сигналов по данным одиночной сейсмоинфразвуковой группы. Также наличие или отсутствие ассоциируемого с инфразвуковым сигналом сейсмического может служить дополнительным критерием для классификации природы его источника.



Благодарности. Работа выполнена за счет гранта Российского научного фонда № 24-27-20007, <https://rscf.ru/project/24-27-20007/>.

Список литературы

- Асминг В. Э. и Асминг С. В. Потокосная система автоматического детектирования, локации и дискриминации PSDL // Современные методы обработки и интерпретации сейсмологических данных. Тезисы XVI Международной сейсмологической школы. — Обнинск : ФИЦ ЕГС РАН, 2022. — С. 17. — EDN: MNHNFK.
- Асминг В. Э., Баранов С. В., Виноградов А. Н. и др. Использование инфразвукового метода для мониторинга деструкции ледников в арктических условиях // Акустический журнал. — 2016. — Т. 62, № 5. — С. 582–591. — DOI: [10.7868/S0320791916040031](https://doi.org/10.7868/S0320791916040031).
- Асминг В. Э., Федоров А. В. и Прокудина А. В. Программа для интерактивной обработки сейсмических и инфразвуковых записей LOS // Российский сейсмологический журнал. — 2021. — Т. 3, № 1. — С. 27–40. — DOI: [10.35540/2686-7907.2021.1.02](https://doi.org/10.35540/2686-7907.2021.1.02).
- Виноградов Ю. А., Федоров А. В., Баранов С. В. и др. О выделении айсбергообразующих льдотрясений по сейсмоинфразвуковым данным // Лёд и снег. — 2021. — Т. 61, № 2. — С. 262–270. — DOI: [10.31857/S2076673421020087](https://doi.org/10.31857/S2076673421020087).
- Arrowsmith S. J., Hedlin M. A. H., Stump B., *et al.* Infrasonic Signals from Large Mining Explosions // Bulletin of the Seismological Society of America. — 2008. — Vol. 98, no. 2. — P. 768–777. — DOI: [10.1785/0120060241](https://doi.org/10.1785/0120060241).
- Cansi Y. and Le Pichon A. Infrasound Event Detection Using the Progressive Multi-Channel Correlation Algorithm // Handbook of Signal Processing in Acoustics. — Springer New York, 2008. — P. 1425–1435. — DOI: [10.1007/978-0-387-30441-0_77](https://doi.org/10.1007/978-0-387-30441-0_77).
- Ens T. A., Brown P. G., Edwards W. N., *et al.* Infrasound production by bolides: A global statistical study // Journal of Atmospheric and Solar-Terrestrial Physics. — 2012. — Vol. 80. — P. 208–229. — DOI: [10.1016/j.jastp.2012.01.018](https://doi.org/10.1016/j.jastp.2012.01.018).
- Gibbons S. J., Asming V., Eliasson L., *et al.* The European Arctic: A Laboratory for Seismoacoustic Studies // Seismological Research Letters. — 2015. — Vol. 86, no. 3. — P. 917–928. — DOI: [10.1785/0220140230](https://doi.org/10.1785/0220140230).
- Infrasound Monitoring for Atmospheric Studies: Challenges in Middle Atmosphere Dynamics and Societal Benefits / ed. by A. Le Pichon, E. Blanc and A. Hauchecorne. — Springer International Publishing, 2019. — DOI: [10.1007/978-3-319-75140-5](https://doi.org/10.1007/978-3-319-75140-5).
- Koch K. and Pilger Ch. Infrasound observations from the site of past underground nuclear explosions in North Korea // Geophysical Journal International. — 2018. — Vol. 216, no. 1. — P. 182–200. — DOI: [10.1093/gji/ggy381](https://doi.org/10.1093/gji/ggy381).
- Le Pichon A., Blanc E., Drob D., *et al.* Infrasound monitoring of volcanoes to probe high-altitude winds // Journal of Geophysical Research: Atmospheres. — 2005. — Vol. 110, no. D13. — DOI: [10.1029/2004JD005587](https://doi.org/10.1029/2004JD005587).

- Liszka L. *and* Waldemark K. High Resolution Observations of Infrasound Generated by the Supersonic Flights of Concorde // Journal of Low Frequency Noise, Vibration and Active Control. — 1995. — Vol. 14, no. 4. — P. 181–192. — DOI: [10.1177/026309239501400403](https://doi.org/10.1177/026309239501400403).
- Mutschlecner J. P. *and* Whitaker R. W. Infrasound from earthquakes // Journal of Geophysical Research: Atmospheres. — 2005. — Vol. 110, no. D1. — DOI: [10.1029/2004JD005067](https://doi.org/10.1029/2004JD005067).
- Ringdal F. *and* Kværna T. A multi-channel processing approach to real time network detection, phase association, and threshold monitoring // Bulletin of the Seismological Society of America. — 1989. — Vol. 79, no. 6. — P. 1927–1940. — DOI: [10.1785/BSSA0790061927](https://doi.org/10.1785/BSSA0790061927).

ALGORITHMS FOR AUTOMATIC DETECTION AND LOCATION OF INFRASOUND EVENTS IN THE PSDL SYSTEM

V. E. Asming¹  and A. V. Fedorov^{**1} 

¹Kola branch of Geophysical survey of Russia Academy of Sciences, Apatity, Russia

****Correspondence to:** Andrey Fedorov, Afedorov@krsc.ru

The paper presents a description of an automated system and the algorithms implemented in it for detection, association and location of low-frequency acoustic events based on infrasound array data. An algorithm for detecting infrasound signals by calculating the cross-correlation function between records of individual sensors in a array is described. The implemented algorithm is optimized for working with arrays consisting of a large number of sensors, which allows minimizing the computational load on the monitoring system in near-real time mode. A procedure for recognizing long-term signals with a source position that may change over time, such as moving vehicles or snow avalanches, is described. The paper also describes algorithms for associating infrasound signals recorded by different arrays, as well as locating a signal source based on data from several infrasound arrays. The system is capable of simultaneously analyzing seismic and infrasound monitoring data and detecting pairs of two types of signals associated with a common source. The algorithm for such an association is also given in the paper. The described system of automatic detection and location of infrasound signals can be used for monitoring dangerous natural and man-made processes and phenomena in a mode close to real time.

Keywords: infrasound signal, infrasound array, detection, location, cross-correlation.

Citation: Asming V. E., A. V. Fedorov (2024), Algorithms for Automatic Detection and Location of Infrasound Events in the PSDL System, *Russian Journal of Earth Sciences*, 24, ES6002, <https://doi.org/10.2205/2024ES000944>, EDN: ZVUUJP

Received: 4 October 2024
Accepted: 23 October 2024
Published: 30 December 2024



© 2024. The Authors.

References

- Arrowsmith S. J., Hedlin M. A. H., Stump B., *et al.* Infrasonic Signals from Large Mining Explosions // Bulletin of the Seismological Society of America. — 2008. — Vol. 98, no. 2. — P. 768–777. — DOI: [10.1785/0120060241](https://doi.org/10.1785/0120060241).
- Asming V. E. and Asming S. V. The stream system of automatic detection, location and discrimination PSDL // Modern methods of processing and interpretation of seismological data. Abstracts of the XVI International Seismological Workshop. — Obninsk : GS RAS, 2022. — P. 17. — EDN: MNHNFK.
- Asming V. E., Baranov S. V., Vinogradov A. N., *et al.* Using an infrasonic method to monitor the destruction of glaciers in Arctic conditions // Acoustical Physics. — 2016. — Vol. 62, no. 5. — P. 583–592. — DOI: [10.1134/S1063771016040035](https://doi.org/10.1134/S1063771016040035).
- Asming V. E., Fedorov A. and Prokudina A. The program LOS for interactive seismic and infrasonic data processing // Russian Journal of Seismology. — 2021. — Vol. 3, no. 1. — P. 27–40. — DOI: [10.35540/2686-7907.2021.1.02](https://doi.org/10.35540/2686-7907.2021.1.02).
- Cansi Y. and Le Pichon A. Infrasound Event Detection Using the Progressive Multi-Channel Correlation Algorithm // Handbook of Signal Processing in Acoustics. — Springer New York, 2008. — P. 1425–1435. — DOI: [10.1007/978-0-387-30441-0_77](https://doi.org/10.1007/978-0-387-30441-0_77).
- Ens T. A., Brown P. G., Edwards W. N., *et al.* Infrasound production by bolides: A global statistical study // Journal of Atmospheric and Solar-Terrestrial Physics. — 2012. — Vol. 80. — P. 208–229. — DOI: [10.1016/j.jastp.2012.01.018](https://doi.org/10.1016/j.jastp.2012.01.018).
- Gibbons S. J., Asming V., Eliasson L., *et al.* The European Arctic: A Laboratory for Seismoacoustic Studies // Seismological Research Letters. — 2015. — Vol. 86, no. 3. — P. 917–928. — DOI: [10.1785/0220140230](https://doi.org/10.1785/0220140230).
- Infrasound Monitoring for Atmospheric Studies: Challenges in Middle Atmosphere Dynamics and Societal Benefits / ed. by A. Le Pichon, E. Blanc and A. Hauchecorne. — Springer International Publishing, 2019. — DOI: [10.1007/978-3-319-75140-5](https://doi.org/10.1007/978-3-319-75140-5).

- Koch K. *and* Pilger Ch. Infrasound observations from the site of past underground nuclear explosions in North Korea // Geophysical Journal International. — 2018. — Vol. 216, no. 1. — P. 182–200. — DOI: [10.1093/gji/ggy381](https://doi.org/10.1093/gji/ggy381).
- Le Pichon A., Blanc E., Drob D., *et al.* Infrasound monitoring of volcanoes to probe high-altitude winds // Journal of Geophysical Research: Atmospheres. — 2005. — Vol. 110, no. D13. — DOI: [10.1029/2004JD005587](https://doi.org/10.1029/2004JD005587).
- Liszka L. *and* Waldemark K. High Resolution Observations of Infrasound Generated by the Supersonic Flights of Concorde // Journal of Low Frequency Noise, Vibration and Active Control. — 1995. — Vol. 14, no. 4. — P. 181–192. — DOI: [10.1177/026309239501400403](https://doi.org/10.1177/026309239501400403).
- Mutschlecner J. P. *and* Whitaker R. W. Infrasound from earthquakes // Journal of Geophysical Research: Atmospheres. — 2005. — Vol. 110, no. D1. — DOI: [10.1029/2004JD005067](https://doi.org/10.1029/2004JD005067).
- Ringdal F. *and* Kväerna T. A multi-channel processing approach to real time network detection, phase association, and threshold monitoring // Bulletin of the Seismological Society of America. — 1989. — Vol. 79, no. 6. — P. 1927–1940. — DOI: [10.1785/BSSA0790061927](https://doi.org/10.1785/BSSA0790061927).
- Vinogradov Yu. A., Fedorov A. V., Baranov S. V., *et al.* Identification of iceberg-forming ice quakes from seismic and infrasound data // Ice and Snow. — 2021. — Vol. 61, no. 2. — P. 262–270. — DOI: [10.31857/S2076673421020087](https://doi.org/10.31857/S2076673421020087).

OPTIMAL INTERPOLATION METHOD FOR GENERATING A DIGITAL BATHYMETRIC MODEL FOR SHALLOW WATERS: A CASE STUDY OVER MAURITIUS COAST

S. Satpute¹ , S. Roy² , O. S. Gatage³ , V. B. Kolase³ , S. K. Singh¹ , and G. Dandabathula^{*,2} 

¹Centre for Climate Change and Water Research, Suresh Gyan Vihar University, Jaipur, India

²Regional Remote Sensing Centre – West, NRSC/ISRO, Jodhpur, India

³Department of Geography, Bharathidasan University, Tiruchirappalli, India

* **Correspondence to:** Giribabu Dandabathula, dgb.isro@gmail.com

Abstract: Bathymetry unveils the underwater topography of oceans, seas, rivers, and lakes. It is a fundamental data resource for various applications, like physical oceanography, marine geology, geophysics, and marine resources. The techniques to compute the seafloor depths are ship-borne echo sensors, empirical models of satellite-derived bathymetry, and aerial-space-borne laser altimetry. The digital bathymetric surfaces are generally generated from a distributed seafloor depths. Once these depth points are collected, the next step to generate a continuous surface is to select and implement interpolation. Numerous interpolation methods have advantages and disadvantages that can hamper the accuracy of the surface, which generally depends on the shape of the extent, distribution, and point density. To date, there is no recommended interpolation method when the study extent is circular with well-distributed points – the core objective of this research is oriented towards this. An attempt was made to generate a digital bathymetric surface for the Mauritius coast with ~ 1.2 million depth points accrued from the NASA ICESat-2 geolocated photons and sounding depths from the marine charts. These points were used as input to interpolation methods like Inverse Distance Weighted, Natural Neighbour, and various forms of Ordinary Kriging. Our findings show that all the methods have generated visually similar surfaces, but the Inverse Distance Weighted interpolation has given the output with less quantified uncertainty.

Keywords: Bathymetry, Interpolation, LiDAR, Inverse Distance Weighted, Natural Neighbour, Kriging.

Citation: Satpute, S., S. Roy, O. S. Gatage, V. B. Kolase, S. K. Singh, and G. Dandabathula (2024), Optimal Interpolation Method for Generating a Digital Bathymetric Model for Shallow Waters: A Case Study over Mauritius Coast, *Russian Journal of Earth Sciences*, 24, ES6003, EDN: PGHFFW, <https://doi.org/10.2205/2024es000937>

Introduction

Bathymetry is the study of mapping the water depth in oceans, seas, rivers, and lakes, and it plays an essential role in understanding and portraying the marine environment. Similar to topographic mapping on land, bathymetric surveys create seafloor depth maps, revealing its seabed structure [Vogt and Tucholke, 1986]. This information is essential for various applications, including marine navigation, ocean engineering, seafloor morphology, tectonic studies, and deep-sea mineral exploration [Dysart, 1996; Smith and Sandwell, 1997; Vogt and Tucholke, 1986; Wöflf et al., 2019]. Bathymetric data potentially aids in investigating coastal dynamics, sediment transportation, changes in seabed morphology, sea level changes, and the impact of global climate patterns, and also helps avoid underwater hazards during navigation [Smith and Sandwell, 1997; Wöflf et al., 2019].

Technological advancements have dramatically improved our ability to map the ocean floor. Ship-borne echo-sounding techniques are classical but still are valid methods for collecting bathymetric data [Smith and Sandwell, 1997]. The echo-sounding techniques are generally either single-beam or multi-beam; if single-beam echo sensors are employed, the

RESEARCH ARTICLE

Received: 4 July 2024

Accepted: 30 September 2024

Published: 30 December 2024



Copyright: © 2024. The Authors. This article is an open access article distributed under the terms and conditions of the Creative Commons Attribution (CC BY) license (<https://creativecommons.org/licenses/by/4.0/>).

result is less coverage, whereas the multi-beam echo-sounding sensors can provide better coverage and more detailed underwater topography [Ashphaq et al., 2021; Pratomo et al., 2023].

With the advent of the earth-observation systems, satellite-derived bathymetry methods that came into existence use multispectral imagery to map the depths of the shallow waters. However, for these methods are empirical and need real-time seed data as a parameter to initiate the model [Wölfl et al., 2019].

On the other hand, LiDAR-based bathymetry has several advantages over ship-borne sounding technology. These advantages include high precision, high point cloud density, high accuracy, and low cost [Ashphaq et al., 2021; Hildale and Raff, 2007; Li et al., 2023]. However, the limitation with the LiDAR-based altimeter is that we can measure to limited depths [Ashphaq et al., 2021; Li et al., 2023]. Ice, Cloud and land Elevation Satellite-2 (ICESat-2), launched by the National Aeronautics and Space Administration (NASA), has been operational since September 2018. ICESat-2 hosts a solo sensor, Advanced Topographic Laser Altimeter System (ATLAS), credited as a revolutionary space-borne altimeter due to its caliber with a highly sensitive photon-counting system [Markus et al., 2017]. The ATLAS sensor onboard the ICESat-2 utilizes a 532 nm wavelength (green) laser, operating at a pulse repetition frequency of 10 kHz, and encounters a diffractive optical element to release six beams. From each of the six beams, geolocated photon data having a spatial resolution of 70 cm can provide surface elevation information [Neumann et al., 2019]. Primarily, the applications of the ICESat-2 data were oriented for the cryosphere. However, the scientific fraternity has successfully used geolocated photon data for various applications related to land/terrain, forest/canopy, and inland water bodies [Brown et al., 2023].

Parrish et al. [2019] evaluated the application validity of ICESat-2-based geolocated photon data towards bathymetric studies; their studies proved that seafloor detection in water depths of up to ~ 40 m is possible during clear water conditions [Parrish et al., 2019]. With this clue, numerous studies have shown the potential of using ICESat-2 geolocated photons for bathymetric studies [Giribabu et al., 2023, 2024; Guo et al., 2022; Rannadal et al., 2021; Xie et al., 2021].

In our study, we generated a digital bathymetric model for the shallow waters of the coastal area for an island using the depth information from ICESat-2 geolocated photon data and the sounding depth values from the available hydrographic charts. The points representing the depth values need interpolation to generate a surface representing the seafloor topography. Interpolation is a mathematical process to predict unknown values using the surrounding measured values [Burrough et al., 2015]. Interpolation techniques are generally classified into deterministic and geostatistical [Childs, 2004]. Deterministic interpolation techniques create surfaces based on measured points (with known values) using mathematical formulas; methods such as Inverse Distance Weight (IDW) and Natural Neighbor (NN) fall in the deterministic category. In contrast, geostatistical interpolation techniques, such as various forms of Kriging, are based on statistics and are used for predicting surface values but include some measure of the uncertainty [Childs, 2004].

However, many researchers are still investigating the best choice in selecting the optimal interpolation technique while generating a bathymetric surface for the shallow water regions, and the question remains a gap area [Li et al., 2023]. The motivation of this study is to determine the best optimal interpolation method given a set of points representing depth values in a shallow water region. Moreover, our research has emphasized an Island that is typically circular. Globally, many of the Islands are circular; thus, the anticipated results from this study should provide a clue for selecting the best interpolation method while generating a bathymetric surface.

Towards reaching the objectives of this research, after accruing the points data containing the depth values of the seafloor pertaining to the study area, various interpolation methods were used to generate the surfaces. Currently, in Geographic Information System (GIS) software like ESRI ArcGIS AND QGIS, nearly 40 interpolation methods are available.

Certain interpolation methods are optimized for surface generation, some for weather forecasting, and some for estimating the missing values. Research done by [Henrico \[2021\]](#) suggested that interpolation methods like IDW, NN, and various Ordinary Kriging (OK) forms are optimized for surface generation. These methods were given preference in our research to generate surfaces. These surfaces were validated by referring to the checkpoints and computing an error quantifier based on a statistical formula like Root Mean Square Error (RMSE). The RMSE computed for each surface generated from the individual interpolation method has been compared to assess the best interpolation method.

Material and methods

Study Area. The study area chosen for this research is Mauritius, which extends over 2.3 million km² (including its sea-zone). It is an island country in the Indian Ocean, about 2000 km off the south-eastern coast of East Africa and east of Madagascar. Isles like Rodrigues, Agaléga, and St. Brandon (Cargados Carajos shoals) are also part of Mauritius. The mainland Mauritius is at latitude 20°10'S and longitude 57°30'E, has a surface area of 1859 km² and a nearly 200 km long coastline. The region is mainly composed of different shoreline types, and chiefly, they are categorized as sandy, rocky, muddy, mixed, calcareous lime stones, and cliffs of coastal geological features [[Doorga et al., 2021](#)]. [Figure 1](#) shows the extent of Mauritius as viewed in high-resolution satellite imagery. The Island is of volcanic origin, and its formation involves the three primary dome building processes that created the structural shape of the high uplands in the central region and lowlands in the coastal region [[Doorga et al., 2021](#)]. According to recent estimates, Mauritius Island has a population of 1.27 million, with the main attraction being its coastal beaches for tourists. Tourism is the third pillar of economic growth after Mauritius's manufacturing and agriculture sectors [[Duvat et al., 2020](#)]. Mauritius's central Plateau is between 300 to 600 meters from mean sea level.

In the context of global climate change, Mauritius is highly vulnerable to sea-level rise as recent studies indicate a rise of 5.6 mm/year on average over the past 30 years – this is 2 to 3 times faster than the 20th century global mean sea level due to climate change [[Devi and Xi, 2020](#)]. This, in turn, will impact the increase in coastal erosion [[Becker et al., 2019](#)]. Thus, high-resolution digital bathymetric data, like the one generated in this research, is beneficial for studying climate change's impact on Mauritius's coastal line. In this research, we have generated a digital bathymetric model for a buffer region of 3 km from the coastline of Mauritius mainland (shown in [Figure 1b](#))

Datasets. [Table 1](#) shows the datasets used to generate a digital bathymetric model for Mauritius Island. Primarily, the datasets include NASA ICESat-2 geolocated photons, navigational charts, and elevation values from a bare-earth digital elevation model (DEM). The details of these datasets are mentioned in the subsequent sections.

ICESat-2, a polar-orbiting satellite from an average altitude of 496 km, will acquire the data during day and night for the globe in 1387 predefined ground reference tracks with a temporal resolution of 91 days [[Markus et al., 2017](#)]. Over the extent of Mauritius mainland and its shallow waters coasts, eight ICESat-2 reference ground tracks are available (listed in [Table 1](#) and illustrated in [Figure 2](#)). From these eight reference ground tracks, one hundred sixty acquisitions of ICESat-2 data between October 2018 and October 2023 are available for the study area. In general, bathymetric studies should use only those acquisitions from nighttime because daytime acquisitions can include substantial noise arising from solar background radiations [[Giribabu et al., 2023](#)]. Similarly, ICESat-2 acquisitions may be impacted due to the presence of clouds, and photons may not be able to reach the Earth's surface [[Hawker and Neal, 2021](#)]. Thus, 79 acquisitions were available for retrieving the seafloor depth information by omitting daytime acquisitions and those of missed data due to the presence of clouds.

The sciences teams of ICESat-2 will process and distribute the photon data by categorizing it into various levels, out of which Level-2A data product, namely, ATL03, is

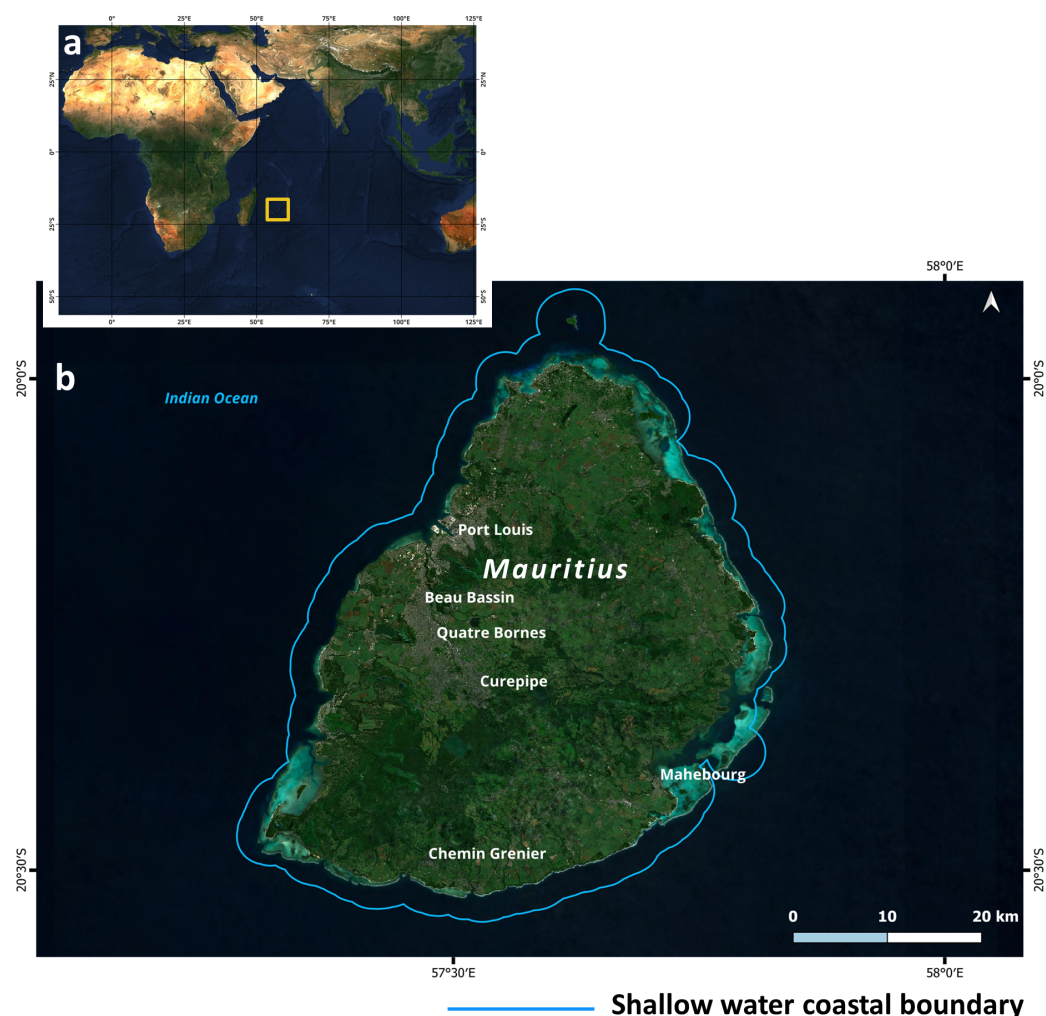


Figure 1. Location map of Mauritius mainland. (a) The location of the Mauritius mainland in the Indian Ocean is highlighted with a yellow box. (b) Mauritius mainland, which constitutes the study area of this research.

a principal data source that contains geolocated photons with attributes like latitude, longitude, and elevation for each successful photon event [Neumann *et al.*, 2019]. In our research, we have used ATL03. From the available 79 acquisitions over the study area, 474 beams are qualified for seafloor depth retrieval (shown in Figure 2). Retrieval of the seafloor from these beams is discussed in the methodology section.

The other source of seafloor depth is the navigational chart obtained from the National Hydrographic Office of the study area [INHO, 2024]. The sounding depths from chart number 2557 at a scale of 1:125,000 were manually digitized in GIS software. Elevation values for the mainland of the study area were retrieved from a bare-earth digital elevation model called Forest and Building removed Copernicus DEM (FABDEM); however, the role of the elevation values from the FABDEM is to fill the gap due to the Mauritius mainland during the visualization of the output and does not have any role in the generation of bathymetric model [Hawker and Neal, 2021].

Methodology. In general, during the ICESat-2's data acquisition process, photons emanating from the ATLAS sensor will return from various features of the Earth's surface. 2D profiles drawn from the along-track geolocated photons will enable us to visualize various features of the Earth's surface. As shown in Figure 3, for a subset of geolocated photons

Table 1. Details of the datasets used in generating a digital bathymetric model for the shallow waters of Mauritius coasts

Dataset	Source	Details
NASA ICESat-2 ATL03	OpenAltimetry application available at [National Snow and Ice Data Center, 2023]	Ground Track: 1217, 661, 272, 1103, 714, 158, 1156, and 600. Duration of Acquisitions: October 2018 to October 2023 Preferred acquisition period: mostly Night time Preferred beam type: Mostly strong beam Total number of Refracted photons from the seafloor: 1.2 million
Sounding depths from navigational charts	Information available at National Hydrographic Office’s web portal available at [INHO, 2024]	Chart Name: Mauritius Chart Scale: 125000 Year of Publication: 2019 Chart No.: 2557
Forest and Building removed Copernicus DEM (FABDEM)	Web portal available at [Hawker and Neal, 2021]	Elevation values pertaining to the Mauritius mainland

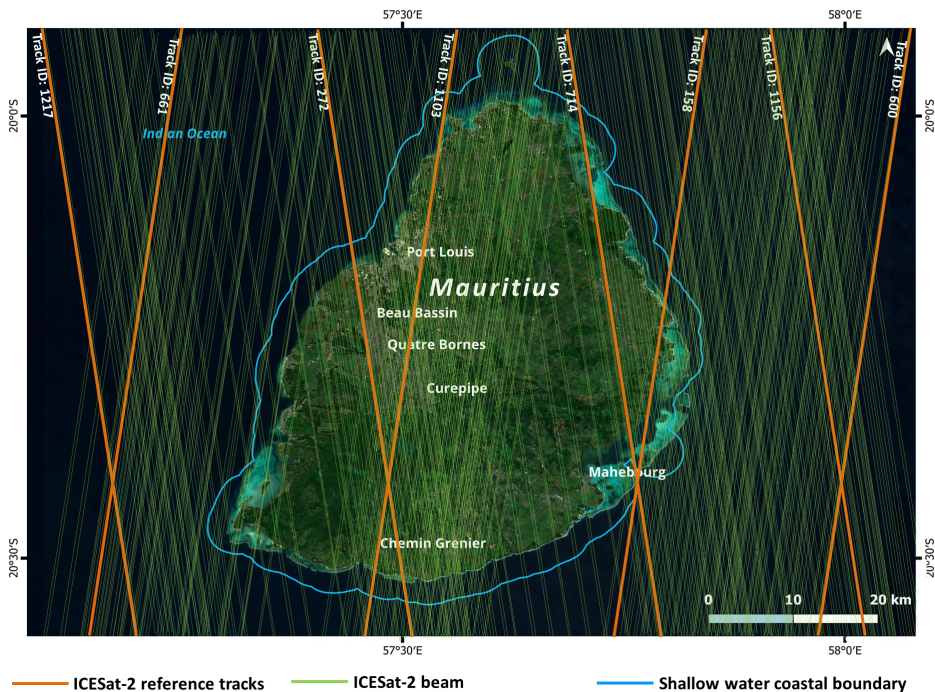


Figure 2. ICESat-2’s ground reference tracks and available beams over Mauritius mainland and the surrounding shallow waters.

acquired over the region, namely, Centre de Flacq, which is adjacent to the coastal area, the profile shows the photons returning from the canopy, land, water surface, water column, and seafloor. In this research, all the ATL03 beams from the ICESat-2 were processed in ESRI ArcGIS software [ESRI, 2024a]; specifically, the graph wizard in the table editor of the ESRI ArcGIS facilitates provision for classification of the points falling in various classes (refer to Figure 3c). As this research is oriented to generate a bathymetric surface, the

photons returning from the canopy, land, and the water surface have been discarded – only those photons returning from the seafloor are considered for further steps.

[Parrish et al. \[2019\]](#), [Guo et al. \[2022\]](#), and [Giribabu et al. \[2024\]](#) suggested that before considering the depth information from the geolocated photons to generate the bathymetric surface, a refraction correction is a must; this is because there will be a change in the speed of light that occurs at the air-water interface due to different refractive indices of air and sea-water. Hence, the default depth information from the geolocated photons is apparent. This apparent depth can be corrected using Snell's Law as suggested by [\[Giribabu et al., 2024; Guo et al., 2022; Parrish et al., 2019\]](#). Similarly, the default vertical datum of the elevation/depth retrieved from the ATL03 data product is in the WGS84 ellipsoid system, whereas the seafloor depth in the bathymetric charts is represented in the orthometric system. In this research, the conversion of the depth information from the ellipsoidal to the orthometric system was done using the geoid height calculator available at the UNAVCO web portal by preferring the EGM2008 geoid model [\[GAGE Facility, 2021\]](#). A total of 1.2 million depth values from the geolocated photons were accrued in this research for the shallow waters surrounding Mauritius.

Additionally, sounding depths were digitized from the navigational charts available at the National Hydrographic Office (NHO). A total of 22700 sounding depths were accrued for the shallow waters surrounding the coast of Mauritius.

Twenty-five depth points from the ICESat-2 geolocated photons were reserved as checkpoints to evaluate the output's accuracy (discussed in the subsequent sections). All the points representing the depths in the study area are illustrated in [Figure 4](#). The methodology adopted for generating the surface from these points was incorporated in [Figure 5](#).

An interpolation method is used to generate a continuous surface from the depth points, during which it will estimate a value in the area of unknown values from a distribution of known depth points to generate a continuous surface. In our research, we used the interpolation methods available in ESRI ArcGIS software [\[ESRI, 2024a\]](#); the methods are shown in [Figure 5](#).

The IDW is considered a non-statistical interpolation method and does not account for the spatial distribution of points but instead predicts unknown values based on the proximity of known values [\[Li and Heap, 2014; Wang et al., 2014\]](#). By giving preference to the nearest neighboring points, IDW assigns more influence to data points closer to the unknown points. These nearby known points carry greater weight in the calculation, and the unknown values are estimated as a weighted average of these close neighbors. It is proven that IDW will generate a smooth interpolated surface and considers dimension parameters, the number of sampling points, and the power parameter, which controls the influence of neighboring points on the interpolated values [\[de Souza et al., 2003\]](#). However, favoring the closest neighboring points results in weighted averages similar for all points in proximity, which can be a disadvantage using this method.

Similar to the IDW, NN interpolation method estimates unknown values using nearby known data points, but the difference is in computation approach. NN interpolation finds the closest subset of input samples to a query point and applies weights to them based on proportionate areas to interpolate a value; the method is also referred as Sibson or area-stealing interpolation [\[Sibson, 1981\]](#). NN interpolation methods is having advantage that it works equally well with irregularly distributed points and also, will not produce errors like sudden peaks or sinks [\[Watson, 1992\]](#).

Kriging a geostatistical interpolation method uses the spatial correlation between sampled points to interpolate the values in the spatial field: the interpolation is based on the spatial arrangement of the empirical observations rather than on a presumed spatial distribution model. Kriging also generates estimates of the uncertainty surrounding each interpolated value [\[Collet et al., 2018; Luo et al., 2007\]](#). Generally, during the process of estimating the optimal interpolation weights, Kriging method takes into account both distances and directions to establish the spatial relationships within the data. Ordinary Kriging is the most common form of interpolation method that uses to model the empirical semi variogram like spherical, circular, exponential, Gaussian, and linear.

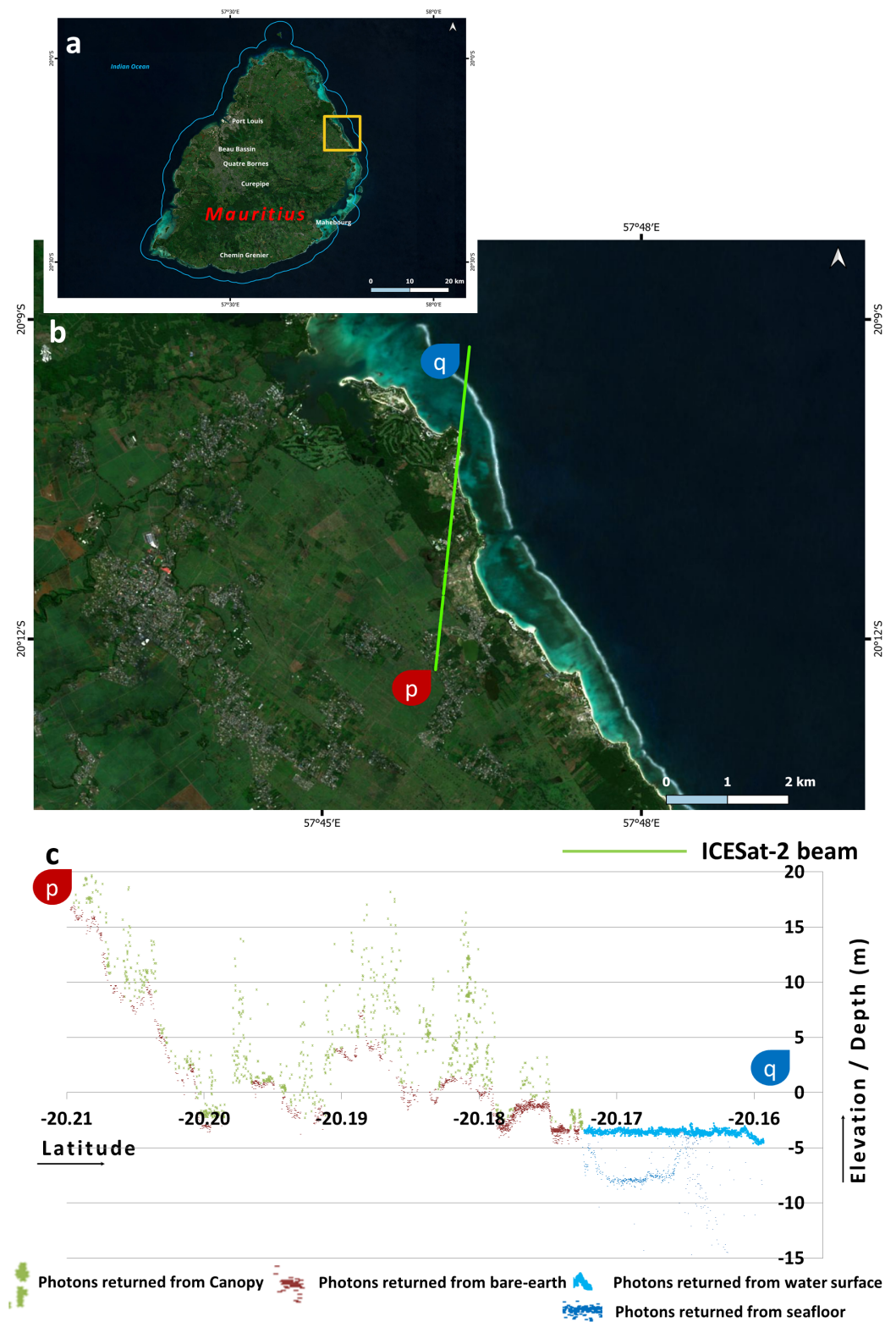


Figure 3. Return photons of ICESat-2 from various features of Earth's surface. (b) Location map of Mauritius mainland. (a) A subset of ICESat-2 beam acquired over land and shallow waters. (c) 2D profiles generated from along-track ICESat-2 geolocated photons. Notably, the profiles show the photons returned from canopy, land, water surface, water column, and seafloor.

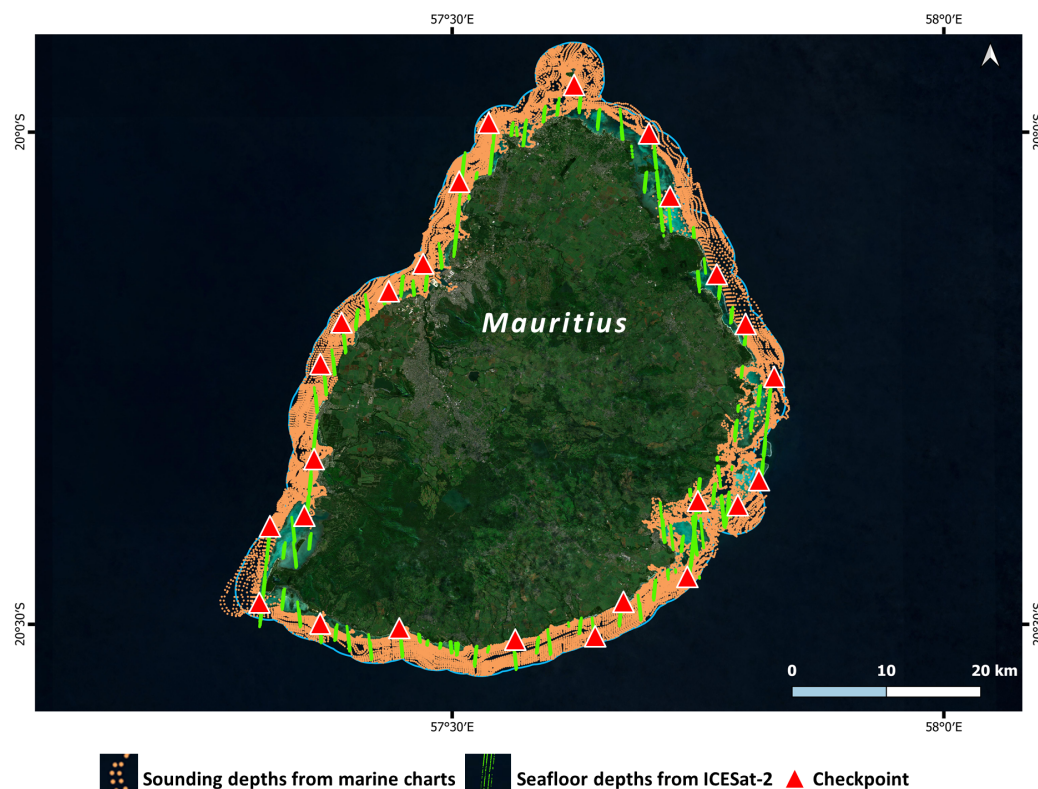


Figure 4. Map showing the distribution of points representing the seafloor depths used to generate a digital bathymetric model for the shallow waters of the Mauritius coast. Nearly 1.2 million points were accrued towards creating the depth database primarily acquired from the ICESat-2 geolocated photons returned from the seafloor and 22,700 sounding depths from marine charts. A few points were reserved as checkpoints for technical validation of the output.

Spatial autocorrelation in the spherical Kriging model increases linearly for short distances and then flattens after a certain threshold. This method is commonly used due to its moderate complexity and effectiveness for many spatial data types. Kriging interpolation with circular semi-variograms assumes that spatial correlation decreases in a circular pattern. This makes it suitable for data with a limited spatial extent and a rapid decline in correlation with distance. The spherical and circular Krigings methods work well when the area of study is relatively small, and the influence of known points diminishes quickly (very short distance) as you move away from them [ESRI, 2024b; Mesić Kiš, 2016].

Exponential Kriging assumes that spatial correlation decreases exponentially with distance. This method is ideal for data where the correlation declines rapidly over short distances, reflecting a more abrupt change in values as you move away from known points [Mesić Kiš, 2016]. The Gaussian Kriging model's spatial correlation decreases rapidly near the origin and more slowly over longer distances. This approach is well-suited for data with strong short-range correlation and a gradual decline over longer distances, providing a smooth transition in the interpolated values [ESRI, 2024b]. Linear Kriging assumes a steady, linear decrease in spatial correlation without a clear range limit. This method is appropriate for data where the correlation consistently declines over distance, without a point where the influence of known points becomes negligible.

Each Kriging method can be chosen for its suitability to different spatial patterns and data characteristics, ensuring accurate and reliable interpolations. By using the strengths of various kriging techniques, the research aims to understand the spatial relationships within the study area thoroughly.

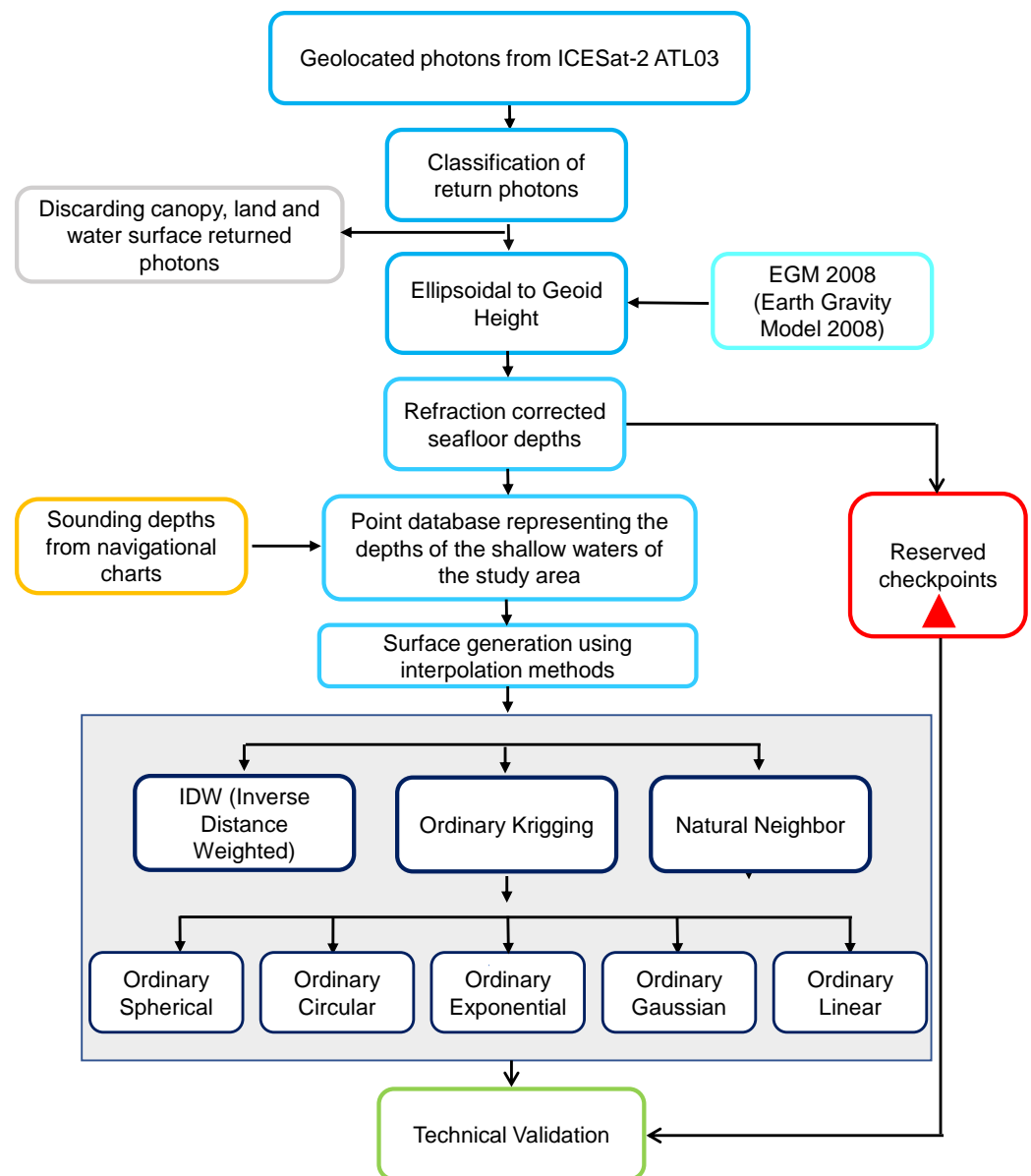


Figure 5. Schematic representation of the methodology used to generate a bathymetric surface from ICESat-2 geolocated photons and sounding depths from the marine charts. Bathymetric surfaces have been generated using various interpolation methods. The reserved checkpoints were not used in the interpolation methods and used for technical validation as reference points.

After generating the digital bathymetric surface using various interpolation methods, a technical validation was performed to assess the accuracy of each interpolation method. Twenty-five checkpoints that were well-distributed in the study area were used to validate the individual surface; during this process, the RMSE was calculated by comparing the depth values of each surface to that of the checkpoint. RMSE, provides a quantitative measure of the differences between the interpolated values and the observed values. This comparison allows evaluating the performance of each interpolation method. The formula for the RMSE is given in (1).

$$\Delta H = (\text{Depth})_{\text{bathymetric_surface}} - (\text{Depth})_{\text{checkpoint}},$$

$$\text{RMSE} = \sqrt{\frac{\sum \Delta H^2}{n}}, \quad (1)$$

where $(\text{Depth})_{\text{bathymetric_surface}}$ is the set of depth values obtained from the interpolated surface and $(\text{Depth})_{\text{checkpoint}}$ are the set of depth values of the reserved checkpoints of ICESat-2, $n = 25$ is the number of observations.

Results

Seven surfaces representing the digital bathymetric models were generated for the study area using IDW, NN, and five methods of Kriging interpolations. Figures 6 and 7 show the 3D perspective view and 2D maps of the digital bathymetric models generated from the IDW and other interpolation methods, respectively. Table 2 shows the RMSEs obtained for each surface, referring to the depth values of the checkpoints.

Errors in digital surfaces are usually classified as either sinks or peaks/spikes. A sink is an area surrounded by higher elevation values and referred to as a depression or pit. Generally, sinks appearing suddenly on the surfaces are treated as imperfections in the digital surfaces. Likewise, a peak/spike is an area surrounded by cells of lower value. The more sinks and peaks/spikes appear in the modelled surfaces implies severe errors. Errors such as these can be visualized by performing quality assessment through visual analysis.

For our research towards the technical validation of the outputs, in the first stage, qualitative analysis was done using the visual analysis of the surfaces obtained from all the interpolation methods; the result from the qualitative analysis shows that all the digital surfaces are without any sinks and spikes (refer to Figures 6 and 7). Earlier, Amoroso et al. investigated the influence of point density on the accuracy of bathymetric surface generation and concluded that more dense and well-distributed points could ensure better surface generation [Amoroso et al., 2023]; probably, this may be the reason that in our case, the surfaces generated by various interpolation methods have yielded less visible errors. However, quantifiers like RMSE can inform the invisible uncertainty in the digital surface. The resultant RMSEs, as computed based on (1), were as summarised in Table 2 for quantifying the depth accuracy of individual surfaces. From Table 2, the IDW interpolation method has yielded significantly lower RMSEs when compared with the other interpolation methods. The minimum and maximum differences in the depth estimations in the surface generated by IDW are 0.28 m and 0.96 m, respectively. Next to the IDW interpolation, NN is a better estimation of depths (refer to Table 2). Notably, the RMSEs obtained from the surfaces of various forms of Kriging methods have yielded nearly 1 m or greater of error. Thus, the depth estimation given by the IDW, which has a minimum uncertainty of ~ 0.68 m, stands to be a better performer.

Table 2. RMSEs obtained for bathymetric surface that were generated from various interpolations methods

Interpolation method	RMSE (m) $n = 25$	Minimum (ΔH)	Maximum (ΔH)
IDW	0.68	0.28	0.96
NN	0.89	0.45	1.04
OK – Spherical	0.98	0.68	1.33
OK – Circular	1.23	0.82	1.32
OK – Exponential	1.45	0.83	1.34
OK – Gaussian	1.46	0.72	1.65
OK – Linear	1.12	0.69	1.55

Discussion

This study aimed to evaluate the accuracy of three interpolation methods – IDW, NN, and various parametric methods of Kriging in predicting the bathymetry of the shallow waters of the Mauritius coastal region. The research ensured a comprehensive distribution of sample points across the entire study area by utilizing depth points retrieved from the

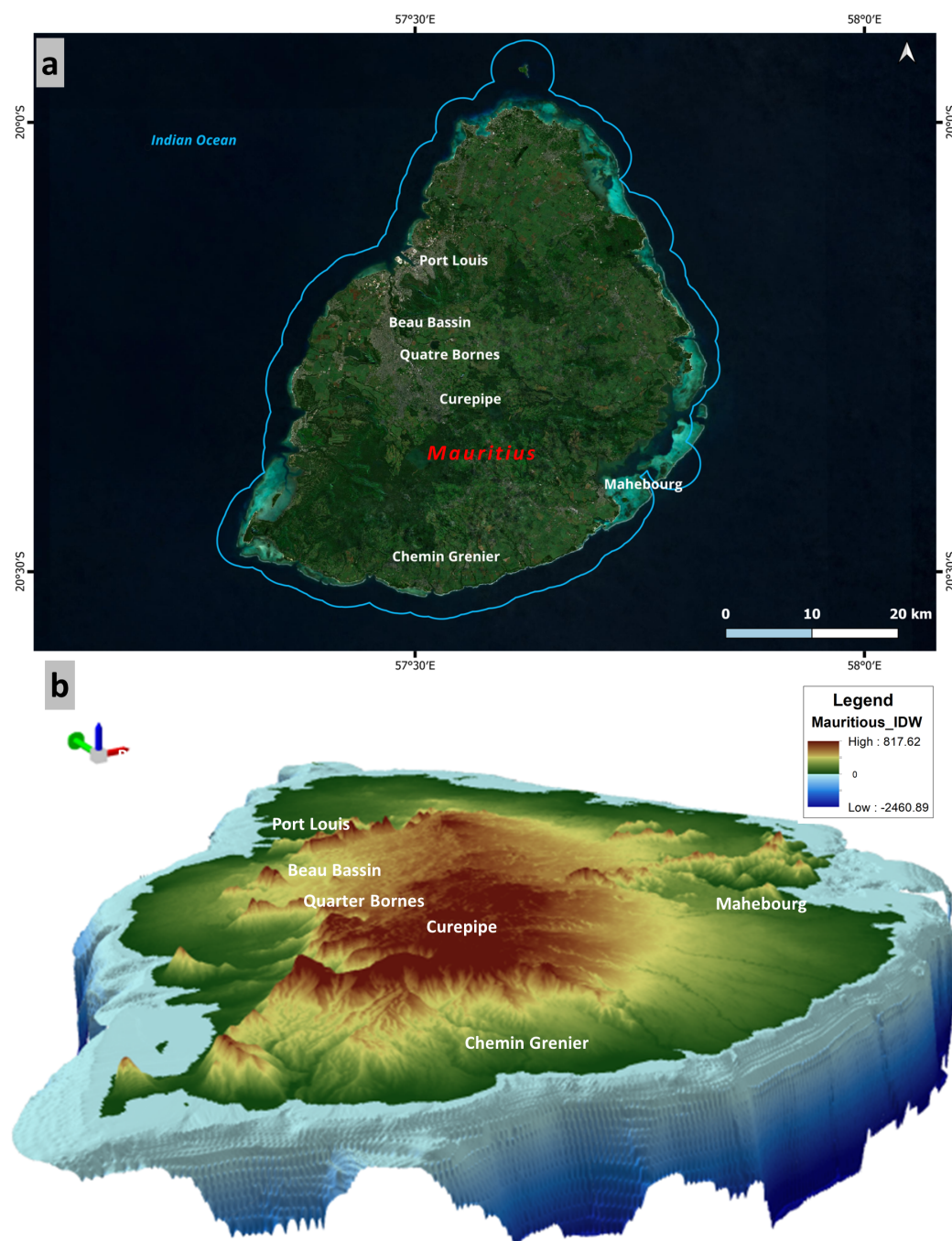


Figure 6. 3D perspective generated with a 10 m digital bathymetric model generated using ICESat-2 photons and sounding depths from the navigation charts for the extent of Mauritius. (a) Extent showing Mauritius mainland and the surrounding coast in a high-resolution satellite imagery. (b) Perspective view for the extent of Mauritius and its surroundings.

water-penetrated geolocated photon data of ICESat-2 and the accurate sounding points digitized from the navigation charts.

Earlier, Ferreira et al. conducted a similar experiment at the main damming of the Sao Bartolomeu stream located at the Federal University of Viçosa in Brazil. In their experiment, the distribution of the points is linearly spread but interleaved, and the extent of the study area is nearly rectangular. Their experiment proved that the OK method produced superior

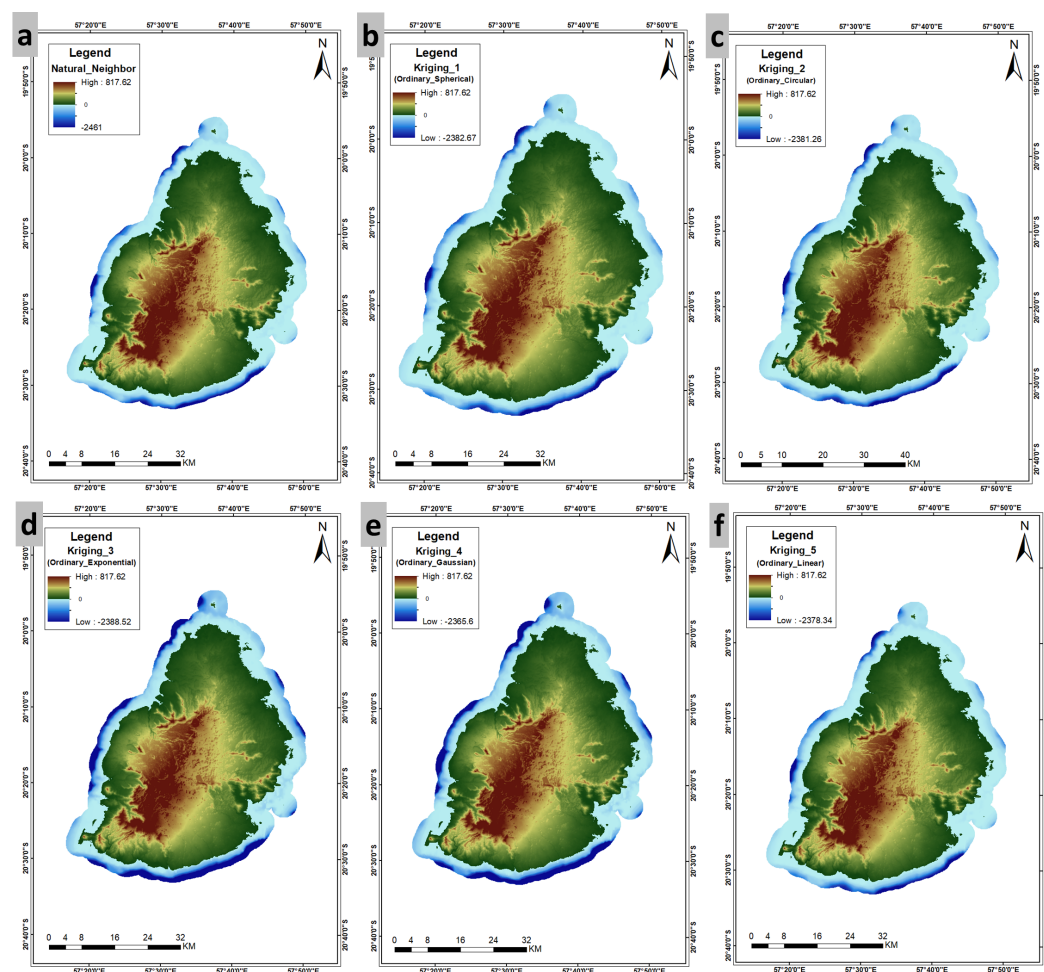


Figure 7. 2D maps of the digital bathymetric model generated using ICESat-2 photons and sounding depths from the navigation charts for the extent of Mauritius. (a, b, c, d, e, & f) Bathymetric models generated from NN, OK (spherical, circular, exponential, Gaussian, and linear), respectively.

output to IDW [Ferreira et al., 2017]. Whereas, the experiment conducted by Henrico et al. [Henrico, 2021] over the extent of Saldanha Bay, which is nearly irregular in shape and having well-distributed points, has proven that IDW has given superior quality of surface prediction in comparison with the OK method.

The shape of the study extent in our research is nearly circular with a well-distributed depth points. The surfaces generated from various interpolation methods when performed visual comparisons, revealed clear similarities in how these methods estimate and generated continues bathymetric surface. However, quantitative assessment resulted in informing that the IDW method has unleashed a surface with fewer uncertainties. Consequently, IDW was identified as the most suitable interpolation method for predicting the bathymetry of the Mauritius coast. Compared to NN and OK methods, IDW produced better accuracy predictions. The findings illustrate the effectiveness of IDW in bathymetric mapping and highlight its potential as the preferred method for future studies in similar coastal environments.

Conclusion

This study aimed to identify the optimal interpolation method for generating a high-resolution digital bathymetric model for a circular-shaped extent with well-distributed points. Towards this, the coastal area of Mauritius Island containing shallow waters was chosen as a study area. Approximately 1.2 million depth points from ICESat-2 photons and

navigation charts were used as input to the interpolation methods. IDW, NN, and various Kriging interpolation methods were used to generate bathymetric surfaces. Technical validation was performed through qualitative and quantitative assessments. Visual analytics shows similarities in all the output surfaces. In contrast, the quantitative assessment has shown that the IDW method is the optimal technique to generate a digital surface with less uncertainty.

The study highlights the importance of selecting appropriate interpolation methods for bathymetric modeling. It demonstrates the superiority of IDW for generating accurate and high-quality digital bathymetric surfaces for shallow water coasts. Notably, our research has identified the optimal interpolation method that can be given preference over other methods when the extent of the study area is circular and well-distributed points exist.

Acknowledgments. The authors gratefully acknowledge the science teams of ICESat-2 for providing access to the data. This work was conducted with the infrastructure provided by the National Remote Sensing Centre (NRSC), for which the authors were indebted to the Director, NRSC, Hyderabad. We acknowledge the continued support and scientific insights from Dr. S. K. Srivastav and Dr. Apurba Kumar Bera, Mr. Rakesh Fararoda, Mr. Sagar, S. Salunkhe, Mr. Hansraj Meena, and other staff members of Regional Remote Sensing Centre – West, NRSC/ISRO, Jodhpur. This research did not receive any specific grant from funding agencies in the public, commercial, or not-for-profit sectors.

References

- Amoroso, P. P., U. Falchi, F. G. Figliomeni, and A. Vallario (2023), The Influence of Interpolation Methods and point density on the Accuracy of a Bathymetric Model, in *2023 IEEE International Workshop on Metrology for the Sea; Learning to Measure Sea Health Parameters (MetroSea)*, pp. 148–153, IEEE, <https://doi.org/10.1109/MetroSea58055.2023.10317127>.
- Ashphaq, M., P. K. Srivastava, and D. Mitra (2021), Review of near-shore satellite derived bathymetry: Classification and account of five decades of coastal bathymetry research, *Journal of Ocean Engineering and Science*, 6(4), 340–359, <https://doi.org/10.1016/j.joes.2021.02.006>.
- Becker, M., M. Karpytchev, and F. Papa (2019), Hotspots of Relative Sea Level Rise in the Tropics, in *Tropical Extremes*, pp. 203–262, Elsevier, <https://doi.org/10.1016/B978-0-12-809248-4.00007-8>.
- Brown, M. E., S. D. Arias, and M. Chesnes (2023), Review of ICESat and ICESat-2 literature to enhance applications discovery, *Remote Sensing Applications: Society and Environment*, 29, 100,874, <https://doi.org/10.1016/j.rsase.2022.100874>.
- Burrough, P. A., R. A. McDonnell, and C. D. Lloyd (2015), *Principles of geographical information systems*, 432 pp., Oxford University Press, USA.
- Childs, C. (2004), *Interpolating surfaces in ArcGIS spatial analyst*, ArcUser.
- Collet, S., T. Kidokoro, P. Karamchandani, and T. Shah (2018), Future-Year Ozone Isopleths for South Coast, San Joaquin Valley, and Maryland, *Atmosphere*, 9(9), 354, <https://doi.org/10.3390/atmos9090354>.
- de Souza, E. C. B., C. P. Kruger, and C. R. Sluter (2003), Determinação das variações volumétricas no ISTMO da ilha do mel utilizando PDGPS, *Boletim de Ciências Geodésicas*, 9(1), 53–74.
- Devi, P. Y., and X. Xi (2020), The impacts of climate change on the coastal zone of Mauritius, *Journal of East China Normal University (Natural Science)*, 2020(S1)(104), <https://doi.org/10.3969/j.issn.1000-5641.202092213>.
- Doorga, J. R. S., M. Sadien, N. A. Bheeroo, et al. (2021), Assessment and management of coastal erosion: Insights from two tropical sandy shores in Mauritius Island, *Ocean & Coastal Management*, 212, 105,823, <https://doi.org/10.1016/j.ocecoaman.2021.105823>.
- Duvat, V. K. E., A. Anisimov, and A. K. Magnan (2020), Assessment of coastal risk reduction and adaptation-labelled responses in Mauritius Island (Indian Ocean), *Regional Environmental Change*, 20(4), <https://doi.org/10.1007/s10113-020-01699-2>.

- Dysart, P. S. (1996), Bathymetric surface modeling: A machine learning approach, *Journal of Geophysical Research: Solid Earth*, 101(B4), 8093–8105, <https://doi.org/10.1029/95JB03737>.
- ESRI (2024a), GIS Software for Mapping and Spatial Analytics, <https://www.esri.com>.
- ESRI (2024b), How Kriging works, <https://pro.arcgis.com/en/pro-app/tool-reference/3d-analyst/how-kriging-works.htm>.
- Ferreira, I. O., D. D. Rodrigues, G. Rodrigues dos Santos, and L. M. F. Rosa (2017), In bathymetric surfaces: IDW or Kriging?, *Boletim de Ciências Geodésicas*, 23(3), 493–508, <https://doi.org/10.1590/S1982-21702017000300033>.
- GAGE Facility (2021), Geoid Height Calculator, <https://www.unavco.org/software/geodetic-utilities/geoid-height-calculator/geoid-height-calculator.html>.
- Giribabu, D., R. Hari, J. Sharma, et al. (2023), Prerequisite Condition of Diffuse Attenuation Coefficient Kd(490) for Detecting Seafloor from ICESat-2 Geolocated Photons During Shallow Water Bathymetry, *Hydrology*, 11(1), 11, <https://doi.org/10.11648/j.hyd.20231101.12>.
- Giribabu, D., R. Hari, J. Sharma, et al. (2024), Performance assessment of GEBCO_2023 gridded bathymetric data in selected shallow waters of Indian ocean using the seafloor from ICESat-2 photons, *Marine Geophysical Research*, 45(1), <https://doi.org/10.1007/s11001-023-09534-z>.
- Guo, X., X. Jin, and S. Jin (2022), Shallow Water Bathymetry Mapping from ICESat-2 and Sentinel-2 Based on BP Neural Network Model, *Water*, 14(23), 3862, <https://doi.org/10.3390/w14233862>.
- Hawker, L., and J. Neal (2021), FABDEM V1-0, <https://doi.org/10.5523/BRIS.25WFY0F9UKOGE2GS7A5MQPQ2J7>.
- Henrico, I. (2021), Optimal interpolation method to predict the bathymetry of Saldanha Bay, *Transactions in GIS*, 25(4), 1991–2009, <https://doi.org/10.1111/tgis.12783>.
- Hilldale, R. C., and D. Raff (2007), Assessing the ability of airborne LiDAR to map river bathymetry, *Earth Surface Processes and Landforms*, 33(5), 773–783, <https://doi.org/10.1002/esp.1575>.
- INHO (2024), National Hydrographic Office, <https://hydrobharat.gov.in>.
- Li, J., and A. D. Heap (2014), Spatial interpolation methods applied in the environmental sciences: A review, *Environmental Modelling & Software*, 53, 173–189, <https://doi.org/10.1016/j.envsoft.2013.12.008>.
- Li, Z., Z. Peng, Z. Zhang, et al. (2023), Exploring modern bathymetry: A comprehensive review of data acquisition devices, model accuracy, and interpolation techniques for enhanced underwater mapping, *Frontiers in Marine Science*, 10, <https://doi.org/10.3389/fmars.2023.1178845>.
- Luo, W., M. C. Taylor, and S. R. Parker (2007), A comparison of spatial interpolation methods to estimate continuous wind speed surfaces using irregularly distributed data from England and Wales, *International Journal of Climatology*, 28(7), 947–959, <https://doi.org/10.1002/joc.1583>.
- Markus, T., T. Neumann, A. Martino, et al. (2017), The Ice, Cloud, and land Elevation Satellite-2 (ICESat-2): Science requirements, concept, and implementation, *Remote Sensing of Environment*, 190, 260–273, <https://doi.org/10.1016/j.rse.2016.12.029>.
- Mesić Kiš, I. (2016), Comparison of Ordinary and Universal Kriging interpolation techniques on a depth variable (a case of linear spatial trend), case study of the Šandrovac Field, *Rudarsko-geološko-naftni zbornik*, 31(2), 41–58, <https://doi.org/10.17794/rgn.2016.2.4>.
- National Snow and Ice Data Center (2023), OpenAltimetry: Visualize and download surface elevation data from across the Earth, over time, <https://openaltimetry.earthdatacloud.nasa.gov/data/>.
- Neumann, T. A., A. J. Martino, T. Markus, et al. (2019), The Ice, Cloud, and Land Elevation Satellite-2 mission: A global geolocated photon product derived from the Advanced Topographic Laser Altimeter System, *Remote Sensing of Environment*, 233, 111,325, <https://doi.org/10.1016/j.rse.2019.111325>.

- Parrish, C., L. Magruder, A. Neuenschwander, et al. (2019), Validation of ICESat-2 ATLAS Bathymetry and Analysis of ATLAS's Bathymetric Mapping Performance, *Remote Sensing*, 11(14), 1634, <https://doi.org/10.3390/rs11141634>.
- Pratomo, D. G., R. A. D. Safira, and O. Stefani (2023), A comparison of different GIS-based interpolation methods for bathymetric data: case study of Bawean Island, East Java, *Geodesy and cartography*, 49(4), 186–194, <https://doi.org/10.3846/gac.2023.18250>.
- Ranndal, H., P. Sigaard Christiansen, P. Kliving, O. Baltazar Andersen, and K. Nielsen (2021), Evaluation of a Statistical Approach for Extracting Shallow Water Bathymetry Signals from ICESat-2 ATL03 Photon Data, *Remote Sensing*, 13(17), 3548, <https://doi.org/10.3390/rs13173548>.
- Sibson, R. (1981), A Brief Description of Natural Neighbor Interpolation, in *Interpolating Multivariate Data*, John Wiley & Sons, New York.
- Smith, W. H. F., and D. T. Sandwell (1997), Global Sea Floor Topography from Satellite Altimetry and Ship Depth Soundings, *Science*, 277(5334), 1956–1962, <https://doi.org/10.1126/science.277.5334.1956>.
- Vogt, P. R., and B. E. Tucholke (1986), Imaging the ocean floor: History and state of the art, pp. 19–44, <https://doi.org/10.1130/DNAG-GNA-M.19>.
- Wang, S., G. H. Huang, Q. G. Lin, et al. (2014), Comparison of interpolation methods for estimating spatial distribution of precipitation in Ontario, Canada, *International Journal of Climatology*, 34(14), 3745–3751, <https://doi.org/10.1002/joc.3941>.
- Watson, D. (1992), *Contouring: A Guide to the Analysis and Display of Spatial Data*, Pergamon Press, London.
- Wöfl, A.-C., H. Snaith, S. Amirebrahimi, et al. (2019), Seafloor Mapping - The Challenge of a Truly Global Ocean Bathymetry, *Frontiers in Marine Science*, 6, <https://doi.org/10.3389/fmars.2019.00283>.
- Xie, C., P. Chen, D. Pan, C. Zhong, and Z. Zhang (2021), Improved Filtering of ICESat-2 Lidar Data for Nearshore Bathymetry Estimation Using Sentinel-2 Imagery, *Remote Sensing*, 13(21), 4303, <https://doi.org/10.3390/rs13214303>.

DISTRIBUTION OF DISSOLVED OXYGEN AND NUTRIENTS IN ABYSSAL WATERS FLOWING INTO THE BRAZIL BASIN, SOUTHWEST ATLANTIC

A. M. Seliverstova¹ , O. A. Zuev^{*,1} , D. I. Frey¹ , V. A. Krechik¹ , and E. G. Morozov¹ 

¹Shirshov Institute of Oceanology, Russian Academy of Sciences, Moscow, Russia

* Correspondence to: Oleg Zuev, qillous@gmail.com

Abstract: The Vema Channel is a deep narrow passage in the South Atlantic and a main path for bottom water which flows northward from the Argentine Basin to the Brazil Basin and after all into the North Atlantic. The thermohaline structure and dynamics in it have been studied for many years. In this study we report our new data on dissolved oxygen and nutrients measurements performed in 2022 at the exit of the Vema Channel. This is the first time that such measurements have been made with high spatial resolution. Data from standard oceanographic sections located near the study area are also analyzed. A significant dependence in the distribution of dissolved oxygen and nutrients on the hydrological structure is shown. Local dissolved oxygen minimum indicates the lower boundary of Circumpolar waters. It was also revealed insignificant temporal variability of nutrients concentration.

Keywords: Vema Channel, abyssal waters, dissolved oxygen, silicate, phosphate, nitrate.

Citation: Seliverstova, A. M., O. A. Zuev, D. I. Frey, V. A. Krechik, and E. G. Morozov (2024), Distribution of Dissolved Oxygen and Nutrients in Abyssal Waters Flowing into the Brazil Basin, Southwest Atlantic, *Russian Journal of Earth Sciences*, 24, ES6004, EDN: GJRPBT, <https://doi.org/10.2205/2024es000948>

Introduction

Numerous studies have been conducted in the South Atlantic both within the framework of international ocean circulation research programs and in the course of individual researches of different countries. Such interest is explained by the role of the region in the formation and distribution of several water masses that are key for the entire World Ocean [Holfort and Siedler, 2001; Orsi et al., 2002]. One of them is Antarctic Bottom Water (AABW, $\theta < 2^\circ\text{C}$ by [Wüst, 1936]), which forms in the Weddell Sea and spreads northward in the bottom layer. Through detailed studies, several classifications were proposed dividing AABW into several individual water masses. In our work, we follow the definition [Reid, 1989; Sandoval and Weatherly, 2001] according to which the AABW consists of Weddell Sea Deep Water (WSDW, $\theta < 0.2^\circ\text{C}$) and Lower Circumpolar Water (LCPW, $\theta < 2^\circ\text{C}$). The characteristic features of WSDW are high density and dissolved oxygen, low temperature and salinity; and characteristic features of LCPW are high values of temperature, silicate, and salinity and low dissolved oxygen relative to the underlying WSDW [Mantyla and Reid, 1983].

In its northward flow, the major part of AABW enters the Argentine Basin. The zonally oriented Rio Grande Rise and the Lower Santos Plateau, separating the Argentine and Brazil basins, prevent further free propagation of bottom waters to the north (Figure 1). Water exchange between these basins occurs through the Vema and Hunter channels [Hogg et al., 1999; Speer and Zenk, 1993], as well as over the Lower Santos Plateau [Frey et al., 2018]. The densest WSDW passes only through the Vema Channel. Water with $\theta > 0.2^\circ\text{C}$ passes over the Lower Santos Plateau, and water with $\theta > 0.6^\circ\text{C}$ passes through the Hunter Channel [Sandoval and Weatherly, 2001]. The Vema Channel is a meridionally located deep-water passage by abyssal currents [Gamboa et al., 1983]. It is more than 700 km long, 15–20 km wide with a depth relative to the terraces forming it of about 500 m, the main sill of the channel is located at $31^\circ12'\text{S}$, $39^\circ20'\text{W}$ and its depth is 4614 m [Zenk et al., 1993].

RESEARCH ARTICLE

Received: 10 October 2024

Accepted: 5 November 2024

Published: 30 December 2024



Copyright: © 2024. The Authors. This article is an open access article distributed under the terms and conditions of the Creative Commons Attribution (CC BY) license (<https://creativecommons.org/licenses/by/4.0/>).

Northward of 29°S the Vema Channel is wider and turns northeastward. For deep narrow passage at about 27°S, 34°W we use the name Vema Extension suggested by [Zenk and Morozov, 2007].

Due to its location and structure, the Vema Channel is an excellent object for studying the structure and dynamics of AABW. Different aspects of abyssal circulation, including Ekman layer, Coriolis and bottom friction forces, and potential vorticity conservation were studied in the Vema Channel [Hogg et al., 1982; Johnson et al., 1976; Reid, 1989; Sandoval and Weatherly, 2001]. During the Deep Basin Experiment, a part of the World Ocean Circulation Experiment [Hogg et al., 1996] and latter studies [Hogg et al., 1999; McDonagh et al., 2002; Speer and Zenk, 1993] estimates of velocity and transport of WSDW and LCPW in the Vema Channel were made. The velocity and transport limits are in a wide range, detailed values are given in [Morozov et al., 2021]. Several numerical models were used for calculations of three-dimensional structure of bottom gravity current in the Vema Channel [Frey et al., 2019, 2022; Wadley and Bigg, 1996]. Variability of the AABW flow in the channel was studied at different temporal scales [Campos et al., 2021; Frey et al., 2023; Zenk and Visbeck, 2013].

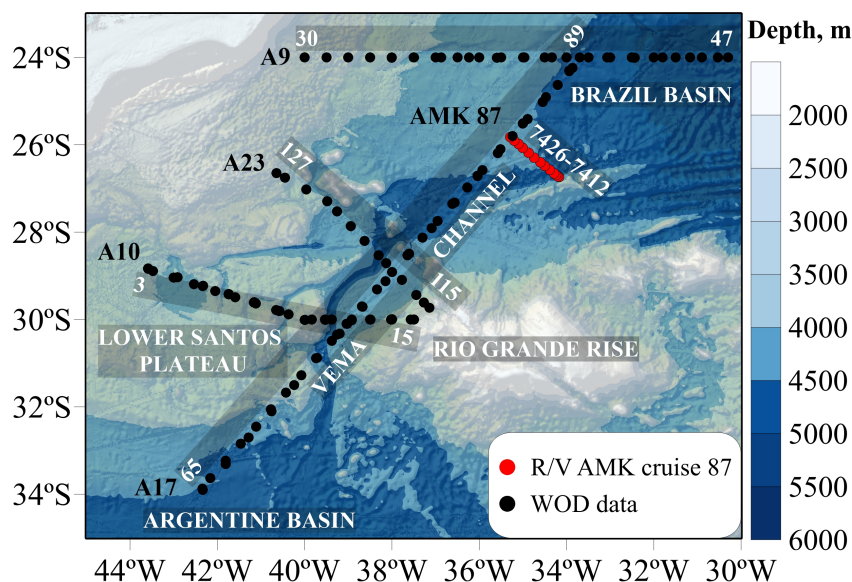


Figure 1. Study area. Red points indicate stations with our measurements in 2022 from 7412 in the southeast to 7426 in the northwest. Black points indicate stations from open databases and sections: A9 (30 and 47 are numbers of the first and last stations in section), A23 (127 and 115), A10 (3 and 15), A17 (65 and 89). The bottom topography is shown according to [GEBCO Bathymetric Compilation Group 2023, 2023].

Much less attention has been paid to the study of hydrochemical indicators in the Vema Channel. The values of individual parameters can be found in review papers on the South Atlantic [Álvarez et al., 2014; Hensen et al., 1998; Holfort and Siedler, 2001; Siedler et al., 1996; Vanicek and Siedler, 2002] or in some oceanographic articles devoted to the hydrology of the Vema Channel [Hernández-Guerra et al., 2019; McDonagh et al., 2002]. However, a detailed description of the hydrochemical structure and its temporal variability in the bottom layer of the channel has not yet been carried out. At the same time, its study and comparison with oceanographic parameters seems interesting both from the point of view of intermediate values between the Argentine and Brazil basins, and for observations of changes in the hydrochemical characteristics in such a complex object as the Vema Channel. Similar studies were carried out in some other deep-water channels, for example, the Vema Fracture Zone [McCartney et al., 1991; Zuev and Seliverstova, 2024], the Equatorial Channel [Andrié et al., 2003] and Azores-Gibraltar Fracture Zone [Krechik et al., 2023], which improved the understanding of the temporal and spatial variability of AABW. In this

study we report our new data on dissolved oxygen and nutrients measurements performed in 2022 in the Vema Channel. This is the first time such measurements have been done with high spatial resolution. The goal of the study was to compare the distribution of dissolved oxygen and nutrients with oceanographic parameters of AABW. A comparison of all parameters in the bottom layer on the continental slope and in the deep bed of the Vema Channel was carried out, the presence and position of the oxygen minimum in LCPW were shown, and the spatial and temporal variability of dissolved oxygen and silicate in the channel area was investigated.

Data and Methods

A total of 13 stations were performed within the Vema Channel from 3 to 6 March 2022 in the 87th cruise of the research vessel *Akademik Mstislav Keldysh*. Oceanographic measurements at stations were made with an Idronaut OCEAN SEVEN 320Plus CTD probe (Italy). The lowered probe is equipped with a high-precision temperature-compensated pressure sensor (PA-10X) with an accuracy of 0.01% and a resolution of 0.002% for the entire measurement range (0–100 m), two redundant temperature sensors with a measurement range from -5 to 45 °C, initial accuracy of 0.001 °C, and a resolution of 0.0001 °C. The two redundant conductivity sensors have a measurement range of 0 to 7 S/m, initial accuracy of 0.0001 S/m, and resolution 0.00001 S/m. The currents were measured with a TRDI Workhorse Monitor Lowered Acoustic Doppler Current profiler (LADCP) with a frequency of 300 kHz. The LADCP data were processed using LDEO Software [Visbeck, 2002]. Additionally, tidal velocities calculated using the software described in [Egbert and Erofeeva, 2002] were taken into account.

Samples for hydrochemical analyzes were taken at the stations with plastic five-liter Niskin bottles of a Carousel Water Sampler system at the depths based on the vertical distribution of potential temperature and salinity. Sampling and determination of hydrochemical parameters were carried out in accordance with accepted methods no later than 6–12 hours after sampling. Dissolved oxygen in seawater was analyzed using the Winkler method modified by Carpenter in 1965 (micromethod) [Cartener, 1965]. Determination of dissolved inorganic silicate was carried out according to the Koroleff method [Grasshoff et al., 2009] with the formation of blue molybdenum complex. When high values of silicate concentration were expected, samples were pre-diluted 1:2 or 1:10 with low-silicate seawater. The sensitivity limit of the element determination was 0.0005 mg/L, the total error of determination was 5.8%. Determination of the concentration of dissolved inorganic phosphate was carried out according to the method of Morphy and Riley [Grasshoff et al., 2009]. The sensitivity limit of the element determination was 0.02 μ M/L. Accuracy index (error limits at probability 0.95) 10%. The determination of nitrate was based on the method of reducing them to nitrite with cadmium and measuring calorimetrically [Grasshoff et al., 2009]. The limit of sensitivity of determination of the element was 0.02 μ M/L, the total error of determination was 7.4%.

We used additional open data of ship observations from the World Ocean Database, 2018 [Boyer et al., 2018]. The main data are A09, A10, A17 and A23 sections from WOCE and CLIVAR projects. The location of sections is shown in Figure 1.

Results and Discussion

Water structure at the Vema Extension section

Distribution of potential temperature at the Vema Extension section (Figure 2) shows features of AABW before it entered the Brazil Basin. The densest and coldest part of AABW was in the deep bed of the Vema Channel (stations 7413–7415), while the water on the western continental slope was warmer, but still significantly colder than 0.2 °C. The bottom homogeneous layer in the Vema Channel with a thickness of 200–250 m was located from the bottom to depths of about 4450 m, the mean potential temperature was -0.06 °C. At stations 7418 and 7419, the homogeneous bottom layer was absent, the minima bottom potential temperatures were 0.11 °C and 0.05 °C, respectively. On the western continental

slope (stations 7420–7425) the bottom homogeneous layer was about 50 m with a spread of potential temperature values of 0.01–0.05 °C. The dynamic structure was consistent with the distribution of potential temperature. In the deep bed of the Vema Channel there was a flow with velocities higher than 20 cm/s, and on the western continental slope there was a flow with velocities higher than 10 cm/s. At the same time, in the bottom layer at stations 7418–7419 there was a flow with velocities of about 5 cm/s in the opposite direction, which corresponds to the absence of a homogeneous layer and the presence of relatively high potential temperature.

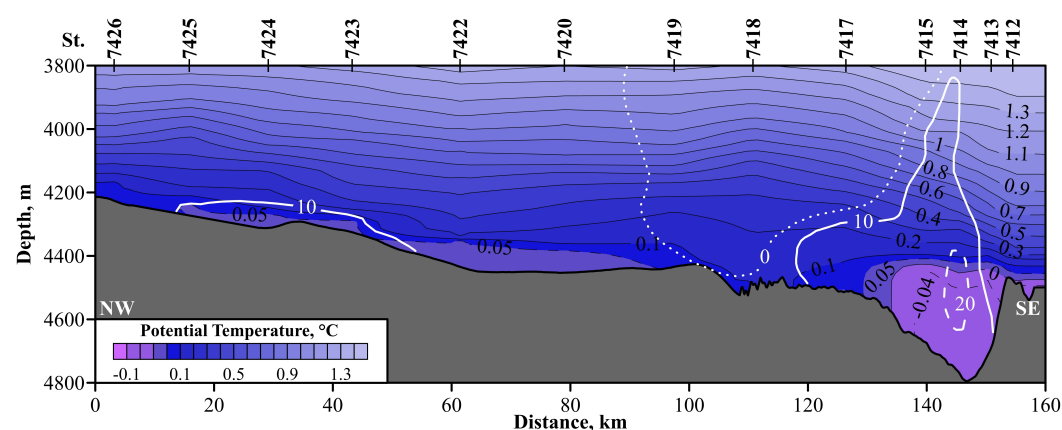


Figure 2. Distribution of potential temperature at the Vema Extension section. The white solid line marks isotach 10 cm/s, the white dashed line marks isotach 20 cm/s, the white dotted line marks isotach 0 cm/s; positive direction is to the northeast, normal to the section. Black lines and numbers at the top axis indicate locations of stations. The bottom topography is shown according to [GEBCO Bathymetric Compilation Group 2023, 2023].

The dissolved oxygen concentration was varied from 5.06 to 5.58 mL/L (Figure 3a). The maximum dissolved oxygen concentration was located at 3800 m in the deep bed of the Vema Channel, the minimum was located at 4150 m and 4168 m at stations 7425 and 7424, respectively. The thickness of the local oxygen minimum layer (5.06–5.09 mL/L) was about 50–100 m and this layer was located at depths from 4400 m in the eastern part of the section to 4100 m in the western part. Below this layer, an increase in the dissolved oxygen concentration was observed (on average to 5.09–5.12 mL/L) with a local maximum at the bottom. The silicate concentration was varied from 57.95 μM to 125.17 μM . (Figure 3b). The minimum was located at 3800 m in the deep bed of the Vema Channel, the maximum was at station 7413 from 4400 m to the bottom. At all stations, a uniform increase in the silicate concentration towards the bottom was observed. The distribution of nitrate was similar to the distribution of silicate (Figure 3c). The range of values was varied from 23.75 μM to 32.86 μM ; the minimum was at 3800 m at stations 7412–7415, the maximum was in the bottom layer at stations 7413 and 7414. The distribution of phosphate was less uniform (Figure 3d). Absolute values were varied from 1.61 μM to 2.25 μM . Increased phosphate was observed in the bottom layer at stations 7415–7419, as well as at stations 7423–7424.

The main feature of the section is the separation of bottom waters both in the vertical and horizontal directions. Thus, the lower boundary of LCPW is distinguished not only by the conventional isotherm of 0.2 °C, but also by the local oxygen minimum. This minimum is observed at all stations of the section, which indicates the existence of WSDW both in the deep bed of the Vema Channel and on the western continental slope. Also, the oxygen isoline of 5.08 mL/L is correlated with the isolines of 111 μM and 31.5 μM silicate and nitrate, respectively. At the same time, the concentrations of nutrients in the bottom homogeneous layer are varied along the section. As expected, the highest silicate (116–120 μM) and nitrate (32–32.4 μM) are located in the deepest part in the main flow of WSDW (Figure 4). Further, with decreasing depth, the concentration of nitrate is

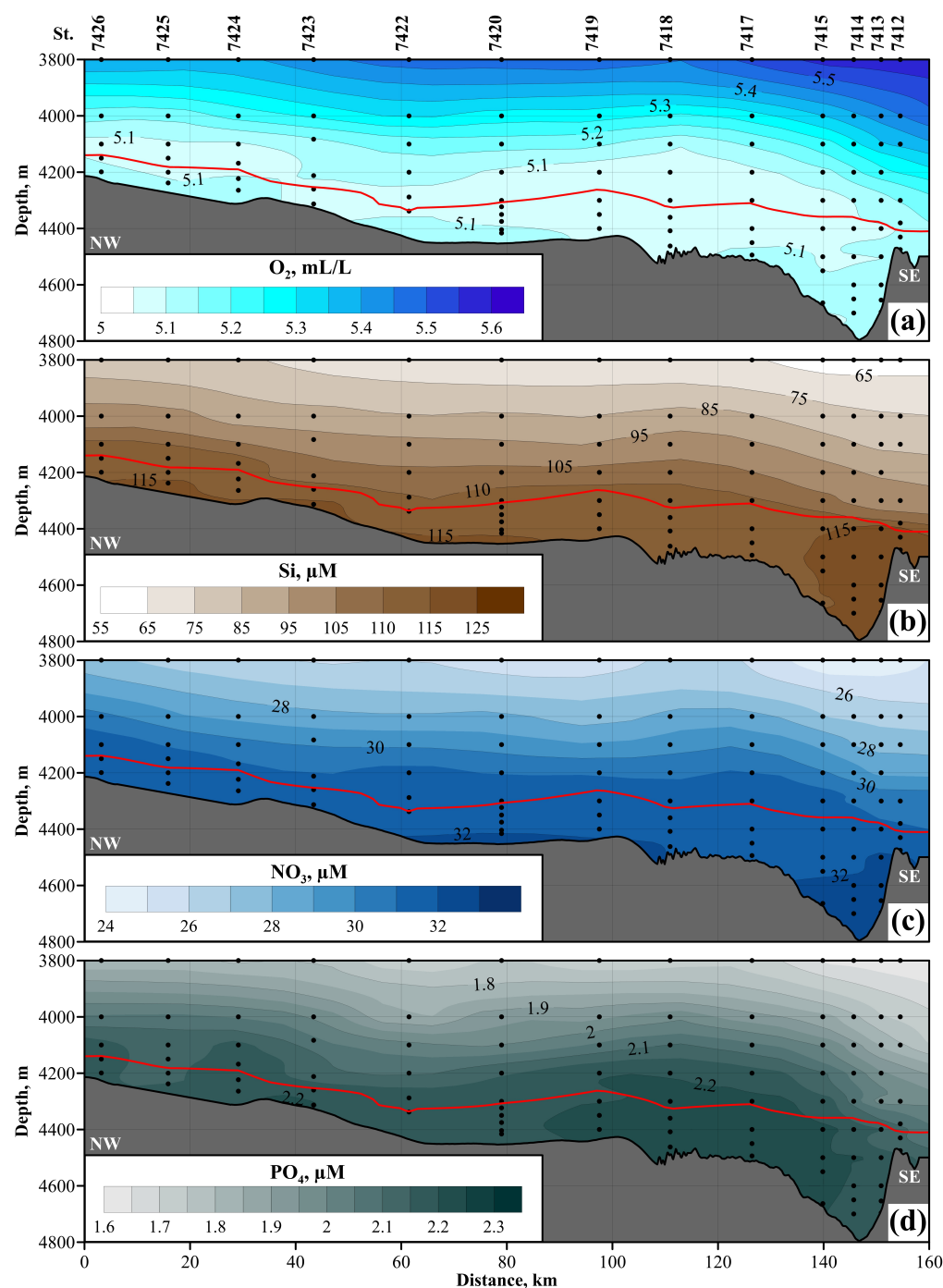


Figure 3. Distributions of (a) dissolved oxygen, (b) silicate, (c) nitrate and (d) phosphate at the Vema Extension section. The red solid line marks isotherm 0.2 °C. Black points and numbers above indicate location of levels and stations. The bottom topography is shown according to [GEBCO Bathymetric Compilation Group 2023, 2023].

decreased almost linearly to 31.6 μM , and concentration of silicate is changed in the range of 112–116 μM with the highest value at station 7423. A flow in the northeast direction with velocities exceeding 10 cm/s is also observed here. The distribution of phosphate is noticeably different: the maximum values are at transition stations 7415–7418, the values on the western continental slope and in the deep bed of the Vema Channel are comparable. Probably, this distribution is associated with the reverse flow at the transition stations. Separately, it is necessary to highlight the easternmost station of the section. It is located outside the Vema Channel and the concentrations of all parameters here are

significantly different, which indicates a much smaller volume of WSDW to the east of the Vema Channel.

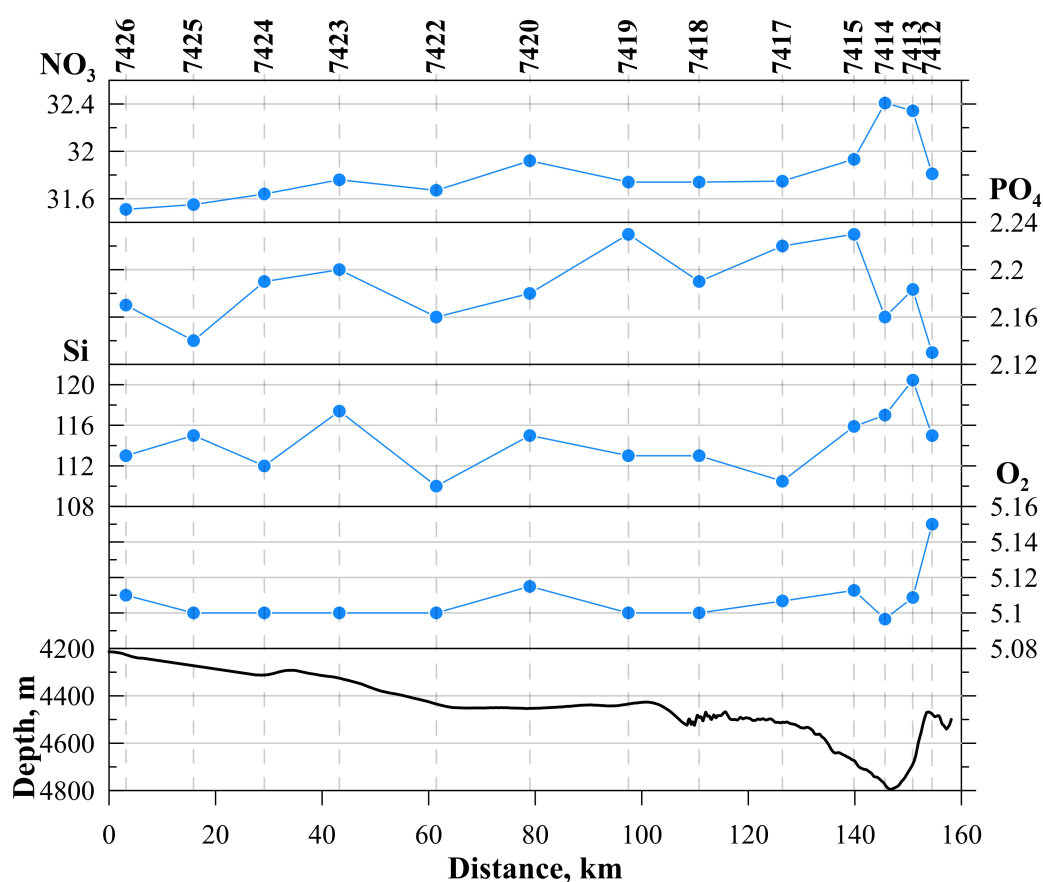


Figure 4. Mean concentrations of dissolved oxygen and nutrients in bottom homogeneous layer. The bottom topography is shown on the lower panel. Data for station 7422 may be incorrect (no measurements at the deepest layer due to technical reasons).

Spatial and temporal variability dissolved oxygen and silicate nearly the Vema Channel

The oxygen minimum in LCPW is observed at other oceanographic sections. Its presence is most clearly expressed in the Argentine Basin: values less than 5 mL/L occupy depths from 3700 m to 4000 m (Figure 5a), respectively, the WSDW thickness here is more than 500 m. A similar pattern is observed in the Vema Channel (station 72). Further, the oxygen minimum disappears, since the stations are located at shallower depths and to the east of the Vema Channel, where WSDW is almost absent. This is clearly seen in sections A10 and A23 (Figure 5b, c): the dissolved oxygen values at the bottom to the east of the Vema Channel are 0.2 mL/L higher than in the western part of the sections. However, even there, an increase in dissolved oxygen toward the bottom is observed only at a few stations, which indicates an insignificant volume of WSDW outside the Vema Channel. On the western continental slope of the Brazil Basin (Figure 5d), separate local oxygen minima are observed, probably related to the division of the bottom water flow into separate jets [Morozov *et al.*, 2022]. The absolute values coincide with the oxygen values over the Lower Santos Plateau, but the layer is much thinner. Further north, the oxygen concentration in the bottom layer is increased, which is consistent with the disappearance of WSDW beyond the Brazil Basin [Álvarez *et al.*, 2014; Vanicek and Siedler, 2002]. This configuration is unique, but there are other extremes characterizing LCPW. Just as the LCPW in the Atlantic appears as oxygen minima and silicate maxima because of the contrasting nature of the deep and bottom water there, it appears as a salinity maximum and silicate minimum in the South

Pacific [Mantyla and Reid, 1983]. The temporal variability of the oxygen concentration in the bottom layer is extremely weak, local changes can be related to measurement errors or to the intensity of the AABW flow.

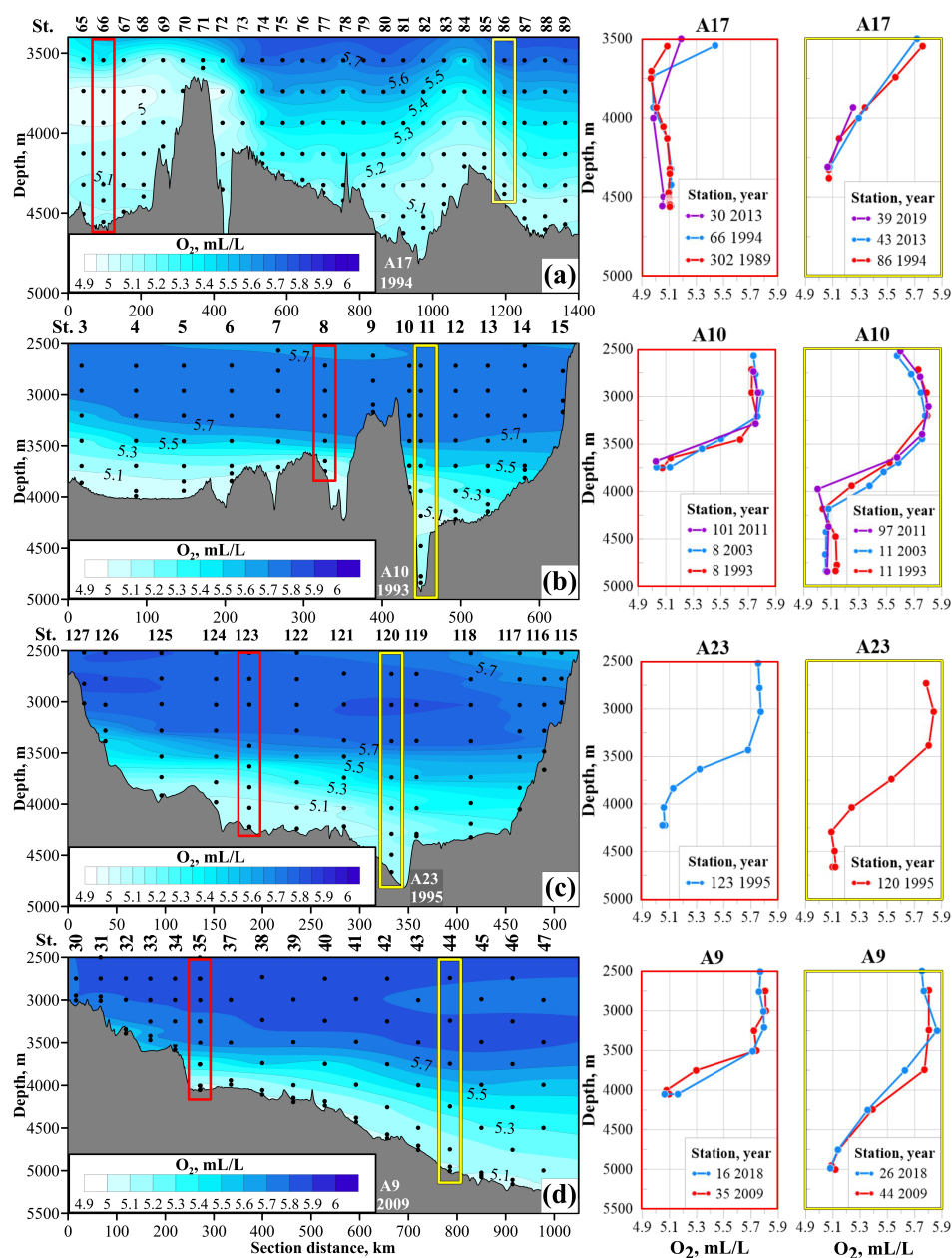


Figure 5. Distribution of dissolved oxygen at (a) A17, (b) A10, (c) A23 and (d) A9 sections. The location of the sections and the first and last station numbers is shown in Fig.1. The bottom topography is shown according to [GEBCO Bathymetric Compilation Group 2023, 2023].

The highest silicate concentrations are found near the bottom in the Argentine Basin. Thus, the silicate maximum here is characteristic of WSDW, and not of LCPW as in the Weddell Sea [Carmack, 1973; Mantyla and Reid, 1983; Mukhametianov et al., 2023]. A significant similarity with the distribution of dissolved oxygen is observed: the presence of its intermediate minimum coincides with the silicate maxima near the bottom, and higher oxygen values correspond to lower silicate concentrations (Figure 6a). The graphs of individual stations for different years show the absence of significant changes of silicate in the bottom layer (Figure 6b, d). The greatest difference is observed in the Argentine Basin, the decrease of silicate was about $8 \mu\text{M}$ from 1989 to 2013. Such changes may be

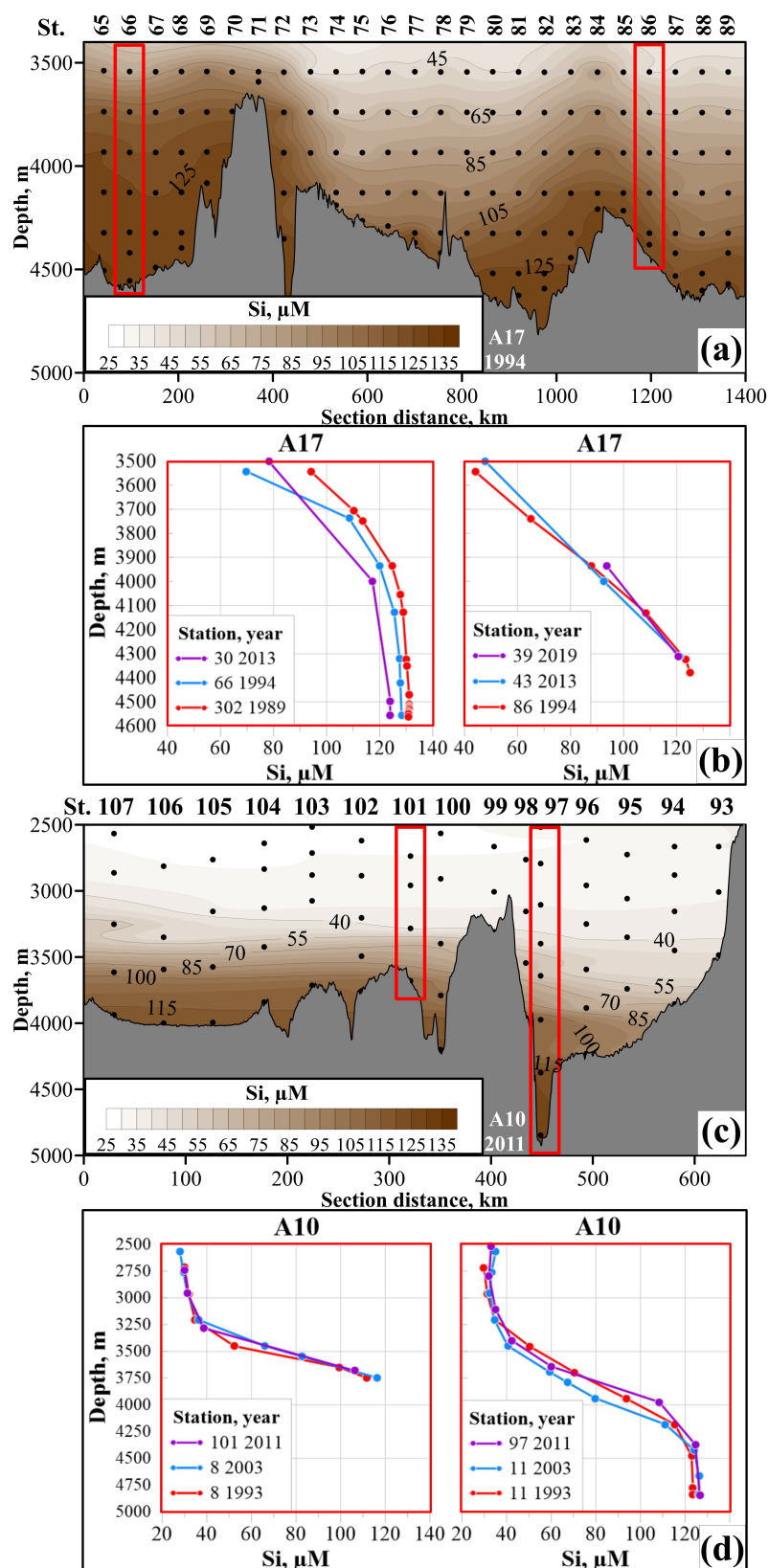


Figure 6. Distribution of silicate at (a) A17 and (c) A10 sections and silicate profiles repeating stations of (b) A17 and (d) A10 sections. The location of the sections and the first and last stations is shown in Fig.1. The bottom topography is shown according to [GEBCO Bathymetric Compilation Group 2023, 2023].

caused by different sources of AABW in the Weddell Sea [Hoppema et al., 2015]. At other points, the silicate distribution is almost the same from year to year, so the warming trend of AABW [Zenk and Morozov, 2007] is not reflected in the silicate concentration. Station 100 on section A10 (Figure 6c) should be noted separately. It is located in one of the small channels of the Santos Plateau and the silicate concentration here is 124.9 μM , which is only slightly less than at station 97, located in the Vema Channel. The minima of the potential temperature also differ slightly: -0.04°C against -0.09°C in the Vema Channel. Thus, it can be assumed that WSDW can flow through individual small channels of the Santos Plateau, but without additional data it is difficult to estimate its volume.

Conclusions

Distribution of dissolved oxygen and nutrients in the abyssal waters near the Vema Channel was analyzed using the in situ data with high spatial resolution. Comparison with potential temperature and current velocities showed significant similarity in distribution even on the horizontal scales of several tens of kilometers. Such water mass tracers as dissolved oxygen and silicate allowed us to identify more accurately the presence and thickness of WSDW over the Vema Extension. Local oxygen minimum on the lower boundary of LCPW was detected in this area. Additional analysis of the open access data showed its strong presence in the Argentine Basin, and poorly noticeable in the Brazil Basin. Silicate concentration complements the pattern of WSDW distribution between the basins. Significant temporal variability in concentrations of dissolved oxygen and nutrients in the bottom layer was not detected. At the same time, significant spatial variability can manifest itself in the presence of high-resolution data, which makes it possible to see additional features of the AABW flow.

Acknowledgments. This work was supported by the Russian Science Foundation grant 24-27-00181.

References

- Álvarez, M., S. Brea, H. Mercier, and X. A. Álvarez Salgado (2014), Mineralization of biogenic materials in the water masses of the South Atlantic Ocean. I: Assessment and results of an optimum multiparameter analysis, *Progress in Oceanography*, 123, 1–23, <https://doi.org/10.1016/j.pocean.2013.12.007>.
- Andrié, C., Y. Gouriou, B. Bourlès, et al. (2003), Variability of AABW properties in the equatorial channel at 35°W , *Geophysical Research Letters*, 30(5), <https://doi.org/10.1029/2002GL015766>.
- Boyer, T. P., O. K. Baranova, C. Coleman, et al. (2018), *World Ocean Database 2018*, NOAA Atlas NESDIS 87.
- Campos, E. J. D., M. C. van Caspel, W. Zenk, et al. (2021), Warming Trend in Antarctic Bottom Water in the Vema Channel in the South Atlantic, *Geophysical Research Letters*, 48(19), <https://doi.org/10.1029/2021GL094709>.
- Carmack, E. C. (1973), Silicate and potential temperature in the deep and bottom waters of the western Weddell Sea, *Deep Sea Research and Oceanographic Abstracts*, 20(10), 927–932, [https://doi.org/10.1016/0011-7471\(73\)90112-5](https://doi.org/10.1016/0011-7471(73)90112-5).
- Cartenter, J. H. (1965), The Chesapeake Bay Institute technique for the Winkler dissolved oxygen method, *Limnology and Oceanography*, 10(1), 141–143, <https://doi.org/10.4319/lo.1965.10.1.0141>.
- Egbert, G. D., and S. Y. Erofeeva (2002), Efficient Inverse Modeling of Barotropic Ocean Tides, *Journal of Atmospheric and Oceanic Technology*, 19(2), 183–204, [https://doi.org/10.1175/1520-0426\(2002\)019<0183:EIMOB0>2.0.CO;2](https://doi.org/10.1175/1520-0426(2002)019<0183:EIMOB0>2.0.CO;2).
- Frey, D. I., V. V. Fomin, R. Y. Tarakanov, et al. (2018), Bottom Water Flows in the Vema Channel and over the Santos Plateau Based on the Field and Numerical Experiments, in *The Ocean in Motion*, pp. 475–485, Springer International Publishing, https://doi.org/10.1007/978-3-319-71934-4_29.
- Frey, D. I., E. G. Morozov, V. V. Fomin, et al. (2019), Regional Modeling of Antarctic Bottom Water Flows in the Key Passages of the Atlantic, *Journal of Geophysical Research: Oceans*, 124(11), 8414–8428, <https://doi.org/10.1029/2019JC015315>.

- Frey, D. I., D. Borisov, V. Fomin, et al. (2022), Modeling of bottom currents for estimating their erosional-depositional potential in the Southwest Atlantic, *Journal of Marine Systems*, 230, 103,736, <https://doi.org/10.1016/j.jmarsys.2022.103736>.
- Frey, D. I., E. G. Morozov, and D. A. Smirnova (2023), Sea level anomalies affect the ocean circulation at abyssal depths, *Scientific Reports*, 13(1), <https://doi.org/10.1038/s41598-023-48074-9>.
- Gamboa, L. A., R. T. Buffler, and P. F. Barker (1983), Seismic Stratigraphy and Geologic History of the Rio Grande Gap and Southern Brazil Basin, in *Initial Reports of the Deep Sea Drilling Project*, 72, U.S. Government Printing Office, <https://doi.org/10.2973/dsdp.proc.72.119.1983>.
- GEBCO Bathymetric Compilation Group 2023 (2023), The GEBCO_2023 Grid - a continuous terrain model of the global oceans and land, <https://doi.org/10.5285/f98b053b-0cbc-6c23-e053-6c86abc0af7b>.
- Grasshoff, K., K. Kremling, and M. Ehrhardt (Eds.) (2009), *Methods of Seawater Analysis*, 634 pp., Wiley-VCH, Hoboken.
- Hensen, C., H. Landenberger, M. Zabel, and H. D. Schulz (1998), Quantification of diffusive benthic fluxes of nitrate, phosphate, and silicate in the southern Atlantic Ocean, *Global Biogeochemical Cycles*, 12(1), 193–210, <https://doi.org/10.1029/97GB02731>.
- Hernández-Guerra, A., L. D. Talley, J. L. Pelegrí, et al. (2019), The upper, deep, abyssal and overturning circulation in the Atlantic Ocean at 30 °S in 2003 and 2011, *Progress in Oceanography*, 176, 102,136, <https://doi.org/10.1016/j.pocean.2019.102136>.
- Hogg, N. G., P. Biscaye, W. Gardener, et al. (1982), On the transport and modification of Antarctic bottom water in the Vema Channel, *Journal of Marine Research*, 40, 231–263.
- Hogg, N. G., W. B. Owens, G. Siedler, and W. Zenk (1996), Circulation in the Deep Brazil Basin, in *The South Atlantic*, pp. 249–260, Springer Berlin Heidelberg, https://doi.org/10.1007/978-3-642-80353-6_13.
- Hogg, N. G., G. Siedler, and W. Zenk (1999), Circulation and Variability at the Southern Boundary of the Brazil Basin, *Journal of Physical Oceanography*, 29(2), 145–157, [https://doi.org/10.1175/1520-0485\(1999\)029<0145:CAVATS>2.0.CO;2](https://doi.org/10.1175/1520-0485(1999)029<0145:CAVATS>2.0.CO;2).
- Holfort, J., and G. Siedler (2001), The Meridional Oceanic Transports of Heat and Nutrients in the South Atlantic, *Journal of Physical Oceanography*, 31(1), 5–29, [https://doi.org/10.1175/1520-0485\(2001\)031<0005:TMOTOH>2.0.CO;2](https://doi.org/10.1175/1520-0485(2001)031<0005:TMOTOH>2.0.CO;2).
- Hoppema, M., K. Bakker, S. M. A. C. van Heuven, et al. (2015), Distributions, trends and inter-annual variability of nutrients along a repeat section through the Weddell Sea (1996–2011), *Marine Chemistry*, 177, 545–553, <https://doi.org/10.1016/j.marchem.2015.08.007>.
- Johnson, D. A., S. E. McDowell, L. G. Sullivan, and P. E. Biscaye (1976), Abyssal hydrography, nephelometry, currents, and benthic boundary layer structure in the Vema Channel, *Journal of Geophysical Research*, 81(33), 5771–5786, <https://doi.org/10.1029/JC081i033p05771>.
- Krechik, V. A., M. V. Kapustina, D. I. Frey, et al. (2023), Properties of Antarctic Bottom Water in the Western Gap (Azores-Gibraltar Fracture Zone, Northeast Atlantic) in 2021, *Deep Sea Research Part I: Oceanographic Research Papers*, 202, 104,191, <https://doi.org/10.1016/j.dsr.2023.104191>.
- Mantyla, A. W., and J. L. Reid (1983), Abyssal characteristics of the World Ocean waters, *Deep Sea Research Part A: Oceanographic Research Papers*, 30(8), 805–833, [https://doi.org/10.1016/0198-0149\(83\)90002-X](https://doi.org/10.1016/0198-0149(83)90002-X).
- McCartney, M. S., S. L. Bennett, and M. E. Woodgate-Jones (1991), Eastward Flow through the Mid-Atlantic Ridge at 11 °N and Its Influence on the Abyss of the Eastern Basin, *Journal of Physical Oceanography*, 21(8), 1089–1121, [https://doi.org/10.1175/1520-0485\(1991\)021<1089:EFTTMA>2.0.CO;2](https://doi.org/10.1175/1520-0485(1991)021<1089:EFTTMA>2.0.CO;2).
- McDonagh, E. L., M. Arhan, and K. J. Heywood (2002), On the circulation of bottom water in the region of the Vema Channel, *Deep Sea Research Part I: Oceanographic Research Papers*, 49(7), 1119–1139, [https://doi.org/10.1016/S0967-0637\(02\)00016-X](https://doi.org/10.1016/S0967-0637(02)00016-X).

- Morozov, E. G., R. Y. Tarakanov, and D. I. Frey (2021), *Bottom Gravity Currents and Overflows in Deep Channels of the Atlantic Ocean: Observations, Analysis, and Modeling*, Springer International Publishing, <https://doi.org/10.1007/978-3-030-83074-8>.
- Morozov, E. G., O. A. Zuev, D. I. Frey, and V. A. Krechik (2022), Antarctic Bottom Water Jets Flowing from the Vema Channel, *Water*, 14(21), 3438, <https://doi.org/10.3390/w14213438>.
- Mukhametianov, R. Z., A. M. Seliverstova, E. G. Morozov, et al. (2023), Hydrological Structure and Water Dynamics in the Powell Basin in January–February 2022, *Oceanology*, 63(4), 472–485, <https://doi.org/10.1134/S0001437023040136>.
- Orsi, A. H., W. M. Smethie, and J. L. Bullister (2002), On the total input of Antarctic waters to the deep ocean: A preliminary estimate from chlorofluorocarbon measurements, *Journal of Geophysical Research: Oceans*, 107(C8), <https://doi.org/10.1029/2001JC000976>.
- Reid, J. L. (1989), On the total geostrophic circulation of the South Atlantic Ocean: Flow patterns, tracers, and transports, *Progress in Oceanography*, 23(3), 149–244, [https://doi.org/10.1016/0079-6611\(89\)90001-3](https://doi.org/10.1016/0079-6611(89)90001-3).
- Sandoval, F. J., and G. L. Weatherly (2001), Evolution of the Deep Western Boundary Current of Antarctic Bottom Water in the Brazil Basin, *Journal of Physical Oceanography*, 31(6), [https://doi.org/10.1175/1520-0485\(2001\)031<1440:EOTDWB>2.0.CO;2](https://doi.org/10.1175/1520-0485(2001)031<1440:EOTDWB>2.0.CO;2).
- Siedler, G., T. J. Müller, R. Onken, et al. (1996), The Zonal WOCE Sections in the South Atlantic, in *The South Atlantic*, pp. 83–104, Springer Berlin Heidelberg, https://doi.org/10.1007/978-3-642-80353-6_5.
- Speer, K. G., and W. Zenk (1993), The Flow of Antarctic Bottom Water into the Brazil Basin, *Journal of Physical Oceanography*, 23(12), 2667–2682, [https://doi.org/10.1175/1520-0485\(1993\)023<2667:TFOABW>2.0.CO;2](https://doi.org/10.1175/1520-0485(1993)023<2667:TFOABW>2.0.CO;2).
- Vanicek, M., and G. Siedler (2002), Zonal Fluxes in the Deep Water Layers of the Western South Atlantic Ocean, *Journal of Physical Oceanography*, 32(8), 2205–2235, [https://doi.org/10.1175/1520-0485\(2002\)032<2205:ZFITDW>2.0.CO;2](https://doi.org/10.1175/1520-0485(2002)032<2205:ZFITDW>2.0.CO;2).
- Visbeck, M. (2002), Deep Velocity Profiling Using Lowered Acoustic Doppler Current Profilers: Bottom Track and Inverse Solutions, *Journal of Atmospheric and Oceanic Technology*, 19(5), 794–807, [https://doi.org/10.1175/1520-0426\(2002\)019<0794:DVPULA>2.0.CO;2](https://doi.org/10.1175/1520-0426(2002)019<0794:DVPULA>2.0.CO;2).
- Wadley, M. R., and G. R. Bigg (1996), Abyssal Channel Flow in Ocean General Circulation Models with Application to the Vema Channel, *Journal of Physical Oceanography*, 26(1), 38–48, [https://doi.org/10.1175/1520-0485\(1996\)026<0038:ACFIOW>2.0.CO;2](https://doi.org/10.1175/1520-0485(1996)026<0038:ACFIOW>2.0.CO;2).
- Wüst, G. (1936), Schichtung und Zirkulation des Atlantischen Ozeans, Das Bodenwasser und die Stratosphäre, in *Wissenschaftliche Ergebnisse, Deutsche Atlantische Expedition auf dem Forschungs- und Vermessungsschiff «Meteor» 1925–1927*, Walter de Gruyter & Co, Berlin (Germany).
- Zenk, W., and E. Morozov (2007), Decadal warming of the coldest Antarctic Bottom Water flow through the Vema Channel, *Geophysical Research Letters*, 34(14), <https://doi.org/10.1029/2007GL030340>.
- Zenk, W., and M. Visbeck (2013), Structure and evolution of the abyssal jet in the Vema Channel of the South Atlantic, *Deep Sea Research Part II: Topical Studies in Oceanography*, 85, 244–260, <https://doi.org/10.1016/j.dsr2.2012.07.033>.
- Zenk, W., K. G. Speer, and N. G. Hogg (1993), Bathymetry at the Vema Sill, *Deep Sea Research Part I: Oceanographic Research Papers*, 40(9), 1925–1933, [https://doi.org/10.1016/0967-0637\(93\)90038-5](https://doi.org/10.1016/0967-0637(93)90038-5).
- Zuev, O., and A. Seliverstova (2024), Spatial Variability of the Hydrochemical Structure in Bottom Gravity Current in the Vema Fracture Zone, *Russian Journal of Earth Sciences*, <https://doi.org/10.2205/2024es000945>.

KINEMATIC CHARACTERISTICS OF ICEBERG D28 DRIFT USING SATELLITE DATA SENTINEL-1A/B SAR

A. E. Pogrebnoi¹  and V. N. Belokopytov^{*,1} 

¹Marine Hydrophysical Institute RAS, Sevastopol, Russia

* **Correspondence to:** Vladimir Belokopytov, belokopytov.vn@mhi-ras.ru

Abstract: The goal of the article is to track down the giant tabular iceberg D28 trajectory from its calving in September 2019 from Amery Ice Shelf until reaching the western part of the Weddell Sea in March 2023 and to present characteristics of the iceberg state and movement, derived from satellite radar data. The Maximally Stable Extremal Regions (MSER) method, which used as an imagery recognition technique for time-dependent visual conditions, has been applied to automatically identify iceberg's positions. On the basis of the Sentinel-1A/B SAR data during 1,275 days, time-series of D28 location, spatial orientation, mass, area, moment of inertia, linear and angular velocity, kinetic and rotational energy, grounding location are presented. D28 dynamics display strongly pronounced regionality, generalized into the three distinct sections of its drift along the Antarctic coast. These sections are in good agreement with existent concepts in the oceanographic literature, concerning the system of Antarctic Slope Current / Antarctic Slope Front.

Keywords: Antarctic, iceberg D28, iceberg dynamics, satellite radar imaging, iceberg grounding, Antarctic Slope Current.

Citation: Pogrebnoi, A. E., V. N. Belokopytov (2024), Kinematic Characteristics of Iceberg D28 Drift Using Satellite Data Sentinel-1A/B SAR, *Russian Journal of Earth Sciences*, 24, ES6005, EDN: JDLXMM, <https://doi.org/10.2205/2024es000940>

1. Introduction

The development of remote sensing methods has provided new, comprehensive opportunities for monitoring the polar regions of the World Ocean, which were impossible in the recent past. Accompanied by field measurements, it enables to detect dozens of large iceberg calvings and trace their further motion [Budge and Long, 2018; Morozov et al., 2021; Stuart and Long, 2011]. From a practical point of view, tracking icebergs is a traditional task of maritime safety and offshore oil and gas production. In the environmental aspect, icebergs plough up bottom sediments during grounding events, cause underwater landslides, and affects vital activity of marine benthos [Barnes and Souster, 2011; Normandeau et al., 2021]. Climatic importance of the icebergs formation process is evident, since it accounts for a significant part of the total mass loss of Antarctic glaciers [Liu et al., 2015]. In addition to the direct loss of glacier mass, iceberg calvings lead to a change of grounded ice flow dynamics from the interior regions of Antarctic to the ocean, increasing its speed [Greenbaum et al., 2015; Hogg and Gudmundsson, 2017; Smith et al., 2019]. The fundamental question: is whether the frequency and intensity of iceberg calving a stationary process that maintains the long-term stable state of the glacier and weakly depends on external forcing [King et al., 2009; Li et al., 2020] or it directly responds to global warming signal [Pritchard et al., 2012; Shepherd et al., 2018] is still understood incompletely.

One of the such events was calving the gigantic tabular iceberg D28, which broke off in September 2019 from the Amery Ice Shelf (AIS) in East Antarctic. According to [Fricker et al., 2002], the cycle of icebergs calving in AIS is 60–70 years and the last major event occurred in 1963–1964. Several works have been devoted to the physical conditions preceding the birth of D28 and the external disturbances that led to the final iceberg detachment from the glacier [Francis et al., 2021; Walker et al., 2021; Zhu et al., 2021]. The drift path and D28 characteristics, such as speed, moving direction, rotation, size, area,

RESEARCH ARTICLE

Received: 13 March 2024

Accepted: 11 October 2024

Published: 30 December 2024



Copyright: © 2024. The Authors. This article is an open access article distributed under the terms and conditions of the Creative Commons Attribution (CC BY) license (<https://creativecommons.org/licenses/by/4.0/>).

draft, grounding locations, calculated from SCATSAT and Sentinel data for the period from September 2019 to February 2021, were considered in [Liu *et al.*, 2021; Mitkari *et al.*, 2021; Singh *et al.*, 2021, 2023].

The purpose of this article is to track down the iceberg D28 path from its calving in the Commonwealth Sea in September 2019 until reaching the western part of the Weddell Sea in March 2023 and to present the characteristics of the motion and state of the iceberg, supplementing them, in comparison with previous works, by new parameters.

2. Materials and Methods

2.1. Iceberg Selection

To select objects in satellite snapshots automatically, various image analysis methods are used, including those developed for computer vision technologies. The Canny Edge Detection method is sufficiently widespread [Canny, 1986; McIlhagga, 2010], according to which the boundaries of an object are determined by the maximum brightness gradient of the image, previously smoothed with the Gaussian filter. It was used to search the boundaries of glaciers and icebergs, for example, in [Mitkari *et al.*, 2021; Singh *et al.*, 2021, 2023; Yu *et al.*, 2019]. Another widely used method is the Constant False Alarm Rate (CFAR) [Gandhi and Kassam, 1988], based on the digital filters related to the local region statistics. To study ice shelves and icebergs CFAR was used in [Silva and Bigg, 2005; Zhu *et al.*, 2021]. Histogram method determines the threshold value to minimize internal variance of the black and white pixels distribution [Otsu, 1979]. It was applied to identify surface manifestations of internal waves and ice floes in the Arctic Ocean [Pogrebnoi, 2023]. Also, methods designed to classify continental landscapes are used to select icebergs, such as the Object Based Image Analyzes (OBIA) [Mazur *et al.*, 2017], machine learning methods [Barbat *et al.*, 2021] and many others.

In this work the Maximally Stable Extremal Regions (MSER) method was applied to identify iceberg D28, which is commonly used for visual pattern recognition, while processing a stream of images under changing conditions of observations, such as different perspectives, lighting, complicated rotations and object deformations [Matas *et al.*, 2004]. For icebergs, which are also rotating and deformed objects, the application of this method seems to be promising.

In case when the iceberg touched the ice shelf or neighboring ice floes and its visible shape was significantly distorted, it was necessary to use manual image processing and at the same time keeping strict control over the selection subjectivity. High albedo of the snow surface usually enables clearly identify icebergs as objects with high brightness. During the Antarctic summer (January–February) or when entering temperate latitudes, the iceberg images become darker as the snow melts. These difficulties can be partly solved by the image inversion. The main problem in object detection arises when the brightness of the iceberg and its surroundings are comparable, or when one part of the iceberg is significantly lighter than other part. In this case, the image was rejected, which of course reduced the length of resulting time-series.

In general, 338 reliable and 45 partially reliable locations and spatial orientations of the iceberg D28 were derived from the C-band synthetic aperture radar measurements onboard Sentinel 1/A and Sentinel 1/B satellites for the period from 2019-09-25 to 2023-03-23 (1275 days).

2.2. Kinematic Characteristics

The iceberg linear velocity V was determined from loxodromic distances in the WGS84 reference coordinate system with the NAD83 datum. The iceberg area S was calculated as the number of cells with size of 1×1 km in the Lambert Conformal Conic map projection (LCC) coordinates. The iceberg mass M was calculated from the area S , taking into account the iceberg draft of 220–270 m, according to [Liu *et al.*, 2021], and the sea water density of $1,028 \text{ kg/m}^3$.

To calculate the azimuthal orientation α and angular rotation velocity ω , the shape of the iceberg was approximated by an ellipse, and the azimuthal angle α was defined as clockwise angle between the north direction and the semi-major axis position of the approximating ellipse. Axis direction ambiguity is 180° , therefore the iceberg was projected into the reference system associated with its center of mass and this axis was directed along the y ordinate. The direction with the largest number of matching pixels between a given iceberg shape and the reference shape was accepted as the true direction. Any iceberg image, for example, the first one, can be selected as a reference shape. Figure 1 represents various examples of projections associated with the center of mass and the direction of the iceberg semi-major axis, including initial AIS calving event. Reduction images to the unified projection promotes effective quality control in animation mode of identification results preview. To provide the maximal continuity of azimuthal orientation time-series, images with partially or not very reliable fixations were also took into account.

The kinetic energy of the iceberg progressive motion was determined by the linear velocity V and the mass of the iceberg M :

$$K_v = \frac{MV^2}{2}.$$

The iceberg rotational energy was calculated from the angular velocity and moment of inertia:

$$K_\omega = \frac{J\omega^2}{2},$$

where ω – angular velocity $J = \sum_{i=1}^n m_i r_i^2$ – moment of inertia, m_i – mass of an ice column per i -cell, r_i – distance from the center of the i -cell to the center of iceberg mass (center of the approximating ellipse).

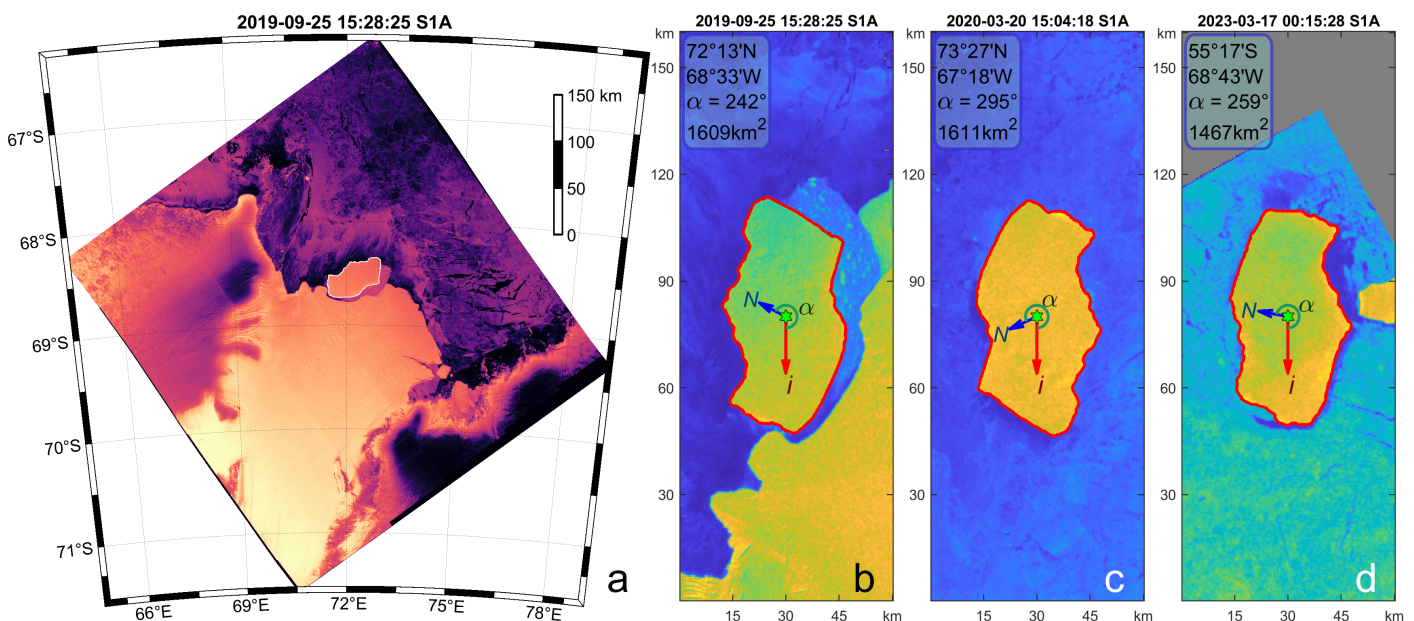


Figure 1. (a) Initial image of D28 calving from Amery Ice Shelf, iceberg boundaries are outlined by the white line; (b), (c) and (d) images in some time points of the iceberg D28 drift. N – direction to the North, i – orientation of the iceberg ellipse major semiaxis, α – azimuthal angle.

2.3. Iceberg Groundings

Determination of the iceberg grounding events was calculated as follows. The velocity $\mathbf{V} = \mathbf{i} \cdot V_x + \mathbf{j} \cdot V_y$ in a point $\mathbf{r} = \mathbf{i} \cdot x + \mathbf{j} \cdot y$ in a coordinate system moving at speed \mathbf{V}_0 is defined by the relation:

$$\mathbf{V} = \mathbf{V}_0 + \omega \times \mathbf{r},$$

where V_0 – forward velocity, $\omega = \mathbf{k} \times \omega$ – angular velocity of the coordinate system. The reference point in the coordinate system, for which at a given time $V_0 = 0$, is a stationary center of rotation. For it:

$$\mathbf{V} = \mathbf{i} \cdot V_x + \mathbf{j} \cdot V_y = \omega \times \mathbf{r} = \begin{vmatrix} \mathbf{i} & \mathbf{j} & \mathbf{k} \\ 0 & 0 & \omega \\ x & y & 0 \end{vmatrix} = -\mathbf{i} \cdot \omega \cdot y + \mathbf{j} \cdot \omega \cdot x,$$

which makes it possible to determine the coordinates of the stationary center of rotation. A possible indication of an iceberg grounding may be the matching this center with any point of the iceberg in several consecutive images.

3. Results and Discussion

3.1. Drift Trajectory

The drift trajectories of icebergs D28 as well as other recent gigantic icebergs A68 and A76 (Figure 2) correspond to the general pattern of a steady, nearly continuous ice transport around Antarctic: eastward in the Antarctic Circumpolar Current (ACC) and westward along the continental coast [Emery *et al.*, 1997].

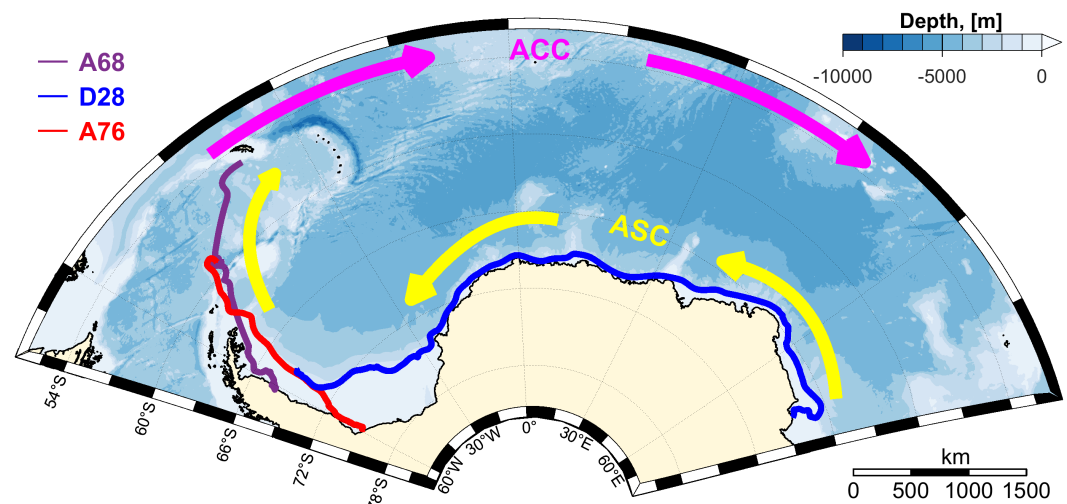


Figure 2. Trajectories of icebergs A68, D28 and A76. Labelling: ACC – Antarctic Circumpolar Current, ASC – Antarctic Slope Current.

The motion of icebergs along the continental coast is exerted by various forcing: easterly katabatic winds, the Antarctic Coastal Current and, for the most part, the Antarctic Slope Front/Antarctic Slope Current (ASC) system [Jacobs, 1991]. Due to a weak density stratification the geographical position of ASC is largely determined by the bottom topography (conservation of potential vorticity f/H) and mainly corresponds to the isobath of 1,000 m or 400–500 m in certain areas of the continental slope [Azaneu *et al.*, 2017; Gill, 1973; Heywood *et al.*, 2004; Whitworth *et al.*, 2013].

Iceberg D28 traveled more than 6,000 km along the Antarctic coast over 1,275 days for the period under review (from 2019-09-25 to 2023-03-23) (Figure 3). Changes in its characteristics (size, mass, speed, etc.) have a well-defined regional nature: 1st section of the iceberg drift is the leg from Prydz Bay in the Commonwealth Sea to the Cosmonauts Sea (0–550 days), 2nd section is the path from the Riiser-Larsen Sea to the Brunt Ice Shelf in the northeastern part of the Weddell Sea (550–800 days) and 3rd section is wide shelf part of the Weddell Sea (> 800 days of the drift).

3.2. Kinematic Characteristics

Variations of the iceberg area in the 1st drift section ranged from 1,560 to 1,630 km², decreasing on average from 1,600 to 1,570 km² (Figure 4). Small changes of the estimated

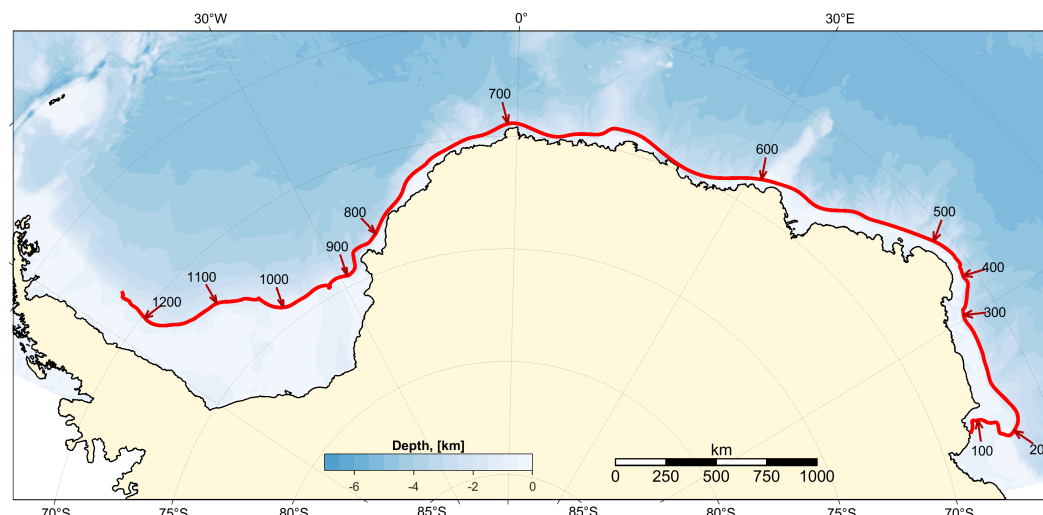


Figure 3. The iceberg D28 path along the Antarctic coast, digits denote the drift duration in days.

iceberg geometric dimensions are caused not only by methodical errors of determining its boundaries, but also with the physical processes of addition/loss of smaller floating ice cover. After crossing the underwater Gunnerus Ridge between the Cosmonauts Sea and the Riiser-Larsen Sea, iceberg D28 began rapidly reduce its size and mass, especially in the Riiser-Larsen Sea and the Lazarev Sea. The iceberg area during the 2nd drift section decreased on average from 1,570 to 1,460 km². After entering the open part of the Weddell Sea, the size of D28 was stabilized, with a slight increase in the western part of the sea (> 1,200 days of the drift).

During the drift period of consideration (3.5 years), iceberg D28 made 13 complete anticyclonic rotations (counterclockwise in the southern hemisphere), of which 9 cycles occurred in the second year of drift while passing from the Cosmonauts Sea to the eastern part of the Weddell Sea (Figure 4).

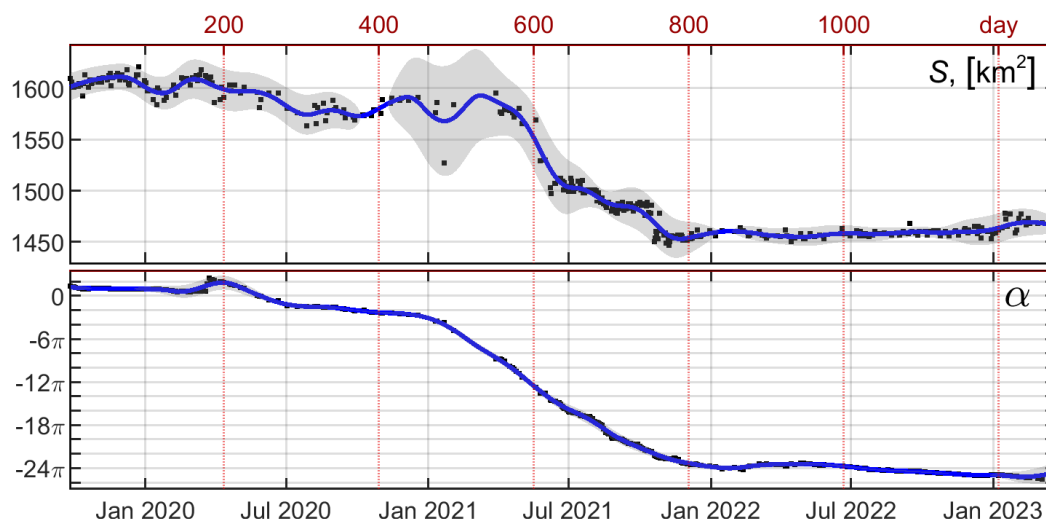


Figure 4. Time-series of area S and azimuth orientation α of the iceberg D28. The 95%-confidence level is painted over by grey color.

The linear velocity of iceberg D28 (Figure 5) was maximal in the 2nd section of the drift (from 30°W to 20°E), reaching 20–30 cm/s in the vicinity of the underwater Gunnerus Ridge and the Fimbul Ice Shelf (0–5°E). The iceberg moving speed within 1st and 3rd sections generally in 5–10 times lower than speed in the 2nd section, except some local maxima in the Commonwealth Sea (65°–70°E) and the Weddell Sea (35°–40°W), reaching 5–10 cm/s. Regional features of the angular speed are similar to those of the linear velocity

(Figure 5). The iceberg rotates much more intensely in the 2nd drift section, and the local maximum of linear velocity in the Commonwealth Sea tightly corresponds to the increase in angular speed, while the local velocity maximum in the Weddell Sea has less influence on the angular velocity. When D28 rounded the Brunt Ice Shelf (25°W), an increase of angular velocity with reverse (cyclonic) rotation was observed.

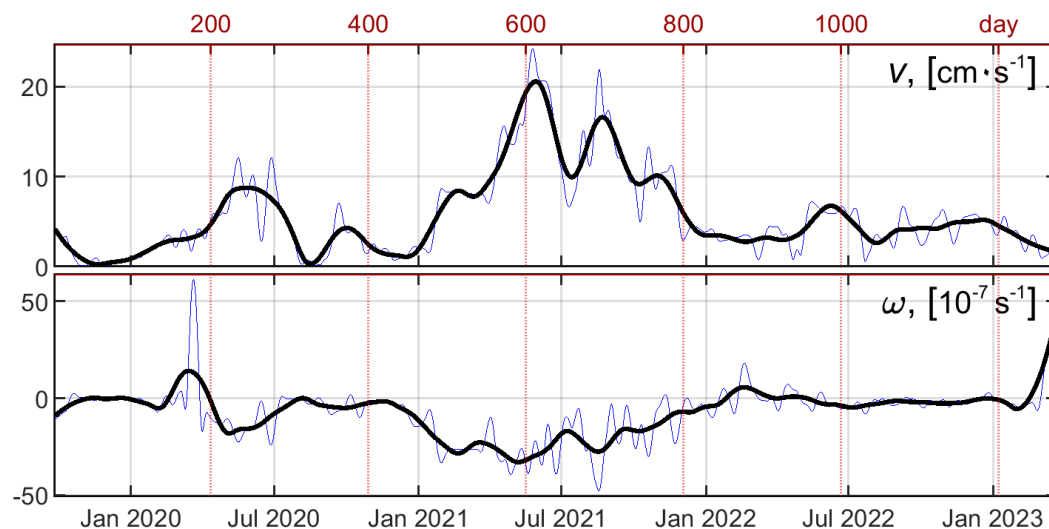


Figure 5. Time-series of linear V and angular ω velocity of the iceberg D28. Bold line represents data smoothed by regression 1st degree polynomial filter (120-day window).

Since the mass and moment of inertia were calculated via the surface area of the iceberg, these characteristics vary in accordance with iceberg dimensions, that is, they sharply decrease in the 2nd section of the trajectory and stabilize when reaching a wide shelf of the Weddell Sea (Figure 6). Distribution of the iceberg kinetic energy qualitatively corresponds to variations of linear and angular velocities, taking into account the mass loss of D28 during the drift (Figure 7).

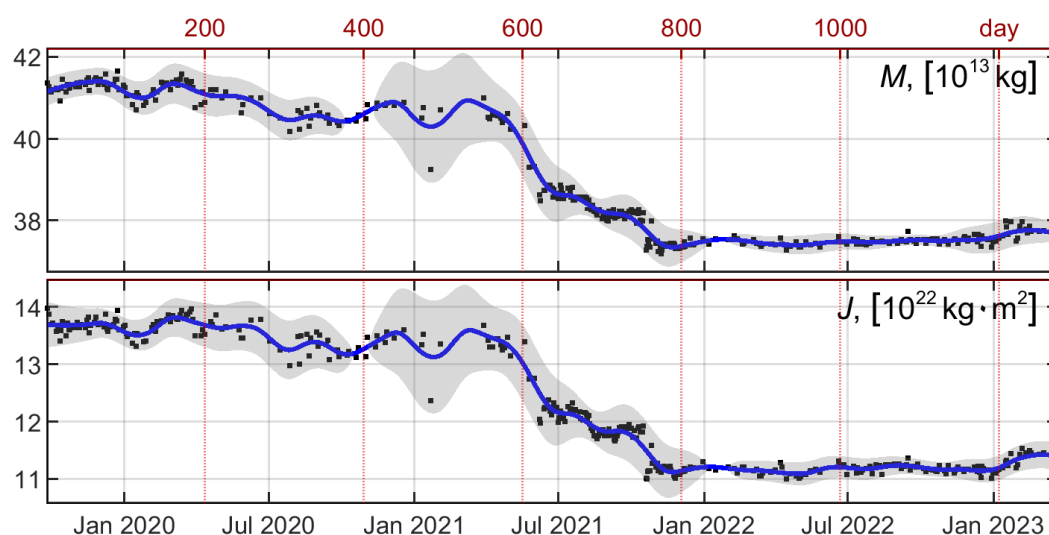


Figure 6. Time-series of mass M and moment of inertia J of the iceberg D28. The 95%-confidence level is painted over by grey color.

Noteworthy is the high consistency of the iceberg D28 time-series V and ω . For example, icebergs A68 and A76, started in other oceanographic conditions (in the region of the Antarctic Peninsula), do not manifest such a high correlation between V and ω .

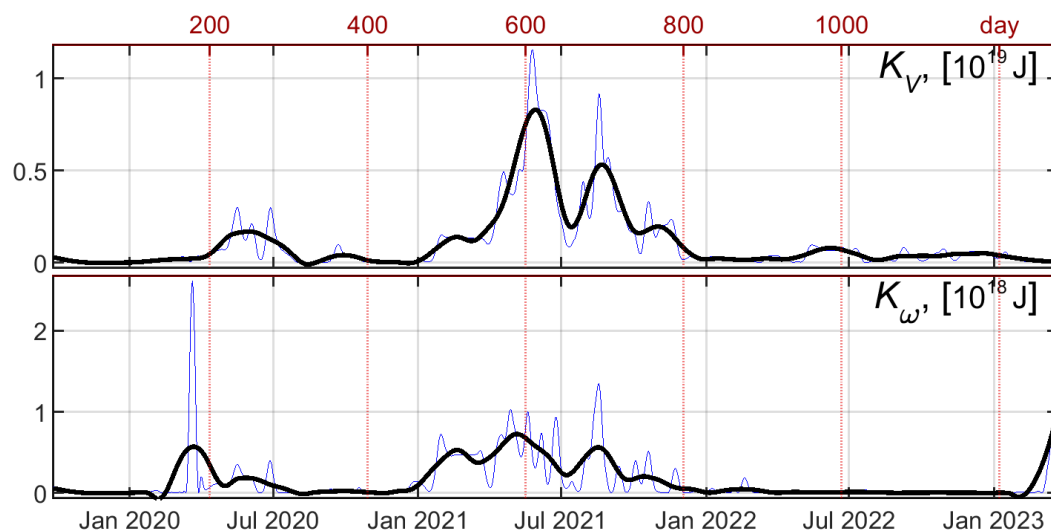


Figure 7. Time-series of kinetic K_V and rotational K_ω energy of the iceberg D28.

Obviously, in a case of coastal current, flow vorticity will primarily depend on shear instability, which is determined by the lateral velocity gradient, i.e. by current speed and distance from the shore. To assess a contribution of this simple mechanism to the general vorticity of the iceberg's motion, a linear regression model was used:

$$\omega = A + B \cdot \Omega,$$

where ω – observed angular velocity, $\Omega = V/D/2$ – model angular velocity, V – linear velocity, D – nearest distance from the iceberg to the shore, $A = -3.2033 \times 10^{-7}$, $B = 1.1649$.

Figure 8 shows the distance D and superposition of angular velocities ω and Ω . Despite the rough assumptions (the inertia of the iceberg is not taken into account, the gradient assumed as linear, the distance is measured to a zero depth value when the iceberg draft is about 250 m, other vorticity components are not examined), the correlation between ω and Ω is distinctly high ($R = 0.76$, $R^2 = 0.57$, with a vanishingly small probability of the null hypothesis). Thus, about 57% of the variability of the iceberg angular velocity ω can be explained by the simple mechanism of linear flow shear near the coastline.

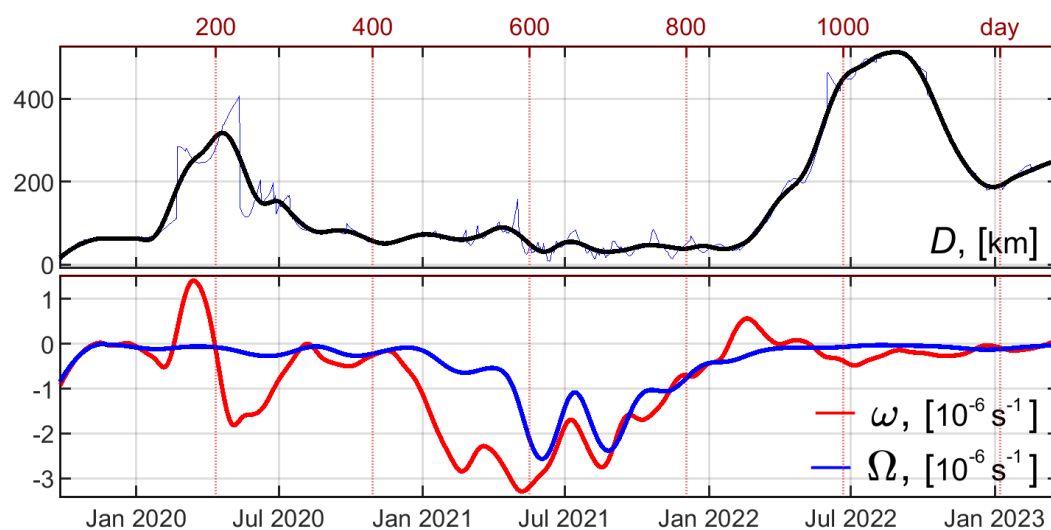


Figure 8. Distance D between the shore and the iceberg D28, angular velocities: observed ω and model Ω .

3.3. Iceberg Groundings

The underwater draft (220–270 m) and groundings of iceberg D28 at the initial stage of its drift in August–September 2020 were revealed in [Liu *et al.*, 2021], using altimeter data from the Cryosat-2, Sentinel-3, and ICESat 2 satellites. According to the digital bottom relief gridded products Bedmap2 and BedMachine, the depths at these points are greater than the iceberg draft by 570 m and 350 m, respectively. This once again is an evidence of the rugged bottom topography in the coastal zone of Antarctic and the insufficient number of hydrographic surveys. Spatial localization of iceberg groundings can be useful for correcting and clarifying the underwater topography of these areas.

According to the above described method for calculating locations of motionless rotation centers, 23 cases of probable iceberg D28 groundings were identified. Examples of the iceberg rotation and motion during these events are presented in Figure 9. Grounding point locations and their depth according to ETOPO_2022_v1_15s gridded data are given in Table 1. Some of these points are very close in time and space, so they probably represent the same grounding events. Negative values of angular velocity ω relative to a stationary center of rotation correspond to anticyclonic movement. In several cases, the iceberg changed the prevailing anticyclonic rotation to the cyclonic one (Figure 9c).

During the iceberg braking episodes, huge angular rotation velocities have been revealed (Table 1). These events are not associated with a weakening of background currents and visual analysis of corresponding images does not confirm ice-bound conditions or pressing iceberg against the ice edge. All detected stationary centers of rotation are located inside the iceberg and are most likely the places where D28 took aground.

Table 1. Grounding events and rotation velocity of the iceberg D28 around stationary points

From date	To date	Longitude	Latitude	$\omega, 10^{-4}$ cycle/day	$H, \text{ m}$
2019-10-24	2019-10-26	70°47.5'E	68°29.5'S	−17	800
2019-11-05	2019-11-07	70°53.6'E	68°20.7'S	−25	730
2019-11-17	2019-11-19	70°42.8'E	68°12.2'S	−35	395
2020-01-16	2020-01-18	70°54.8'E	67°58.3'S	−28	499
2020-01-28	2020-02-04	71°1.6'E	67°33.7'S	−72	409
2020-03-18	2020-03-20	73°13.1'E	67°16.4'S	−112	539
2020-03-20	2020-03-23	73°11.3'E	67°14.5'S	−312	541
2020-08-10	2020-08-18	58°27.3'E	66°25.2'S	−54	545
2020-08-18	2020-08-20	58°59.4'E	66°17.1'S	−33	1,870
2020-08-30	2020-09-01	59°25.7'E	66°25.1'S	−12	2,154
2020-09-03	2020-09-11	58°26.0'E	66°23.0'S	−93	479
2020-09-11	2020-09-13	58°33.4'E	66°18.5'S	−117	478
2020-10-19	2020-10-21	56°22.1'E	65°46.4'S	−184	507
2020-11-24	2020-11-26	54°37.2'E	65°31.6'S	17	774
2021-11-25	2021-11-30	21°5.3'W	73°23.1'S	−164	284
2022-02-17	2022-02-19	27°44.7'W	74°18.7'S	356	2,319
2022-03-07	2022-03-11	27°49.0'W	74°33.0'S	16	1,726
2022-07-20	2022-07-24	42°42.0'W	73°13.4'S	−176	1,408
2022-07-24	2022-07-29	42°37.0'W	73°22.4'S	−83	1,263
2022-08-29	2022-09-01	45°48.6'W	72°42.6'S	−82	1,182
2022-11-12	2022-11-13	52°25.6'W	71°33.4'S	149	1,775
2023-01-04	2023-01-05	55°44.9'W	70°5.8'S	75	1,176
2023-02-27	2023-03-05	55°38.6'W	68°41.3'S	−105	1,238

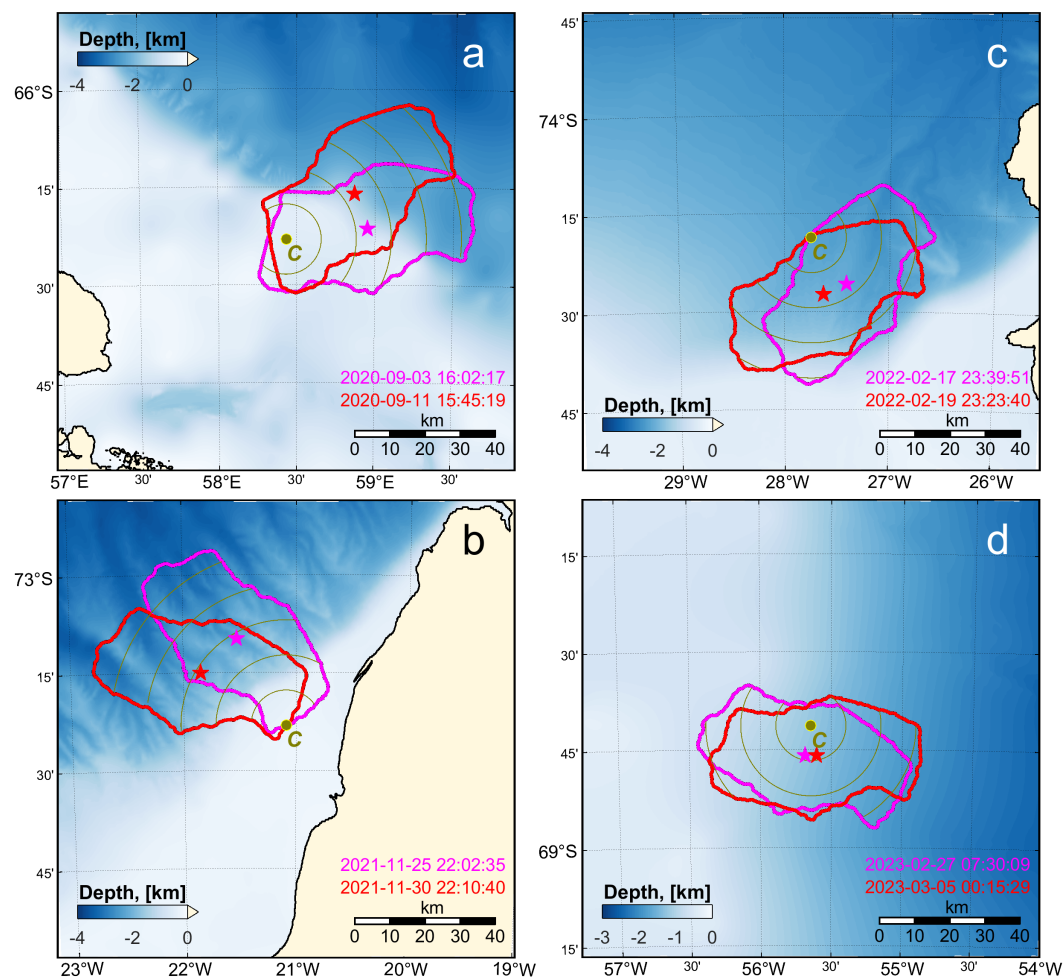


Figure 9. Iceberg D28 positions during grounding events. (a) Region of the Kemp Land in the Commonwealth Sea in September 2020, (b), (c) region of the Brunt ice shelf in the Weddell Sea in November 2021, February 2022, (d) region of the Larsen ice shelf in the Weddell Sea, March 2023. Green circles show centers of rotation, asterisks denote centers of the iceberg mass.

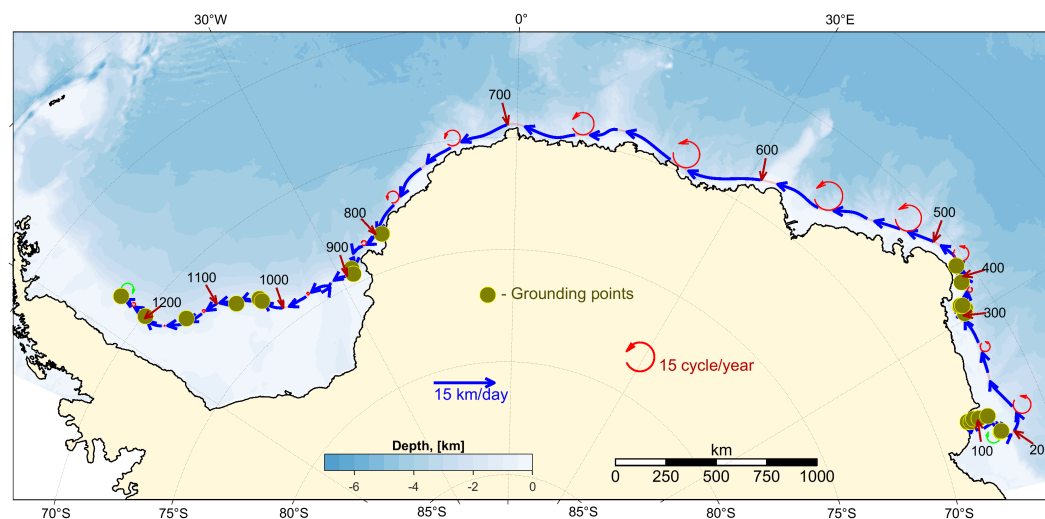


Figure 10. Locations of possible groundings of the iceberg D28. Drift vectors present 20-day movements with 5-day intervals between them. “Circle vectors”, presented angular velocities ω , are drawn with 50-day intervals. Vector linear dimensions are proportional values of V and ω and the legend.

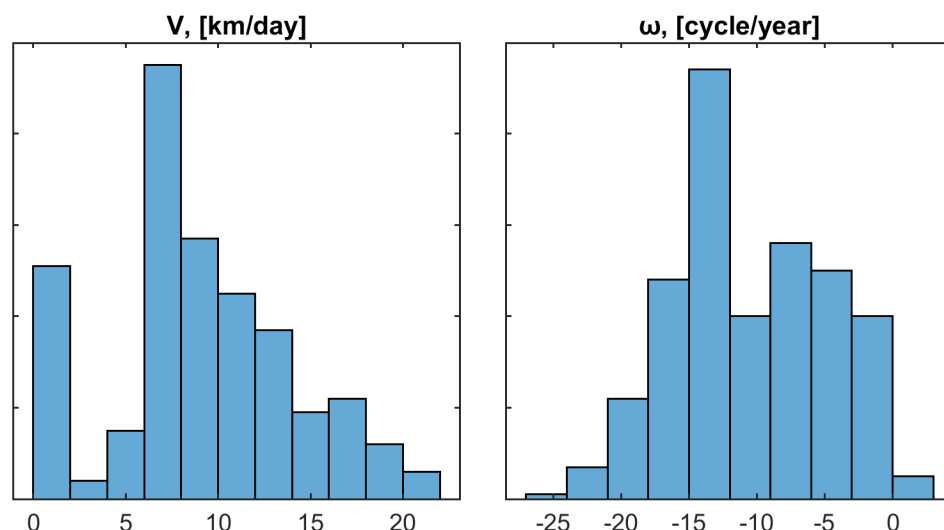


Figure 11. Histograms of linear velocity V and angular velocity ω in the non-stop section of the iceberg D28 drift.

Locations of possible iceberg D28 groundings, drift vectors and the “circular vectors” of the rotation angular velocity are shown in Figure 10. During the drift period from 26-11-2020 to 25-11-2021 along the Bellingshausen Ice Shelf from the Kemp Land ($54^{\circ}37.2'E$, $65^{\circ}31.6'S$) to the Cape Vestkapp ($21^{\circ}31.6'W$, $73^{\circ}9.8'S$) no cases of touching the bottom were found. It can be considered that in this section of the drift, the kinematic characteristics of the D28 motion are the most representative for integral flux in the layer of the iceberg draft (about 250 m). Figure 11 and Table 2 present statistics of linear velocity V and angular velocity ω in this non-stop section of the iceberg D28 trajectory.

Table 2. Statistics of linear velocity V and angular velocity ω in the non-stop section of the iceberg D28 drift

	V , km/day	ω , cycle/year
Maximum	20.9	−24.1
Median	8.81	−11.6
Average	9.2	−10.5
Standard deviation	4.9	5.6

4. Conclusions

The ongoing variations of the iceberg kinematic characteristics during D28 drift along the Antarctic coast are in fairly good agreement with the classification of the frontal and dynamic structure of the Antarctic Slope Current presented in [Thompson *et al.*, 2018]. The 2nd section of the D28 trajectory (from the Riiser-Larsen Sea to the Brunt Ice Shelf), with the highest speed of motion and rotation, falls on the “fresh shelf” category (according to the classification [Thompson *et al.*, 2018]). Here the ASC velocity is maximal, due to the strong katabatic easterly winds and a sharp slope thermohaline front, extending from the sea surface to the bottom. High velocity and fast rotation in this area most likely lead to intensification of mechanical destruction and a rapid decrease of the iceberg size and mass. The 1st and 3rd sections of the D28 trajectory (Commonwealth Sea, Cosmonauts Sea and Weddell Sea) according to the classification [Thompson *et al.*, 2018] belong to the “dense shelf”. Easterly winds in these regions weaken, dense shelf waters, descending down the continental slope, displace the thermohaline front to the sea surface and the ASC speed decreases. The motion of iceberg D28 is significantly slowing down, the area and mass of the iceberg become stabilized.

Localization of the iceberg D28 grounding sites within the 1st and 3rd sections of the drift can be associated with several factors: weakening of the ASC, which favoured to the iceberg deceleration even while soft bottom contact occurs, complicated underwater terrain in the form of ridges and canyons, strong eddy structures, which disturbing the iceberg path with deviations towards shallower depths. According to studies of ASC mesoscale and submesoscale variability [Azaneu *et al.*, 2017; Stewart and Thompson, 2015; Wang *et al.*, 2009], emergence and development of eddies is often associated with jets of dense shelf water descending along the continental slope to participate further in the Antarctic Bottom Water (AABW) formation. Such processes are intrinsic to “dense shelves” (according to the classification [Thompson *et al.*, 2018]), which include the 1st and 3rd sections of the D28 drift. Low ASC speed also reduces stream stability and increases meandering, bending iceberg paths.

The contribution of linear shear instability to ASC vorticity is significantly reduced in the Commonwealth Sea, where the southern boundary of the ACC zone approaches the counter-directed ASC, as well in the Kemp Land and Brunt Ice Shelf regions.

In general, drifting icebergs, in addition to their practical, ecological and climatic significance, can be considered in a certain sense as a tool that allows to assess indirectly some oceanographic processes in Antarctic.

Acknowledgments. This research was funded by Marine Hydrophysical Institute RAS, State Tasks FNNN-2021-0010, FNNN-2024-0014.

References

- Azaneu, M., K. J. Heywood, B. Y. Queste, and A. F. Thompson (2017), Variability of the Antarctic Slope Current System in the Northwestern Weddell Sea, *Journal of Physical Oceanography*, 47(12), 2977–2997, <https://doi.org/10.1175/JPO-D-17-0030.1>.
- Barbat, M. M., T. Rackow, C. Wesche, et al. (2021), Automated iceberg tracking with a machine learning approach applied to SAR imagery: A Weddell sea case study, *ISPRS Journal of Photogrammetry and Remote Sensing*, 172, 189–206, <https://doi.org/10.1016/j.isprsjprs.2020.12.006>.
- Barnes, D. K. A., and T. Souster (2011), Reduced survival of Antarctic benthos linked to climate-induced iceberg scouring, *Nature Climate Change*, 1(7), 365–368, <https://doi.org/10.1038/nclimate1232>.
- Budge, J. S., and D. G. Long (2018), A Comprehensive Database for Antarctic Iceberg Tracking Using Scatterometer Data, *IEEE Journal of Selected Topics in Applied Earth Observations and Remote Sensing*, 11(2), 434–442, <https://doi.org/10.1109/JSTARS.2017.2784186>.
- Canny, J. (1986), A Computational Approach to Edge Detection, *IEEE Transactions on Pattern Analysis and Machine Intelligence*, PAMI-8(6), 679–698, <https://doi.org/10.1109/TPAMI.1986.4767851>.
- Emery, W. J., C. W. Fowler, and J. A. Maslanik (1997), Satellite-derived maps of Arctic and Antarctic sea ice motion: 1988 to 1994, *Geophysical Research Letters*, 24(8), 897–900, <https://doi.org/10.1029/97GL00755>.
- Francis, D., K. S. Mattingly, S. Lhermitte, M. Temimi, and P. Heil (2021), Atmospheric extremes triggered the biggest calving event in more than 50 years at the Amery Ice shelf in September 2019, *The Cryosphere*, 15, 2147–2165, <https://doi.org/10.5194/tc-2020-219>.
- Fricker, H. A., N. W. Young, I. Allison, and R. Coleman (2002), Iceberg calving from the Amery Ice Shelf, East Antarctica, *Annals of Glaciology*, 34, 241–246, <https://doi.org/10.3189/172756402781817581>.
- Gandhi, P. P., and S. A. Kassam (1988), Analysis of CFAR processors in nonhomogeneous background, *IEEE Transactions on Aerospace and Electronic Systems*, 24(4), 427–445, <https://doi.org/10.1109/7.7185>.
- Gill, A. E. (1973), Circulation and bottom water production in the Weddell Sea, *Deep Sea Research and Oceanographic Abstracts*, 20(2), 111–140, [https://doi.org/10.1016/0011-7471\(73\)90048-X](https://doi.org/10.1016/0011-7471(73)90048-X).
- Greenbaum, J. S., D. D. Blankenship, D. A. Young, et al. (2015), Ocean access to a cavity beneath Totten Glacier in East Antarctica, *Nature Geoscience*, 8(4), 294–298, <https://doi.org/10.1038/ngeo2388>.

- Heywood, K. J., A. C. Naveira Garabato, D. P. Stevens, and R. D. Muench (2004), On the fate of the Antarctic Slope Front and the origin of the Weddell Front, *Journal of Geophysical Research: Oceans*, 109(C6), <https://doi.org/10.1029/2003JC002053>.
- Hogg, A. E., and G. H. Gudmundsson (2017), Impacts of the Larsen-C Ice Shelf calving event, *Nature Climate Change*, 7(8), 540–542, <https://doi.org/10.1038/nclimate3359>.
- Jacobs, S. S. (1991), On the nature and significance of the Antarctic Slope Front, *Marine Chemistry*, 35(1–4), 9–24, [https://doi.org/10.1016/S0304-4203\(09\)90005-6](https://doi.org/10.1016/S0304-4203(09)90005-6).
- King, M. A., R. Coleman, A.-J. Freemantle, et al. (2009), A 4-decade record of elevation change of the Amery Ice Shelf, East Antarctica, *Journal of Geophysical Research: Earth Surface*, 114(F1), <https://doi.org/10.1029/2008JF001094>.
- Li, T., Y. Liu, and X. Cheng (2020), Recent and imminent calving events do little to impair Amery ice shelf's stability, *Acta Oceanologica Sinica*, 39(5), 168–170, <https://doi.org/10.1007/s13131-020-1600-6>.
- Liu, X., X. Cheng, Q. Liang, et al. (2021), Grounding Event of Iceberg D28 and Its Interactions with Seabed Topography, *Remote Sensing*, 14(1), 154, <https://doi.org/10.3390/rs14010154>.
- Liu, Y., J. C. Moore, X. Cheng, et al. (2015), Ocean-driven thinning enhances iceberg calving and retreat of Antarctic ice shelves, *Proceedings of the National Academy of Sciences*, 112(11), 3263–3268, <https://doi.org/10.1073/pnas.1415137112>.
- Matas, J., O. Chum, M. Urban, and T. Pajdla (2004), Robust wide-baseline stereo from maximally stable extremal regions, *Image and Vision Computing*, 22(10), 761–767, <https://doi.org/10.1016/j.imavis.2004.02.006>.
- Mazur, A. K., A. K. Wåhlin, and A. Krężel (2017), An object-based SAR image iceberg detection algorithm applied to the Amundsen Sea, *Remote Sensing of Environment*, 189, 67–83, <https://doi.org/10.1016/j.rse.2016.11.013>.
- McIlhagga, W. (2010), The Canny Edge Detector Revisited, *International Journal of Computer Vision*, 91(3), 251–261, <https://doi.org/10.1007/s11263-010-0392-0>.
- Mitkari, K., J. Pallipad, D. Putrevu, and A. Misra (2021), Detecting Calving Events of Icebergs D-28 and B-49 using High Resolution Sentinel-1A SAR Data, *EGU General Assembly 2021, online, 19-30 Apr 2021, EGU21-16264*, <https://doi.org/10.5194/egusphere-egu21-16264>.
- Morozov, E. G., V. A. Krechik, D. I. Frey, and V. V. Zamshin (2021), Currents in the Western Part of the Weddell Sea and Drift of Large Iceberg A68A, *Oceanology*, 61(5), 589–601, <https://doi.org/10.1134/S000143702105009X>.
- Normandeau, A., K. MacKillop, M. Macquarrie, et al. (2021), Submarine landslides triggered by iceberg collision with the seafloor, *Nature Geoscience*, 14(8), 599–605, <https://doi.org/10.1038/s41561-021-00767-4>.
- Otsu, N. (1979), A Threshold Selection Method from Gray-Level Histograms, *IEEE Transactions on Systems, Man, and Cybernetics*, 9(1), 62–66, <https://doi.org/10.1109/TSMC.1979.4310076>.
- Pogrebnoi, A. E. (2023), Estimation of Internal Wave Parameters in the Arctic Based on Synthetic Aperture Satellite Radar Data, *Physical Oceanography*, 30(1), 98–111, <https://doi.org/10.29039/1573-160X-2023-1-98-111>.
- Pritchard, H. D., S. R. M. Ligtenberg, H. A. Fricker, et al. (2012), Antarctic ice-sheet loss driven by basal melting of ice shelves, *Nature*, 484(7395), 502–505, <https://doi.org/10.1038/nature10968>.
- Shepherd, A., H. A. Fricker, and S. L. Farrell (2018), Trends and connections across the Antarctic cryosphere, *Nature*, 558(7709), 223–232, <https://doi.org/10.1038/s41586-018-0171-6>.
- Silva, T. A. M., and G. R. Bigg (2005), Computer-based identification and tracking of Antarctic icebergs in SAR images, *Remote Sensing of Environment*, 94(3), 287–297, <https://doi.org/10.1016/j.rse.2004.10.002>.
- Singh, K. N., R. K. Singh, M. Maisnam, et al. (2021), Detection of Two Recent Calving Events in Antarctica from SCATSAT-1, in *2021 IEEE International Geoscience and Remote Sensing Symposium IGARSS*, pp. 439–442, IEEE, <https://doi.org/10.1109/IGARSS47720.2021.9553306>.
- Singh, K. N., M. Maisnam, R. K. Singh, et al. (2023), Spatio-temporal monitoring of the iceberg D28 using SCATSAT-1 data, *Polar Record*, 59, <https://doi.org/10.1017/S0032247423000062>.

- Smith, J. A., A. G. C. Graham, A. L. Post, et al. (2019), The marine geological imprint of Antarctic ice shelves, *Nature Communications*, 10(1), <https://doi.org/10.1038/s41467-019-13496-5>.
- Stewart, A. L., and A. F. Thompson (2015), Eddy-mediated transport of warm Circumpolar Deep Water across the Antarctic Shelf Break, *Geophysical Research Letters*, 42(2), 432–440, <https://doi.org/10.1002/2014GL062281>.
- Stuart, K. M., and D. G. Long (2011), Tracking large tabular icebergs using the SeaWinds Ku-band microwave scatterometer, *Deep Sea Research Part II: Topical Studies in Oceanography*, 58(11–12), 1285–1300, <https://doi.org/10.1016/j.dsr2.2010.11.004>.
- Thompson, A. F., A. L. Stewart, P. Spence, and K. J. Heywood (2018), The Antarctic Slope Current in a Changing Climate, *Reviews of Geophysics*, 56(4), 741–770, <https://doi.org/10.1029/2018RG000624>.
- Walker, C. C., M. K. Becker, and H. A. Fricker (2021), A High Resolution, Three-Dimensional View of the D-28 Calving Event From Amery Ice Shelf With ICESat-2 and Satellite Imagery, *Geophysical Research Letters*, 48(3), <https://doi.org/10.1029/2020GL091200>.
- Wang, Q., S. Danilov, and J. Schröter (2009), Bottom water formation in the southern Weddell Sea and the influence of submarine ridges: Idealized numerical simulations, *Ocean Modelling*, 28(1–3), 50–59, <https://doi.org/10.1016/j.ocemod.2008.08.003>.
- Whitworth, T., A. H. Orsi, S.-J. Kim, W. D. Nowlin, and R. A. Locarnini (2013), *Water Masses and Mixing Near the Antarctic Slope Front*, pp. 1–27, American Geophysical Union, <https://doi.org/10.1029/AR075p0001>.
- Yu, Y., Z. Zhang, M. Shokr, et al. (2019), Automatically Extracted Antarctic Coastline Using Remotely-Sensed Data: An Update, *Remote Sensing*, 11(16), 1844, <https://doi.org/10.3390/rs11161844>.
- Zhu, T., X. Cui, and Y. Zhang (2021), Analysis of Temporal and Spatial Variability of Fronts on the Amery Ice Shelf Automatically Detected Using Sentinel-1 SAR Data, *Remote Sensing*, 13(17), 3528, <https://doi.org/10.3390/rs13173528>.

WHAT SHOULD WE KNOW TO PREDICT GEOMAGNETICALLY INDUCED CURRENTS IN POWER TRANSMISSION LINES?

V. A. Pilipenko^{*,1,2} , O. V. Kozyreva² , V. B. Belakhovsky³ , Ya. A. Sakharov³ , and V. V. Selivanov⁴ 

¹Geophysical Center of Russian Academy of Sciences, Moscow, Russia

²Schmidt Institute of Physics of the Earth, Moscow, Russia

³Polar Geophysical Institute, Apatity, Russia

⁴Institute of Northern Energetics, Apatity, Russia

* **Correspondence to:** Vyacheslav Pilipenko, space.soliton@gmail.com

Abstract: This review considers several issues of space weather studies that are directly related to the problem of geomagnetically induced current (GIC) excitation in the power line transmission systems. Expectations to reduce the damage to technological systems from space weather were related with elaboration of models capable of real-time predictions of electromagnetic disturbances at the Earth's surface. However, the examination of the feasibility of the MHD simulation to predict the level of geomagnetic field variability, and consequently GICs, during the May 27–28, 2017 storm showed that the modeling reasonably well reproduced the global magnetospheric parameters, but the predicted magnetic field variability dB/dt has turned out to be more than order of magnitude less than that observed. The reason is the inability of current global MHD models to adequately predict the fine structure of the storm/substorm – Pi3 disturbances, and consequently GICs that they drive. Moreover, impulsive disturbances such as Pi3 pulsations demand a special tool for their analysis. Data processing technique for a 2D network of magnetic stations has to be elaborated to automatically recognize eddy current structures in the ionosphere and estimate their characteristics. The proposed technique applied to Pi3 pulsations on March 17, 2013 revealed that each vortex caused a disturbance of the vertical magnetic component Z and GIC burst up to ~ 100 A. The efficiency of GIC generation by different types of magnetic storms must be examined. For that it is necessary to compare GIC responses to storms caused by coronal mass ejection and by corotating interaction region, and to estimate the normalized GIC-effectiveness of each storm. The excitation rate of GIC during storms may be associated with the occurrence of mesoscale current vortices.

Keywords: magnetic storm, substorms, magnetic impulsive events, ionospheric vortex, geomagnetically induced currents, Pi3 pulsations, power transmission lines.

Citation: Pilipenko, V. A., O. V. Kozyreva, V. B. Belakhovsky, Ya. A. Sakharov, and V. V. Selivanov (2024), What Should We Know to Predict Geomagnetically Induced Currents in Power Transmission Lines?, *Russian Journal of Earth Sciences*, 24, ES6006, EDN: VETPKC, <https://doi.org/10.2205/2024es000954>

RESEARCH ARTICLE

Received: 3 August 2024

Accepted: 21 November 2024

Published: 30 December 2024



Copyright: © 2024. The Authors. This article is an open access article distributed under the terms and conditions of the Creative Commons Attribution (CC BY) license (<https://creativecommons.org/licenses/by/4.0/>).

Introduction

One of the most harmful factors of space weather for technological systems is electric geomagnetically induced currents (GICs) caused by rapid changes of the geomagnetic field \mathbf{B} , i.e., large values of dB/dt . GICs associated with intense magnetic disturbances were found to be dangerous for various technological systems, causing overheating of industrial transformers, imbalance of power line transmission, malfunction of railway equipment, disruption of communication cables, reduction of the lifetime of pipelines, etc. (see references in review [Pilipenko, 2021]). For example, the catastrophe of the Hydro Quebec energy system was caused by a storm with $dB/dt \sim 480$ nT/min [Kappenman, 2005], although the impact of GIC on power lines was also observed at much lower $dB/dt \sim 100$ nT/min

[[Pirjola et al., 2005](#)]. The highest risk of GIC may be related not directly to global magnetic storm/substorms processes with enormous energy yield, but to more local and rapid processes. Such meso-scale processes embedded into storm/substorm evolution can be the actual drivers of GIC bursts [[Belakhovsky et al., 2019](#)]. The abrupt disturbances that appear in magnetometers during nighttime may be associated with substorm onsets, isolated magnetic impulse events with a duration of ~ 5–15 min [[Engebretson et al., 2020](#)], quasi-periodic series of such impulses – geomagnetic Pi3 pulsations (quasi-periods around 5–20 min) [[Kozyreva et al., 2019](#); [Yagova et al., 2021](#)], and quasi-monochromatic Pc5 pulsations [[Heyns et al., 2021](#)]. Some authors introduce in the Pi3 frequency band additional subclasses of ultra-low-frequency (ULF) pulsations, such as Ps6 or Pc6, but for brevity we call all of them as Pi3 pulsations. Though the power of such impulsive processes is much lower than the magnetic storm power, the rapidly varying electromagnetic fields of these events can induce a significant GIC [[Apatenkov et al., 2020](#); [Ngwira et al., 2018](#); [Viljanen and Pirjola, 1994](#)]. In general, meso-scale disturbances on short timescales may be considered as a kind of the space weather “tornadoes”. Any progress in building the effective system for the GIC prediction demands the solution of several mutually related problems on these “tornadoes”. Here we consider several issues of the fine time-spatial structure of storm/substorm and discuss some efforts in resolving these issues.

Practical steps taken by the international geophysical community to reduce the damage to technological systems from space weather include the development of numerical models capable of real-time predictions of geoeffective electromagnetic disturbances at the Earth's surface [[Pulkkinen et al., 2013](#)]. These models are based on the physical principles of the solar wind interaction with the Earth's magnetosphere and directly solve equations representing the underlying physical processes in the solar-terrestrial system using the driving conditions in the interplanetary space [[Gombosi et al., 2021](#)]. Special attention is to be paid to the capabilities of the current models to adequately predict dB/dt values, i.e., fast fluctuations of the magnetic field, which are the main indicator of the appearance of dangerous levels of GIC. Desirably, the modeling results are to be compared not just with GIC proxy dB/dt , but with actual observations of GIC in power transmission line.

It has become a necessity to find an adequate tool to reveal the temporal-spatial features of geomagnetic variations most responsible for the GIC generation [[Dimmock et al., 2021](#)]. The energy transfer of electromagnetic disturbances from the Earth's magnetosphere to the ionosphere occurs mainly due to the field-aligned currents (FACs), so geomagnetic impulses can be driven by localized FAC. Such a system of eddy Hall currents driven by FACs produces meso-scale magnetic disturbances. The eddy ionospheric currents can have very different spatial-time scales, depending on the type of magnetospheric disturbance. The ability to automatically recognize localized vortex structures and determine their parameters using magnetometer data is an extremely important task.

Standard wave analysis tools (Fourier decomposition into harmonic waves, description of space structure with a set of plane harmonics, etc.) cannot be applied for the consideration of impulsive disturbances. Commonly, the presence of vortex structures in geomagnetic disturbances is determined visually from the equivalent ionospheric current pattern. More advanced technique is the spherical elementary current system (SECS) approach based on data from 2D magnetometer array [[Amm and Viljanen, 2014](#)]. Additionally, a new method was proposed in [[Chinkin et al., 2020](#)], which makes it possible from data of 2D magnetometer network to automatically determine several simultaneous vortex structures and their instant characteristic parameters. Such methods should be applied to a study of geomagnetic events which produce a very intense burst of GIC.

Magnetic storms are considered a major risk factor for power systems at high latitudes. Two sources of magnetic storms are Coronal Mass Ejections (CMEs) emanating plasma clouds, and Corotating Interaction Regions (CIRs) created by high-speed solar wind streams from coronal holes. The question arises about the efficiency of the GIC generation by different types of magnetic storms.

Despite an enormous database of observations with a flotilla of satellites, extensive arrays of ground magnetometers and ionosphere sounders, and Sun imagers, some key questions related to the GIC excitation are still unsolved. These questions are related to the feasibility of global computer modeling to resolve meso-scale processes in the near-earth space, the availability of adequate tools for detection and analysis of meso-scale structures of magnetic storm/substorm, and the determination of key factors that control the GIC-effectiveness of different types of magnetic storms. In this review we'd like to draw the attention of the space community to these problems and present some preliminary steps in resolving these issues.

Prediction of Space Weather Hazard With MHD Modeling

Permanent monitoring of the interplanetary space upstream the Earth opens a principal possibility to construct a GIC forecast with a horizon of about one hour [Morley, 2020]. A promising forecast method combines global space weather models and simulations of near-surface electromagnetic fields [Pulkkinen et al., 2007; Zhang et al., 2012]. The input parameters of such models are satellite data on the solar wind plasma, interplanetary magnetic field (IMF), and solar radio flux F10.7 transmitted in real time from satellites at ~ 200 Earth radii (R_E).

The version of Space Weather Modeling Framework (SWMF) is currently used by NOAA's Space Weather Prediction Center is of particular interest because it produces surface disturbance outputs as part of magnetic disturbance forecasts. The SWMF is a software system (<http://csem.engin.umich.edu/swmf>) that simulates the space-weather environment from the solar chromosphere to the Earth's upper atmosphere [Tóth et al., 2005]. The SWMF comprises physical processes in different space domains through a modular approach, i.e. each domain is covered by a numerical sub-model developed specifically for that purpose. The near-Earth space is divided into the following physical domains: global magnetosphere (GM), inner magnetosphere (IM), and ionosphere (IE). The GM part is based on MHD equations. In the IM area the bounce-averaged trajectories of electrons and ions of different energies are calculated to capture ring current dynamics. The IE region 3D sub-model considers ionization, recombination, ion-neutral friction, and various heat sources to simulate the interaction between the ionosphere and magnetosphere. The SWMF simulation provides, in particular, the virtual ground magnetograms calculating Biot–Savart contributions from the currents in the magnetosphere outside of $2.5R_E$, FACs between 110 km altitude and $2.5R_E$, and height-integrated Pedersen and Hall ionospheric currents [Rastätter et al., 2014]. The SWMF consists of a dozen physics domains and sub-models and contains > 1 million lines of Fortran/C++ code, dozens of scripts and visualization tools (<http://csem.engin.umich.edu/tools/swmf>) [Tóth et al., 2005]. The SWMF runs can be requested via the Community Coordinated Modeling Center at the NASA Goddard Space Flight Center (<https://ccmc.gsfc.nasa.gov>) [Pulkkinen et al., 2009].

Here we present some results from [Pilipenko et al., 2023] obtained with a version of SWMF that is currently in use to issue short-term space weather predictions [Pulkkinen et al., 2013]. It is important to understand how well this model can capture ULF variations that drive GICs. The geomagnetic disturbances and associated bursts of GIC in the electric power line along Kola Peninsula for the May 27–28, 2017, geomagnetic storm were considered. The observations were compared with the global modeling results to validate whether this version of SWMF can reproduce adequately the magnetic field variability dB/dt , which is the driver of recorded GIC.

Comparison of Observations With the SWMF Modeling

The SWMF modeling output was obtained in the GSM coordinate system, where X is the coordinate along the Earth–Sun line directed towards the Sun. The model 1 run was performed with ~ 2 million grid cells with resolution $1/4R_E$ in the region $-20R_E \leq X \leq 8R_E$ and $|Y|, |Z| \leq 8R_E$, but it had a finer resolution $1/8R_E$ near the Earth up to $3.5R_E$. The model 2 run was performed with ~ 9.6 million cells and had $1/4R_E$ resolution within $8R_E$, but it used $1/2R_E$ resolution in a large area further away from the Earth.

A system to monitor the GIC in power transmission line “Northern Transit” operates at the Kola Peninsula [Selivanov et al., 2023]. The system consists of 4 substations at 330 kV power line. Each substation records a quasi-DC current in the dead-grounded neutral of the transformer. For the analysis data from the terminal substation Vykhodnoi (VKH) has been used with cadence from 2 Hz to 1-min.

The variations of the geomagnetic field horizontal components are measured by IMAGE magnetometers with 1-sec time resolution. The locations of selected magnetic stations in the vicinity of GIC recording system are shown in Figure 1. The substation VKH is located at the same geomagnetic latitude as magnetic stations IVA and LOZ.

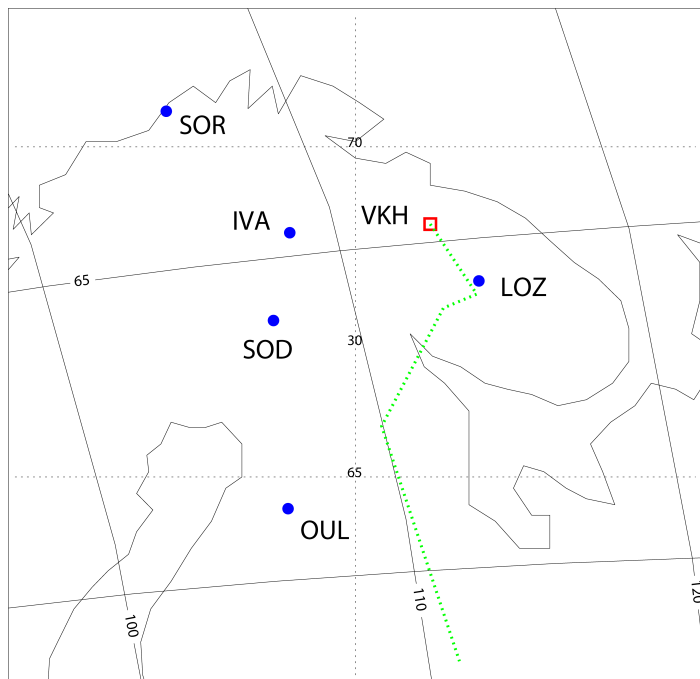


Figure 1. The map with location of GIC recording substation (empty red square) and nearby IMAGE magnetometers (blue dots). Solid thin lines denote the geomagnetic coordinates, dotted lines denote the geographic coordinates. The “Northern Transit” power transmission line is denoted by the dashed green line.

The SWMF modeling provides the horizontal magnetic field perturbation on the ground in the North, ΔB_n , and East, ΔB_e , directions with 1-min time resolution. The actual magnetometer observations at key station IVA from the IMAGE array have been compared with the same virtual station. Magnetic disturbances in the horizontal X and Y components, and time derivatives dX/dt , dY/dt , and $|dB/dt| = \sqrt{(dX/dt)^2 + (dY/dt)^2}$, calculated with 3-point scheme, have been examined.

The storm on May 27, 2017, has been considered as an example. The storm was caused by the southward reorientation of IMF B_z at ~ 2130 UT. The extreme value of the SYM-H index was about -140 nT, and the auroral SML index irregularly decreased till about -1500 nT. Upon long-time growth phase the magnetic variations became irregular, when intense Pi3 pulsations superposed the magnetic bay during 00–05 UT, May 28 (Figure 2). These pulsations are quasi-periodic sequence of magnetic impulses, whose time scale varies from ~ 20 min to ~ 10 min, and are evident in all components, but most clearly in Y-component with peak-to-peak amplitudes ~ 300 nT.

Observations have been compared with the global magnetospheric parameters reproduced by modeling. The basic features of the SYM-H index characterizing the intensity of the ring current agreed with the modeling predictions (Figure 3). Although the extreme value of modeled SYM-H index, about -80 nT (model 2), was

noticeably weaker than the measured SYM-H index. The SWMF model reproduces cross-polar potential CP index [kV]. For validation of the modeling results, a measure of the trans-polar current across the polar cap – the PC index [mV/m], has been used. The comparison indeed showed an expected similarity in variations of the modeled CP index and the PC index in both Northern and Southern hemispheres (Figure 3).

The main interest is whether modeling can describe not only global variations of the magnetosphere-ionosphere system, but the magnetic field variability as well. Although the magnetic disturbance was observed to be much larger in the X-component than in the Y-component, $|\Delta X| \gg |\Delta Y|$, the time derivatives dX/dt and dY/dt were nearly of the same peak-to-peak magnitude ~ 20 nT/s (Figure 2). During the period with high Pi3 activity, extremely high values of GIC amplitudes were recorded (peak-to-peak values up to $J \sim 80$ A) at the substation VKH (Figure 2). Each burst of magnetic variability was accompanied by a burst of GIC.

The virtual magnetograms for station IVA are shown in Figure 4. The modelled magnetic bay in the X-component roughly matched observations. The substorm onset on 22 UT, May 27 was well reproduced by modeling, although the magnetic disturbance was weaker than the observed one. However, the intense quasi-periodic pulsations in Y-

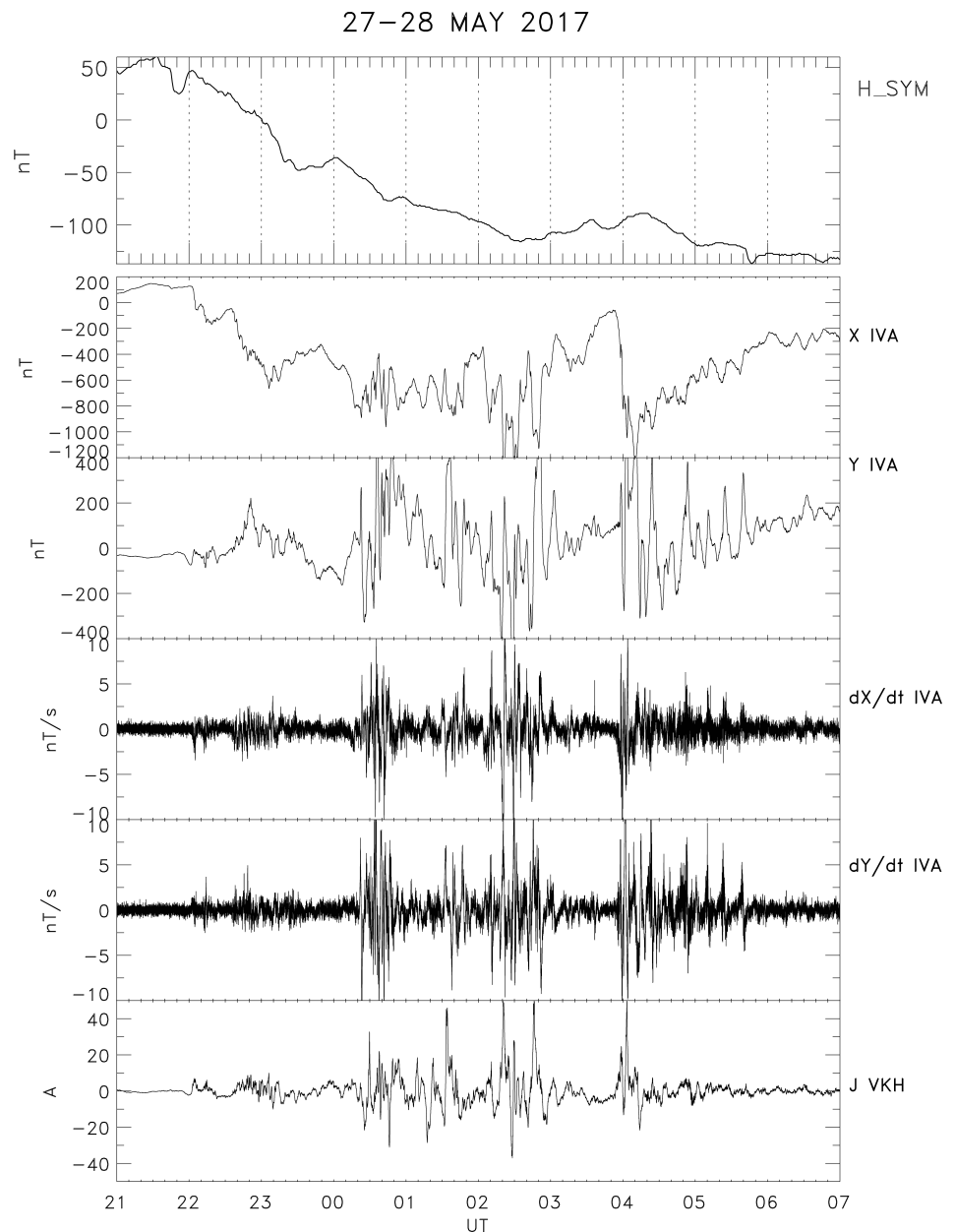


Figure 2. Variations during time interval 2017, May 27, 21 UT – May 28, 07 UT of the *SYM-H* index, geomagnetic field *X* and *Y* components at magnetic station IVA (1 Hz sampling rate); corresponding magnetic field variability (dX/dt , dY/dt), and GIC *J* recorded at VKH station (2 Hz sampling rate).

component did not show up in virtual magnetograms. The variability magnitude $|dB/dt|$ predicted by the SWMF reached up to 10 nT/min only, that was much less than actual observations, $\sim 200\text{--}300\text{ nT/min}$ (Figure 4). So, the contrast between the magnetic field variability predicted by the MHD modeling and observed fluctuations in Pi3 band was very prominent, more than an order of magnitude. Thus, the modeling of meso-scale magnetic field features was inadequate to predict the GIC magnitude in this event.

Restoration of Meso-Scale Ionospheric Vortex Characteristics From Ground Magnetometer Data

Standard data analysis tools for ULF waves based on the decomposition in time-space into a set of sinusoidal harmonics and plane waves cannot be applied for the analysis of impulsive disturbances. Pi3 time series is probably composed from hierarchy of vortices driven by localized FACs. The FAC flowing along the magnetic field lines between the mag-

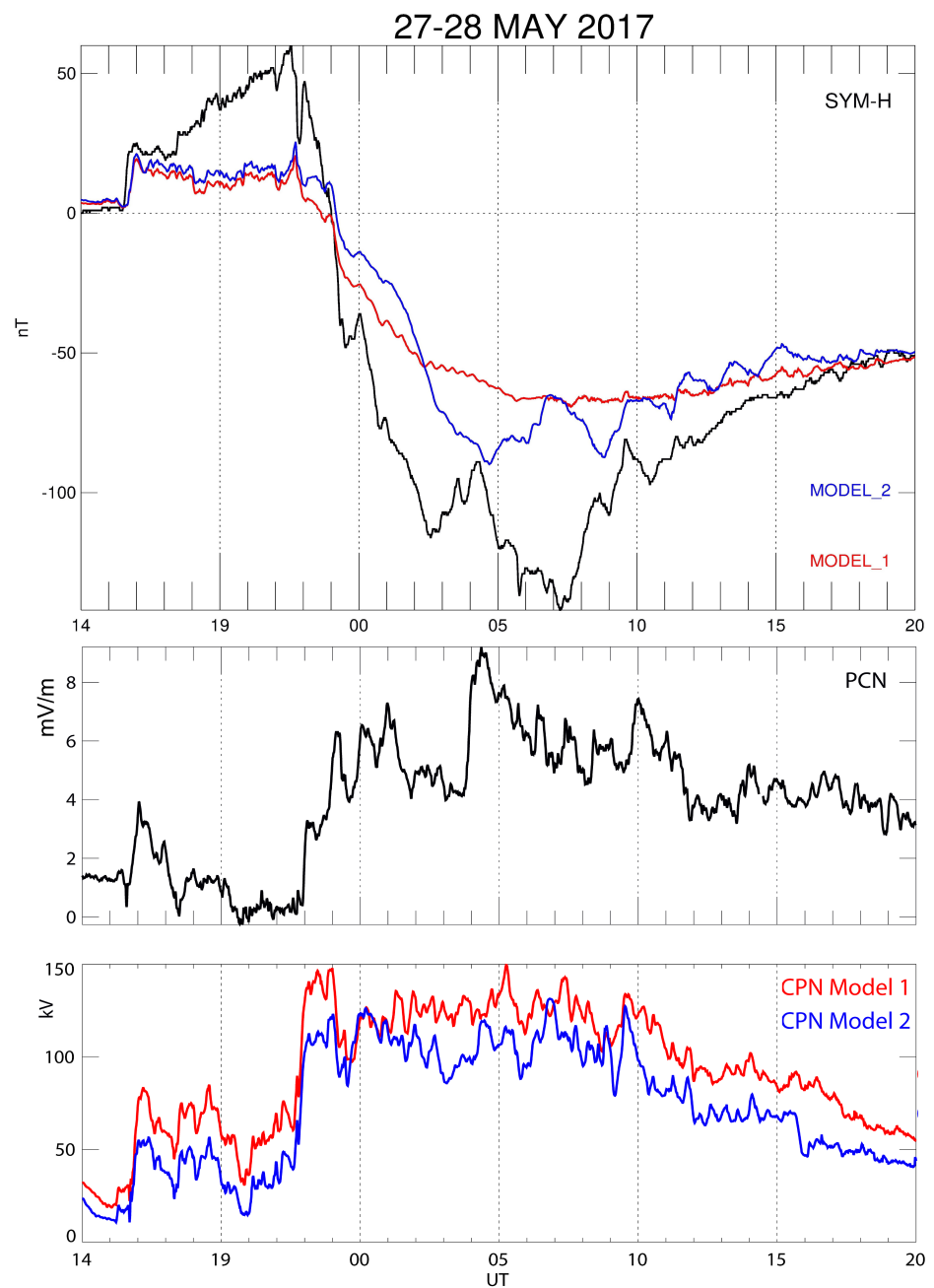


Figure 3. Variations during time interval 2017, May 27, 14 UT – May 28, 20 UT of the observed SYM-H index (black line) and the SYM-H index predicted by the SWFM modeling (runs 1 and 2 shown by red and blue lines), and of PC index [mV/m] (characterizing the intensity of the transpolar current) in the Northern hemisphere (upper panel), and the modeled (run 1 and 2) cross-polar potential CPN in the Northern hemisphere [kV] (bottom panel).

netosphere and ionosphere is closed in the conducting E-layer by the system of transverse Pedersen \mathbf{J}_P and Hall \mathbf{J}_H currents

$$\mathbf{J}_\perp = \mathbf{J}_P + \mathbf{J}_H = \Sigma_P \mathbf{E} + \Sigma_H [\mathbf{n} \times \mathbf{E}].$$

Here, \mathbf{J}_\perp is the height-integrated ionospheric current, \mathbf{E} is the horizontal electric field, \mathbf{n} is the normal to the ionospheric plane, and the Σ_P and Σ_H are height-integrated Pedersen and Hall conductances, \mathbf{J}_P and \mathbf{J}_H are the vortex-free (solenoidal) and divergence-free (eddy) components of the horizontal current vector \mathbf{J}_\perp . Introducing 2D differential

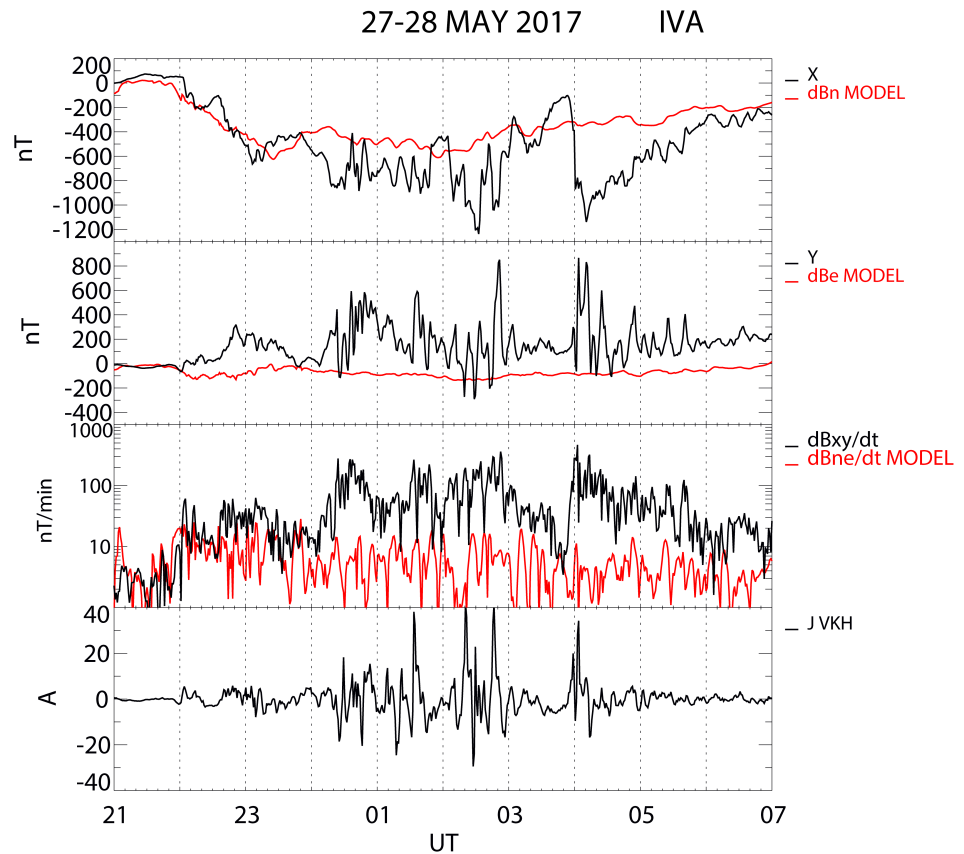


Figure 4. Variations of geomagnetic field and GIC during time interval 2017, May 27, 21 UT – May 28, 07 UT: (upper panels) magnetograms X , Y (black lines), measured at magnetic station IVA, and B_n , B_e components predicted by SWMF model-1 for the same location (red line); (3rd panel) $|d\mathbf{B}/dt|$ estimated at IVA from data (black line) and from virtual magnetometer (red line); (bottom panel) GIC recorded at VKH substation.

operators $\text{Rot} = \mathbf{n} \cdot \text{rot}$ and $\text{Div} = \{\partial x, \partial y\}$ these properties can be written as $\text{Rot} \mathbf{J}_p = 0$ and $\text{Div} \mathbf{J}_H = 0$. At high latitudes, where the geomagnetic field is nearly vertical, the vertical current j_z is closed only by the Pedersen current $j_z = \text{Div} \mathbf{J}_p$. The total magnetic effect under the ionosphere from j_z and \mathbf{J}_p vanishes, therefore the ground magnetic disturbance is produced only by \mathbf{J}_H . In the ionosphere with horizontally homogeneous conductance the local FAC is related to the current Hall as follows:

$$j_z = \left(\frac{\Sigma_P}{\Sigma_H} \right) \text{rot} \mathbf{J}_H.$$

An ionospheric vortex system is driven by local FAC (Figure 5, upper panel). The radial structure of the horizontal $B_r(r)$ and vertical $B_z(r)$ components of the magnetic field produced on the ground by such a system is qualitatively demonstrated in Figure 5 (bottom panel). Pedersen currents flow symmetrically from the center of the FAC tube, and they do not excite a magnetic response on the ground ($B_\varphi = 0$). The radial component $B_r(r)$ on the ground produced by the ionospheric Hall currents has a bipolar form ($B_r(r) \rightarrow 0$ under the center of the eddy current system) with maximum at distance R_{\max} . According to theoretical notions the corresponding radius δ of the ionospheric Hall current vortex is to be related with R_{\max} as follows $\delta = \sqrt{2}R_{\max} - h$ (where h is the height of the E-layer).

For the analysis of magnetometer data from a 2D array a new technique was proposed in [Chinkin et al., 2020]. Using the cubic polynomial interpolation, the observed values have been transformed onto a regular geographic 2D grid. To make the vortex-like structures

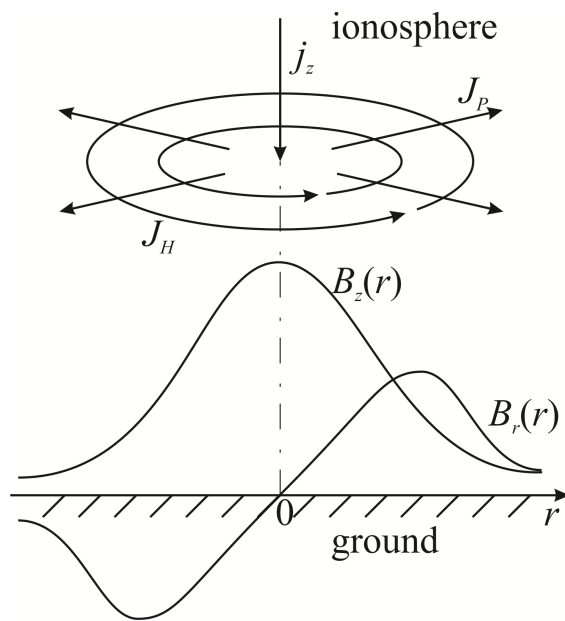


Figure 5. Schematic representation of the azimuthally symmetric field-aligned current J_z flowing into the ionosphere and its coupling to the transverse Pedersen J_P and Hall J_H currents in the conductive E-layer of the ionosphere (upper panel). Bottom panel shows radial dependence of the radial $B_r(r)$ and vertical $B_z(r)$ components of the geomagnetic disturbance on the ground.

more evident, the equivalent ionosphere current field \mathbf{J}_\perp is derived by $\pi/2$ rotation of the ground field vector \mathbf{B}_\perp . Then, the 2D scalar field of the ionospheric current vorticity $G(x, y) = \text{rot} \mathbf{J}_\perp(x, y)$ has been calculated. The extrema of function $G(x, y)$ correspond to FAC peaks flowing in or out the ionosphere. As a result, this technique enables one to determine a set of instant vortex centers $\mathbf{r}_0 = (x_0, y_0)$ for each time moment. A characteristic scale of vortex will be characterized by its effective radius R . The vortex radial scale is estimated by finding first significant extremum of vector circulation \mathbf{J}_\perp along the contour $\Gamma(R)$ (the circle of radius R with its center at \mathbf{r}_0) $C(\Gamma(R)) = \oint_\Gamma \mathbf{J}_\perp d\mathbf{l} = \int_S \text{rot} \mathbf{J}_\perp dS$. To have the possibility to trace the vortex trajectory, the program merges automatically all the predetermined vortex centers, providing a possibility to determine a single vortex trajectory.

The developed algorithm was applied to identify a spatial structure of Pi3 pulsations during the magnetic storm on June 27–29, 2013 [Chinkin et al., 2021]. The prolonged period of southward IMF drove the magnetosphere into the magnetic storm, during which geomagnetic indices reached maximal values of $|Dst| \sim 120 \text{ nT}$ and $AE \sim 1000 \text{ nT}$. During the period when intense Pi3 pulsations were superposed on the magnetic bay (Figure 6), extremely high values of GICs were recorded (up to $\sim 120 \text{ A}$ per node) in transformers of power transmission line in North-West Russia [Apatenkov et al., 2020; Belakhovsky et al., 2019].

Data from 2D array of IMAGE magnetometers in the vicinity of the power line was analyzed. The snapshot of ionospheric Hall currents clearly shows the pair of FACs forming adjacent vortices (Figure 7). There is likely a hierarchy of such short-lived vortices with different spatial scales.

Figure 8 presents the time evolution of the vortex characteristics restored with the help of the described algorithm. The presented features include trajectories of the identified vortices (geographic latitude Φ and longitude Λ), FAC density J_z in the center of each vortex, and its estimated radius δ in the ionosphere. During the period 01–03 UT, the occurrence of irregular series of magnetic pulses is evident from magnetograms of Y and Z components (3rd and 2nd panels from the bottom in Figure 8). The peak values of J_z correspond to extrema of vertical Z component in accordance with the structure of an isolated vortex (Figure 5). Each magnetic pulse is found to be associated with the ionospheric vortex. Peak values of FAC density reach $|J_z| \sim 5 \text{ A/km}^2$. Typical scale 2δ of the recognized vortices is $\sim 400\text{--}500 \text{ km}$. The vortices move eastward, that is in the anti-sunward direction, and no regular movement in the latitudinal direction is observed. The observed pattern of vortices is compared with bursts of GICs recorded at VKH (bottom panel in Figure 8). The one-to-one correlation between a disturbance of component Z and GIC burst is clearly observed. Thus, each vortex induces a GIC enhancement with amplitude up to $\sim 100 \text{ A}$.

GIC-effectiveness of CME and CIR Storms

Magnetic storms are caused by two possible forms of the solar activity. At the solar cycle maximum, non-recurrent storms caused by Coronal Mass Ejections (CMEs) are predominantly observed. At the minimum and declining phase of the solar activity, recurrent storms produced by high-speed solar wind streams emanating from coronal holes (Corotating Interaction Regions, CIR) are usually observed. CIRs cause magnetic storms of weak to moderate intensity, but these storms have a longer duration than CME storms. CIR storms develop against the background of fast-speed solar wind flows and

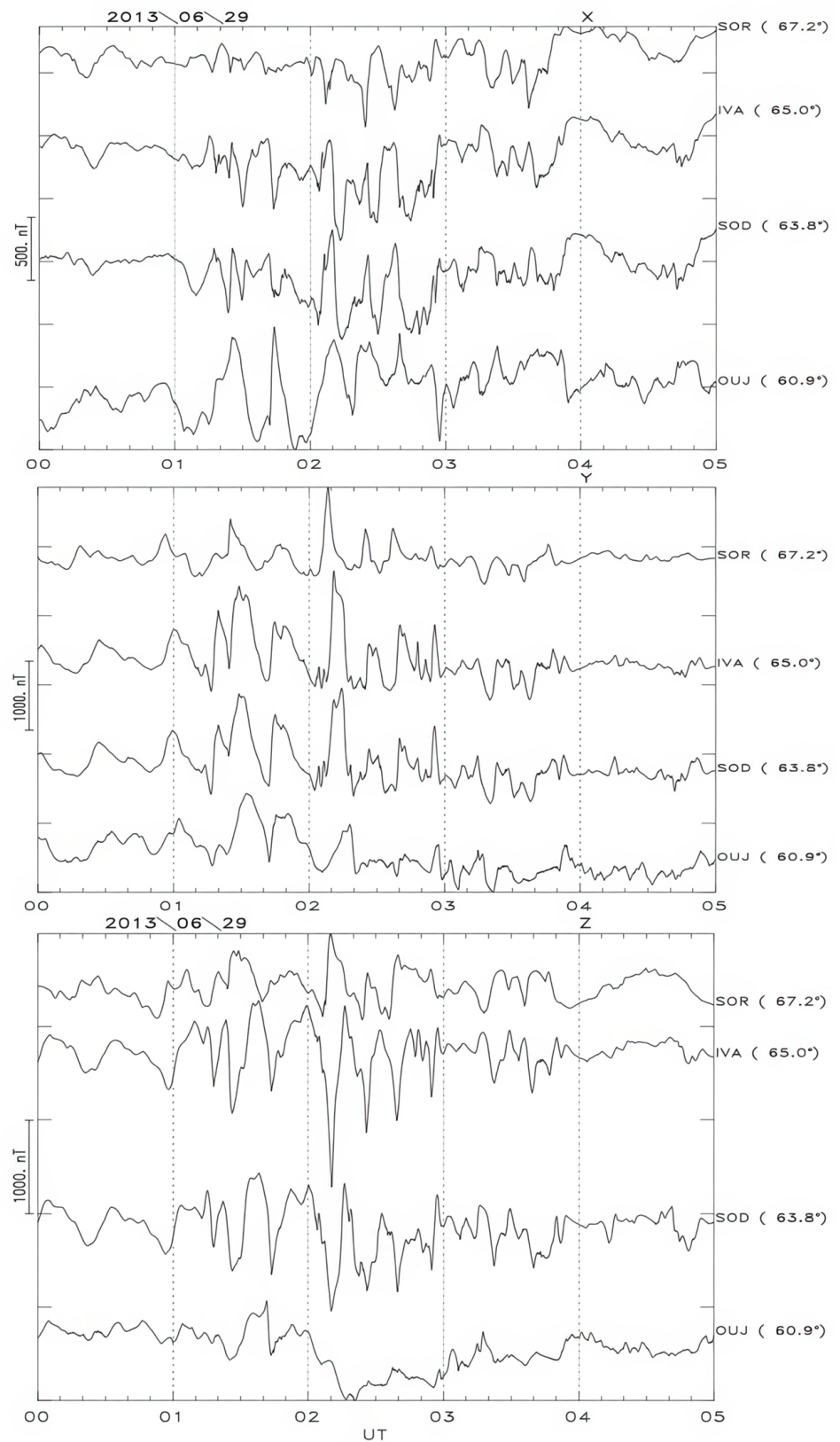


Figure 6. Geomagnetic field variations at latitudinal array of stations SOR, IVA, SOD, OUJ from the IMAGE array during magnetic storm on June 29, 2013, from 00 UT till 05 UT: X, Y, and Z components. Geomagnetic latitudes are indicated near the station codes on the right-hand ordinate axis.

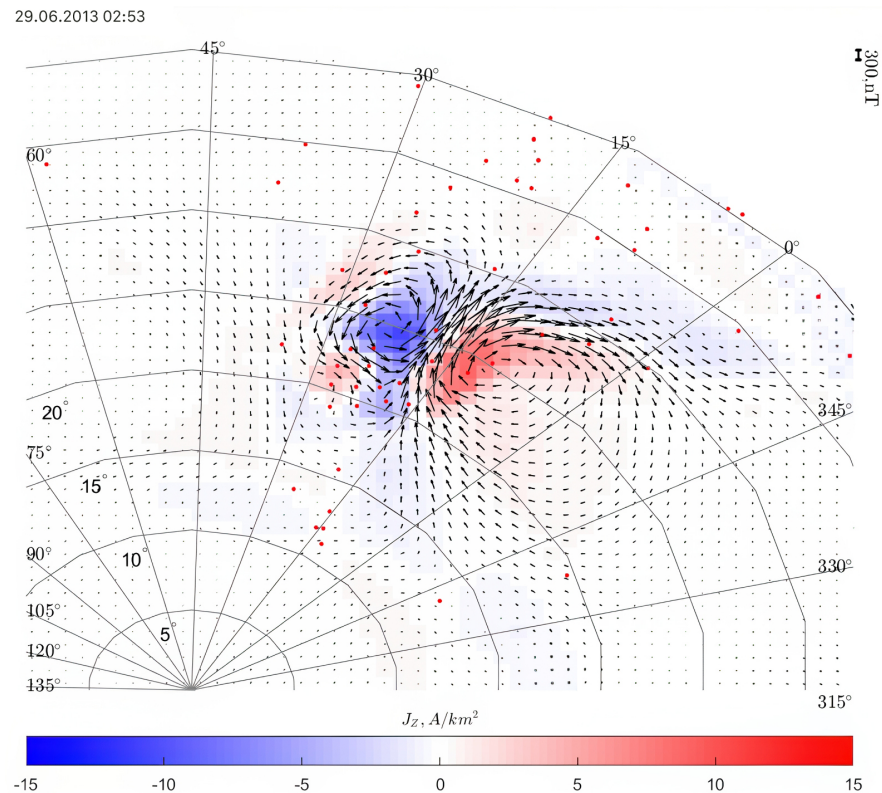


Figure 7. 2D vector field of the equivalent ionospheric current \mathbf{J} , constructed for the time moment June 29, 0253 UT, 2013. Arrow length corresponds to the magnitude of ground magnetic disturbances. Red dots denote the station locations. The density of inward flowing FAC $J_z > 0$ (corresponding to clockwise vortex) is denoted with red color, whereas the density of outward flowing FAC $J_z < 0$ (corresponding to counterclockwise vortex) is denoted with blue color.

are accompanied by a higher level of ULF pulsations in the magnetosphere [Borovsky and Denton, 2006]. Naturally, the question arises about the generation efficiency of intense GICs by different types of magnetic storms. The impact of two types of magnetic storms on the growth of GICs in the power transmission line “Northern Transit” was considered in [Belakhovsky et al., 2023] using as example the events on November 3–5, 2021 and October 11–13, 2021 (Figure 9).

The CME storm on November 3–5, 2021 is caused by the arrival of an interplanetary magnetic cloud to the Earth's magnetosphere. The $Dst/SYM-H$ and AE indices reach $-105/118$ nT and ~ 3040 nT, correspondingly. The geomagnetic field disturbance in the vicinity of GIC recording substation is $\Delta X \sim 1200$ nT (Figure 9, left-hand panel). The magnitude of the geomagnetic field time derivative reach $|dX/dt| \approx |dY/dt| \approx 300$ nT/min. The highest GIC magnitude at VKH substation is ~ 20 A.

The CIR magnetic storm on October 11–13, 2021 produces $Dst/SYM-H$ up to $-65/72$ nT and AE index up to ~ 2650 nT. The IMF B_z component changes its sign to positive several times, which results in a low storm intensity. Three consecutive substorms observed at 19–23 UT, 23–02 UT, and 02–05 UT, are accompanied by GIC bursts (Figure 9, right-hand panel). The third substorm is the most intense ($\Delta X \approx 1000$ nT), while the GIC also reaches the highest magnitude ~ 40 A. The peak magnitudes of time derivatives are $|dX/dt| \sim 300$ nT/min, and $|dY/dt| \sim 330$ nT/min.

Geoeffectiveness of a magnetic storm in respect to the GIC excitation may be characterized by the ratio between the maximal $|SYM - H|_{\max}$ and maximal GIC amplitude J_{\max}

$$\Gamma = J_{\max} / |SYM - H|_{\max}.$$

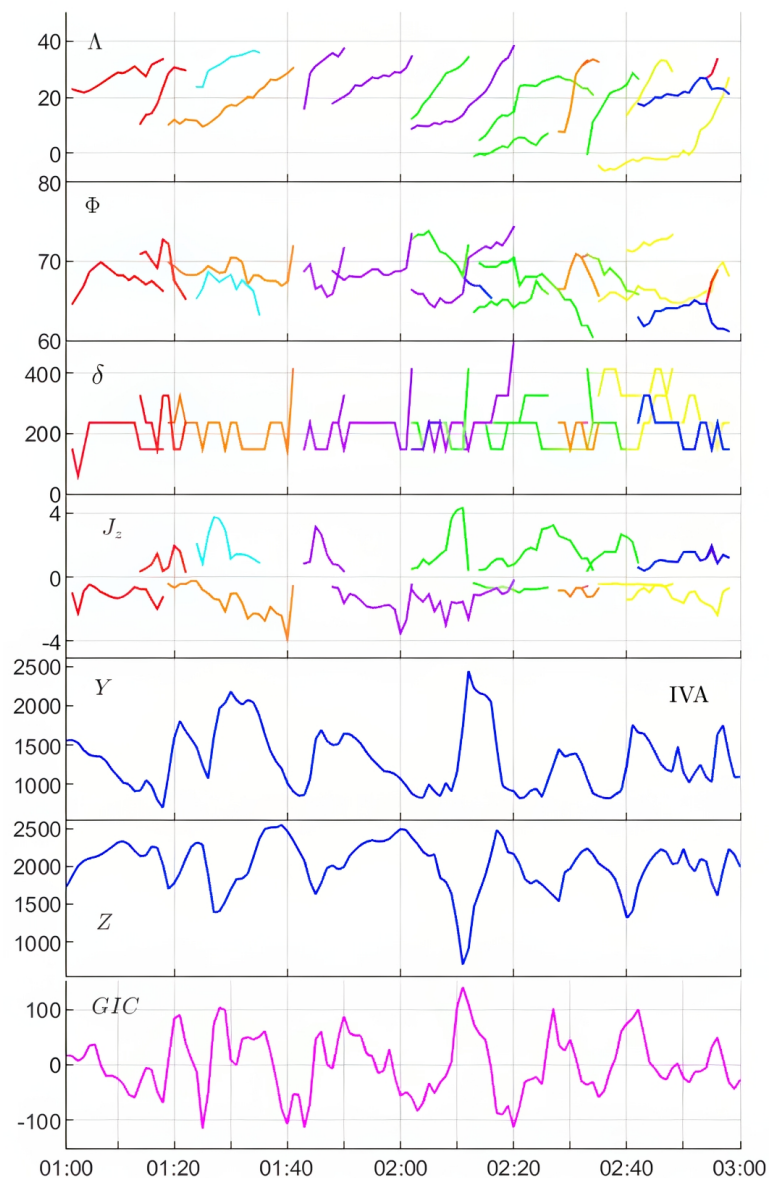


Figure 8. Dynamics of the vortex characteristics during time interval June 29, 2013, from 01 to 03 UT (from top to bottom): geographic longitude Λ and latitude Φ of the vortex center, radial scale δ [km] of each vortex in the ionosphere, and density of FAC J_z [A/km²] in the vortex center. Bottom panels show the variations of Y [nT] and Z [nT] components of geomagnetic field at IVA station, and GIC [A] recorded in the transformer at substation VKH. The ratio Σ_P/Σ_H has been set equal 1.

The CME storm on November 2021 has $J_{\max} \sim 20$ A, whereas the CIR storm on October 2021 has maximal recorded GIC magnitude $J_{\max} \sim 40$ A. Thus, the GIC-effectiveness of the CME storm is $\Gamma = 0.17$ A/nT, and that of the CIR storm is $\Gamma = 0.56$ A/nT, thus nearly 3 times larger! The comparison of storm geoeffectiveness according to maximal AE index provides a similar difference, but ~ 2.5 times.

The reason for this difference can be comprehended by consideration of 2D distribution of ionospheric currents for both storms constructed from 2D magnetometer array (Figure 10). For the CME storm at the time of GIC maximum (2135 UT), a predominant contribution to geomagnetic disturbances is provided by the westward auroral electrojet. For the CIR storm at the moment of GIC maximum (0315 UT), along with the auroral electrojet, a significant contribution of eddy current systems to geomagnetic disturbances is observed.

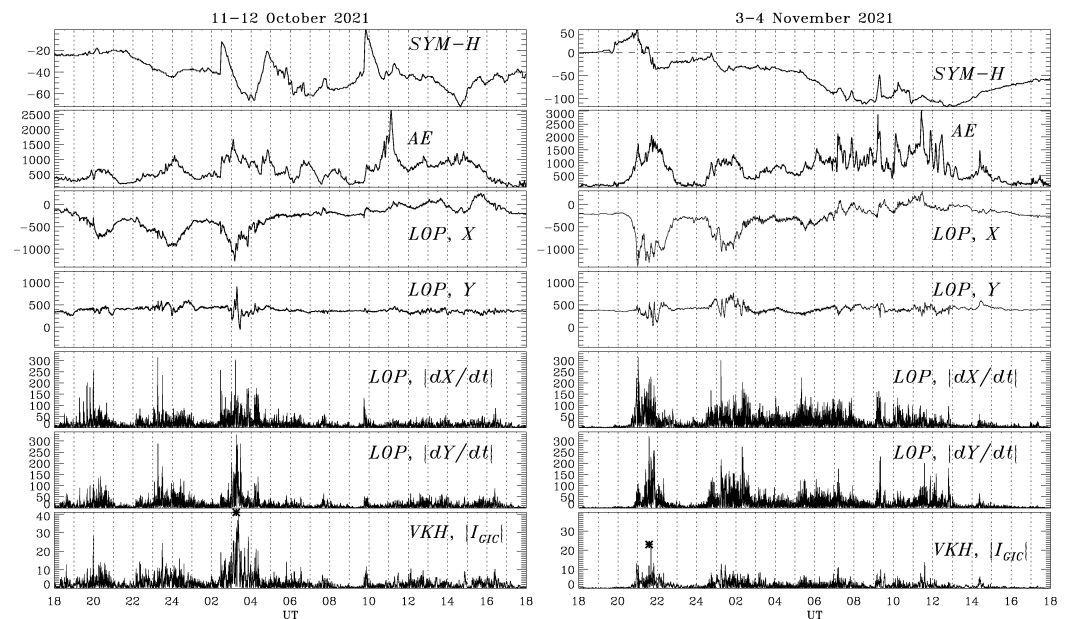


Figure 9. Variations of geomagnetic field at LOP station and GIC during the CME storm on November 3, 18 UT – November 4, 18 UT, 2021 (left-hand panel) and CIR storm on October 11, 18 UT – October 12, 18 UT, 2021 (right-hand panel): SYM-H index [nT], AE index [nT], X and Y-components of the geomagnetic field [nT], magnitudes $|dX/dt|$ [nT/min] and $|dY/dt|$ [nT/min], and GIC amplitude J [A] from VKH substation has been set equal 1.

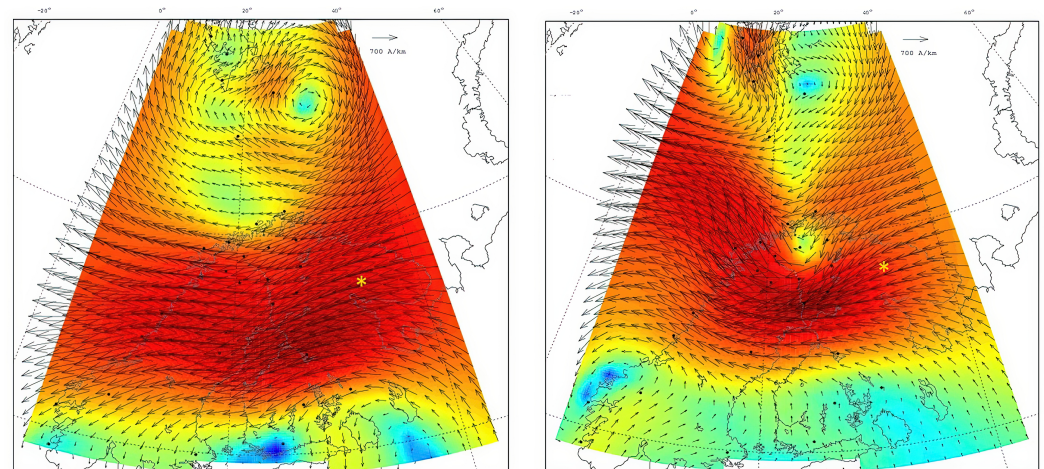


Figure 10. Equivalent ionospheric current systems according to 2D IMAGE magnetometer array for November 3, 2021, 21:35 UT (left-hand panel) and for October 12, 2021, 03:15 UT (right-hand panel). Yellow star indicates the location of GIC substation VKH.

Thus, GIC magnitude does not always depend on the storm intensity only. Development of eddy ionospheric current systems can lead to a significant GIC for weaker CIR storms. However, the reliable prediction of the space weather impact on technological systems is still a challenge for the space community because we still cannot predict the occurrence of vortex structures during a particular storm.

Prospects of Future Studies

Some studies that compared magnetometer measurements with simulated ground magnetic fields with various global MHD models [Kwagala et al., 2020; Yu and Ridley, 2008] indicated that observational data contain more structure than a model, and a model tends to miss some localized intense disturbances. In general, most of the models tend

to underestimate the dB/dt [Pulkkinen et al., 2013]. Therefore, continual investigation of global models with new events is highly beneficial to obtain a greater understanding of the model applicability for space weather purposes. Any efforts to compare the global MHD modeling results with actual GIC observations, but not just GIC proxy dB/dt , are highly desirable.

The analysis of the geomagnetic disturbances and GIC variations during the magnetic storm on May 2017 showed that the evolution of global magnetospheric parameters was reasonably well reproduced by the SWMF modeling. However, the current version of SWMF was found to be unable to reproduce the meso-scale ionospheric structures (few hundred km) [Pilipenko et al., 2023]. Comparison of IMAGE magnetometer observations during the September 2017 storm with virtual magnetometers from the SWMF run for various spatial resolutions, from low ($1/4R_E$ and 10^6 cells) to high ($1/16R_E$ and 8×10^6 cells), showed that only at low/mid-latitudes a higher spatial resolution provided more accurate magnetic disturbances, whereas at sub-auroral latitudes, increasing the spatial resolution provided a negligible improvement [Dimmock et al., 2021]. In a similar way, investigation of the SWMF performance in predicting magnetic perturbations for major storms in 2001–2015 showed that modeling captured only the general trend of ground perturbations [Kwagala et al., 2020]. The model performed reasonably well for dB/dt predictions for the low level < 60 nT/min, but short-lived large dB/dt were greatly underestimated. These facts suggest that global MHD models used for space weather predictions are inadequate so far for the prediction of intense GIC bursts related to Pi3 pulsations and other meso-scale structures.

The low-frequency part of the ULF period range (5–20 min) is of special importance for the GIC studies. While the spectral power of geomagnetic variations in general drops with frequency, the magnetic field variability dB/dt grows with frequency. The resultant GIC is the convolution of these factors and has a maximum at time scales 2–10 min, that is in the period range of Pi3 pulsations. At these regional scales, weaker but rapidly varying localized vortex-like current systems superposed on the electrojet produce intense GIC bursts. The new technique of data analysis has confirmed that actual driver of GIC is not the intensification of global ionospheric electrojet, but the occurrence of meso-scale short-lived structures in the ionosphere. Bursts of largest GICs is caused by a quasi-periodic sequence of local anti-sunward drifting ionospheric vortices driven by FACs with densities up to $\sim 5 \times 10^{-6}$ A/m². It is hard to decide whether the inability of the SWMF to predict the occurrence of Pi3 pulsations is related with some missing magnetotail physics or not, because the physical mechanism of these pulsations has not been firmly established yet. Pi3 pulsation periodicity (5–20 min) is longer than typical magnetospheric field line eigenoscillations (~ 3 min). Thus, though Pi3 pulsations are mentioned in all the textbooks on ULF waves in the magnetosphere, their physical mechanism is still a challenge to the ULF community. The relationship between the large-scale auroral electrojet and localized current systems superposed on it has not been established yet.

Rather unexpectedly, weaker CIR storms were found to produce more intense GIC bursts than stronger CME storms. This distinction is caused by a higher level of Pi3 pulsations during the CIR storms. Thus, the fine impulsive structure of storm/substorm seems to be important, but underestimated, factor of the space weather geoeffectiveness. Although, many additional factors, such as the underlying crust conductivity, configuration of the power transmission system, type of high-voltage transformer, etc. are also essential for the GIC size in a particular system.

Acknowledgments. The SWMF modeling results were provided by L. Rastaetter and M. Hartinger. We appreciate a very thorough examination of the m/s by a Reviewer and his helpful comments. The study is supported by the grant 21-77-30010 from the Russian Science Foundation. The IMAGE magnetometer data and related 2D ionospheric current modeling are available at the website <https://space.fmi.fi/image/>.

References

- Amm, O., and A. Viljanen (2014), Ionospheric disturbance magnetic field continuation from the ground to the ionosphere using spherical elementary current systems, *Earth, Planets and Space*, 51(6), 431–440, <https://doi.org/10.1186/BF03352247>.
- Apatenkov, S. V., V. A. Pilipenko, E. I. Gordeev, et al. (2020), Auroral Omega Bands are a Significant Cause of Large Geomagnetically Induced Currents, *Geophysical Research Letters*, 47(6), <https://doi.org/10.1029/2019GL086677>.
- Belakhovsky, V. B., V. Pilipenko, M. Engebretson, et al. (2019), Impulsive disturbances of the geomagnetic field as a cause of induced currents of electric power lines, *Journal of Space Weather and Space Climate*, 9, <https://doi.org/10.1051/swsc/2019015>.
- Belakhovsky, V. B., V. A. Pilipenko, Y. A. Sakharov, and V. N. Selivanov (2023), The Growth of Geomagnetically Induced Currents during CME and CIR Geomagnetic Storms in 2021, *Bulletin of the Russian Academy of Sciences: Physics*, 87(2), 236–242, <https://doi.org/10.3103/S1062873822700988>.
- Borovsky, J. E., and M. H. Denton (2006), Differences between CME-driven storms and CIR-driven storms, *Journal of Geophysical Research: Space Physics*, 111(A7), <https://doi.org/10.1029/2005JA011447>.
- Chinkin, V. E., A. A. Soloviev, and V. A. Pilipenko (2020), Identification of Vortex Currents in the Ionosphere and Estimation of Their Parameters Based on Ground Magnetic Data, *Geomagnetism and Aeronomy*, 60(5), 559–569, <https://doi.org/10.1134/S0016793220050035>.
- Chinkin, V. E., A. A. Soloviev, V. A. Pilipenko, et al. (2021), Determination of vortex current structure in the high-latitude ionosphere with associated GIC bursts from ground magnetic data, *Journal of Atmospheric and Solar-Terrestrial Physics*, 212, 105,514, <https://doi.org/10.1016/j.jastp.2020.105514>.
- Dimmock, A. P., D. T. Welling, L. Rosenqvist, et al. (2021), Modeling the Geomagnetic Response to the September 2017 Space Weather Event Over Fennoscandia Using the Space Weather Modeling Framework: Studying the Impacts of Spatial Resolution, *Space Weather*, 19(5), <https://doi.org/10.1029/2020SW002683>.
- Engebretson, M. J., K. R. Kirkevold, E. S. Steinmetz, et al. (2020), Interhemispheric Comparisons of Large Nighttime Magnetic Perturbation Events Relevant to GICs, *Journal of Geophysical Research: Space Physics*, 125(8), <https://doi.org/10.1029/2020JA028128>.
- Gombosi, T. I., Y. Chen, A. Gloer, et al. (2021), What sustained multi-disciplinary research can achieve: The space weather modeling framework, *Journal of Space Weather and Space Climate*, 11, 1–55, <https://doi.org/10.1051/swsc/2021020>.
- Heyns, M. J., S. I. Lotz, and C. T. Gaunt (2021), Geomagnetic Pulsations Driving Geomagnetically Induced Currents, *Space Weather*, 19(2), <https://doi.org/10.1029/2020SW002557>.
- Kappenman, J. G. (2005), An overview of the impulsive geomagnetic field disturbances and power grid impacts associated with the violent Sun-Earth connection events of 29–31 October 2003 and a comparative evaluation with other contemporary storms, *Space Weather*, 3(8), <https://doi.org/10.1029/2004SW000128>.
- Kozyreva, O., V. Pilipenko, R. Krasnoperov, et al. (2019), Fine structure of substorm and geomagnetically induced currents, *Annals of Geophysics*, 62, <https://doi.org/10.4401/ag-8198>.
- Kwagala, N. K., M. Hesse, T. Moretto, et al. (2020), Validating the Space Weather Modeling Framework (SWMF) for applications in northern Europe: Ground magnetic perturbation validation, *Journal of Space Weather and Space Climate*, 10, 33, <https://doi.org/10.1051/swsc/2020034>.
- Morley, S. K. (2020), Challenges and Opportunities in Magnetospheric Space Weather Prediction, *Space Weather*, 18(3), <https://doi.org/10.1029/2018SW002108>.
- Ngwira, C. M., D. Sibeck, M. V. D. Silveira, et al. (2018), A Study of Intense Local dB/dt Variations During Two Geomagnetic Storms, *Space Weather*, 16(6), 676–693, <https://doi.org/10.1029/2018SW001911>.
- Pilipenko, V. A. (2021), Space weather impact on ground-based technological systems, *Solar-Terrestrial Physics*, 7(3), 68–104, <https://doi.org/10.12737/stp-73202106>.

- Pilipenko, V. A., O. Kozyreva, M. Hartinger, et al. (2023), Is the Global MHD Modeling of the Magnetosphere Adequate for GIC Prediction: the May 27-28, 2017 Storm, *Cosmic Research*, 61(2), 120–132, <https://doi.org/10.1134/S001095252600044>.
- Pirjola, R., K. Kauristie, H. Lappalainen, et al. (2005), Space weather risk, *Space Weather*, 3(2), <https://doi.org/10.1029/2004SW000112>.
- Pulkkinen, A., M. Hesse, M. Kuznetsova, and L. Rastätter (2007), First-principles modeling of geomagnetically induced electromagnetic fields and currents from upstream solar wind to the surface of the Earth, *Annales Geophysicae*, 25(4), 881–893, <https://doi.org/10.5194/angeo-25-881-2007>.
- Pulkkinen, A., M. Hesse, S. Habib, et al. (2009), Solar shield: forecasting and mitigating space weather effects on high-voltage power transmission systems, *Natural Hazards*, 53(2), 333–345, <https://doi.org/10.1007/s11069-009-9432-x>.
- Pulkkinen, A., L. Rastätter, M. Kuznetsova, et al. (2013), Community-wide validation of geospace model ground magnetic field perturbation predictions to support model transition to operations, *Space Weather*, 11(6), 369–385, <https://doi.org/10.1002/swe.20056>.
- Rastätter, L., G. Tóth, M. M. Kuznetsova, and A. A. Pulkkinen (2014), CalcDeltaB: An efficient postprocessing tool to calculate ground-level magnetic perturbations from global magnetosphere simulations, *Space Weather*, 12(9), 553–565, <https://doi.org/10.1002/2014SW001083>.
- Selivanov, V., T. Aksenovich, V. Bilin, et al. (2023), Database of geomagnetically induced currents in the main transmission line «Northern Transit», *Solar-Terrestrial Physics*, 9(3), 93–101, <https://doi.org/10.12737/stp-93202311>.
- Tóth, G., I. V. Sokolov, T. I. Gombosi, et al. (2005), Space Weather Modeling Framework: A new tool for the space science community, *Journal of Geophysical Research: Space Physics*, 110(A12), <https://doi.org/10.1029/2005JA011126>.
- Viljanen, A., and R. Pirjola (1994), Geomagnetically induced currents in the Finnish high-voltage power system: A geophysical review, *Surveys in Geophysics*, 15(4), 383–408, <https://doi.org/10.1007/BF00665999>.
- Yagova, N. V., V. A. Pilipenko, Y. A. Sakharov, and V. N. Selivanov (2021), Spatial scale of geomagnetic Pc5/Pi3 pulsations as a factor of their efficiency in generation of geomagnetically induced currents, *Earth, Planets and Space*, 73(1), <https://doi.org/10.1186/s40623-021-01407-2>.
- Yu, Y., and A. J. Ridley (2008), Validation of the space weather modeling framework using ground-based magnetometers, *Space Weather*, 6(5), <https://doi.org/10.1029/2007SW000345>.
- Zhang, J. J., C. Wang, and B. B. Tang (2012), Modeling geomagnetically induced electric field and currents by combining a global MHD model with a local one-dimensional method, *Space Weather*, 10(5), <https://doi.org/10.1029/2012SW000772>.